DOKUZ EYLÜL UNIVERSITY
GRADUATE SCHOOL OF NATURAL AND APPLIED SCIENCES

CHARACTERIZATION OF NEUTRON AND HIGH PURITY GERMANIUM DETECTORS WITH ADVANCED DATA ACQUISITION SYSTEM AND MEASUREMENT OF NEUTRON BACKGROUND AT THE KUO-SHENG NEUTRINO LABORATORY

by
Anıl SONAY

June, 2018
İZMİR

CHARACTERIZATION OF NEUTRON AND HIGH PURITY GERMANIUM DETECTORS WITH ADVANCED DATA ACQUISITION SYSTEM AND MEASUREMENT OF NEUTRON BACKGROUND AT THE KUO-SHENG NEUTRINO LABORATORY

A Thesis Submitted to the
Graduate School of Natural and Applied Sciences of Dokuz Eylül University
In Partial Fulfillment of the Requirements for the Degree of
Master of Science in Physics

by
Anıl SONAY

June, 2018
İZMİR

M.Sc THESIS EXAMINATION RESULT FORM

We have read the thesis entitled " **CHARACTERIZATION OF NEUTRON AND HIGH PURITY GERMANIUM DETECTORS WITH ADVANCED DATA ACQUISITION SYSTEM AND MEASUREMENT OF NEUTRON BACKGROUND AT THE KUO-SHENG NEUTRINO LABORATORY**" completed by **ANIL SONAY** under supervision of **PROF. DR. MUHAMMED DENİZ** and we certify that in our opinion it is fully adequate, in scope and in quality, as a thesis for the degree of Master of Science.

Prof. Dr. Muhammed DENİZ

Supervisor

Durmuş Demir	Saime Kerman
(Jury Member)	(Jury Member)

Prof. Dr. Latif SALUM

Director

Graduate School of Natural and Applied Sciences

ACKNOWLEDGMENTS

During the past two years, I have had a chance to work with many people whose accompanied me over the whole tenure of my M.Sc. To all of them I want to say Thank You!, for a wonderful time and great experience.

The graduate adventure of any student starts with his/her supervisor, I start by addressing a few words to Prof. Muhammed DENIZ, who supervised me over all these years and consciously guided the various steps during my M.Sc. He always been patient and helpful to me. Especially he was leading greatly to my routes on my troubled times. I can only express my sincere thanks to him.

I would like to express my great gratitude to Prof. Henry Tsz-King WONG, the spokesperson of the TEXONO collaboration. This thesis was created by his intelligent guidance and shed lighting on the challenging problems. His supportive touch on the subject with his deep insights has been leave a profound mark to mine. I am really grateful for his guidance, supports and great contribution on my experiences.

I would like to thank all TEXONO collaboration members, especially Lin Feng Kai, Chen Jin Han, Vivek SHARMA, Dr. Li Hau BIN, Dr. Lin Shin TED and Dr. Arun Kumar SOMA, as well as our group secretary Jingxuan SU for great kindness and making our life easier and smooth during stay in Taiwan. My special thank for Dr. Lakhwinder SINGH to contribution on my apprentice knowledge and being a great friend and great soul with his family.

I am grateful to my mom Güven Zengin CENGIZHAN and my father Alaattin CENGIZHAN. Their encouragement and supports led me to have great experiences and opportunities.

Last but not least, I would like to express my deep gratitude to my wife İpek Bingazi SONAY, a rare beauty, soul and intelligence who always assist and advise me through

all aspects. Without her blessings, this work could have never been materialized. Her existence on my side always give me immense strength and motivation to achieve my goal.

Anıl SONAY

CHARACTERIZATION OF NEUTRON AND HIGH PURITY GERMANIUM DETECTORS WITH ADVANCED DATA ACQUISITION SYSTEM AND MEASUREMENT OF NEUTRON BACKGROUND AT THE KUO-SHENG NEUTRINO LABORATORY

ABSTRACT

The rare event experiments for both in the new physics and the standard model studies such as; neutrino physics, weakly interacted massive particle (WIMP) investigations, neutrinoless double beta decay searches and so on, highly desires background suppression and understanding. Therefore in this study at the Kuo-Sheng Neutrino Laboratory (KSNL), two major components of background due to photon and neutron interactions were investigated with complete characterized high-purity Germanium (HPGe) detectors and a neutron detector with a hybrid structure (HND). HND and HPGe detectors were exposed with a data size of 33.8 and 347 days respectively to ambient and cosmic events under the same identical shielding configuration where the data acquisition system was designed in advanced level for labeling cosmic and ambient backgrounds. The measured nuclear recoil spectrum on HND is constructed into the fast neutron energy spectrum by an iterative unfolding method and projected into the Ge-recoil spectrum by Geant4 simulation. Thus, the background contribution due to neutron interaction with the measured photon background in HPGe spectra was obtained. Moreover, some X-ray emission lines of germanium due to neutron capture in HPGe detector were used to estimation of neutron flux, whose result proved that the measured and estimated neutron fluxes are consistent. Therefore, this method can be used for estimation on low energy and low background experiments in underground laboratories. The results are valuable to background understanding on the neutrino and WIMP studies at the KSNL. In particular, the ambient radioactivity due to neutron interaction is negligible compared to photon activity.

Keywords: Neutron background, radiation detection, scintillator, high-purity germanium detector, unfolding method, underground experiment, rare event searches

İLERİ VERİ TOPLAMA SİSTEMİ İLE NÖTRON VE YÜKSEK SAFLIKTA GERMANYUM DETEKTÖRLERİNİN KARAKTERİZASYONU VE KUO-SHENG NÖTRİNO LABORATUVAR ORTAMINDAKİ NÖTRON ARKA-ALAN ÖLÇÜMÜ

ÖZ

Standard model ve yeni fizik çalışmalarında nadir olay araştırmaları; nötrino fiziği, zayıf etkileşimli kütleli parçacık (ZEKP) ve nötrinosuz çift beta bozunumu araştırmalarında olduğu gibi, bu tür deneyler arka planın bastırılmasını ve anlaşılmasını güçlü bir şekilde arzularlar. Bu nedenle, Kuo-Sheng Nötrino Laboratuvarı'nda (KSNL) yapılan bu çalışmada, foton ve nötron etkileşimlerine bağlı olarak arka planın iki ana bileşeni tam karakterize edilmiş yüksek saflıkta Germanyum (HPGe) detektörleri ve hibrit bir yapıya (HND) sahip bir nötron detektörü ile araştırılmıştır. HND ve HPGe detektörleri, veri toplama sisteminin kozmik ve ortam arka planlarının etiketlenmesi için ileri düzeyde tasarlandığı aynı özdeş koruma konfigürasyonu altında, ortam ve kozmik olaylara sırasıyla 33.8 ve 347 gün veri boyutu ile maruz bırakıldı. HND üzerinde ölçülen nükleer geri tepme spektrumu, hızlı bir nötron enerji spektrumu içine iteratif açılım metodu ile yapılandırılmış ve Geant4 simülasyonu ile Ge-geri tepme spektrumuna yansıtılmıştır. Böylece, HPGe spektrumunda ölçülen foton arka plan ile nötron etkileşimi nedeniyle arka plan katkısı elde edilmiştir. Ayrıca, nötron akısının tahmininde HPGe detektöründe nötron yakalaması nedeniyle germanyumun bazı X-ışını emisyon çizgileri kullanılmış ve sonuçta ölçülen ve tahmin edilen nötron akısının tutarlı olduğu kanıtlanmıştır. Bu nedenle, tahmin metodu yeraltı laboratuvarlarındaki düşük enerjili düşük arkaplan deneylerinde kullanılabilir. Sonuçlar KSNL'deki nötrino ve WIMP çalışmaları hakkında arka plan anlayışı için değerlidir. Özellikle, nötron etkileşimine bağlı ortam radyoaktivitesinin foton aktivitesine kıyasla ihmal edilebilir olduğunu göstermektedir.

Anahtar Kelimeler: Nötron arka plan, radyasyon ölçümü, sintilasyon, yüksek saflıkta germanyum dedektörü, açılım metodu, yeraltı deneyi, nadir olay araştırmaları

CONTENTS

LIST OF FIGURES

Page

LIST OF TABLES

Page

CHAPTER ONE
INTRODUCTION

In the classical physics era, some of the unexplained phenomena like strange properties of light being, black-body radiation as well as photoelectric effect etc. had been directive to the invention of quantum mechanics. Newtonian mechanics and classical electromagnetism were not enough to resolve that anomalies and it is understood that, classical physics can be considered as an effective theory at low velocity regions and long distance and a more fundamental theory as quantum mechanics exists in atomic scale.

In the last century, with the discovery of nucleus and its constituents such as proton and neutron, the existence of new forces began to be considered beside of electromagnetic and gravitational forces. Moreover, the enhancements in technology allowed to design new experiments which could be causative to new particle discoveries. The interactions of newly discovered particles such as quarks and electron-like particles have been explained with strong and weak forces. In 1935, Yukawa and Fermi's models had been explain to strong and weak interactions which can be considered as the beginning of the modern particle physics era.

Quantum mechanics and the definition of the new interactions had been guide to new theories such as quantum chromodynamics (QCD) and quantum electrodynamics (QED) and by the unification of those theories standard model (SM) had been introduced. Nowadays, SM is very successful in explaining elementary particle interactions. However, the model can not give clear predictions on the questions of the description of dark matter, dark energy as well as the neutrino mass mechanism. In addition to that, SM does not fit with the neutrino oscillation mechanism. Hence, investigations on neutrino and dark matter become quite significant to clarify these questions and probe new physics beyond the standard model (BSM).

Neutrino and dark matter have poor interactions with matter due to the low event rate cross section in the SM, which makes it almost impossible to observe them. However, they can be observed directly by measuring nuclear or electron recoil energy when the neutrino scattering exists. Hence this kind of experiments can be achieved at low energy region with well understood background. With the understanding of the background contributions such as cosmic-contributed events or corresponding secondary events, experiment can be significantly enhanced to reach physical content.

1.1 Background Sources

In rare event researches, understanding the background sources and eliminating them is crucial. Therefore, the background distinction is needed to achieve intended physical subject by separating the events according to sources. In direct research of WIMP and neutrino, mostly the low energy region is taken into account. In this regime, there are two important sources, the photons and neutrons. The charged particles in low energy can not cross long distances inside the materials. So the charged radiations due to environmental sources or secondary produced particles can be easily shielded by materials. However, the neutral particles like neutron and photon sources become the main source for this kind of experiments at low energy regime.

1.1.1 Photon Background Sources

The photon radiation can be based on γ-ray due to de-excitation of the nuclei, which is excited from natural radioactive occurrence or activated isotopes by cosmic rays. Moreover, the X-ray sources by cosmogenic activation or the Bremsstrahlung radiation occurrence by charged particles can be considered as sources of photon. Understandably, we can differentiate all the sources to many pieces but dividing everything into many part may not be efficient. Hence, we can differentiate the sources into two different categories, which are the environmental radioactivity and the cosmic induced activity.

The natural radioactive isotopes such as ^{238}U and ^{232}Th and their constitutes by the radioactive cascades create environmental radioactivity in the materials and causes the ambient γ background. The decay chains of Uranium and Thorium series are shown in Figure 1.1, after which they respectively decay to stable lead isotopes (^{206}Pb) and (^{208}Pb) by α and β decays.

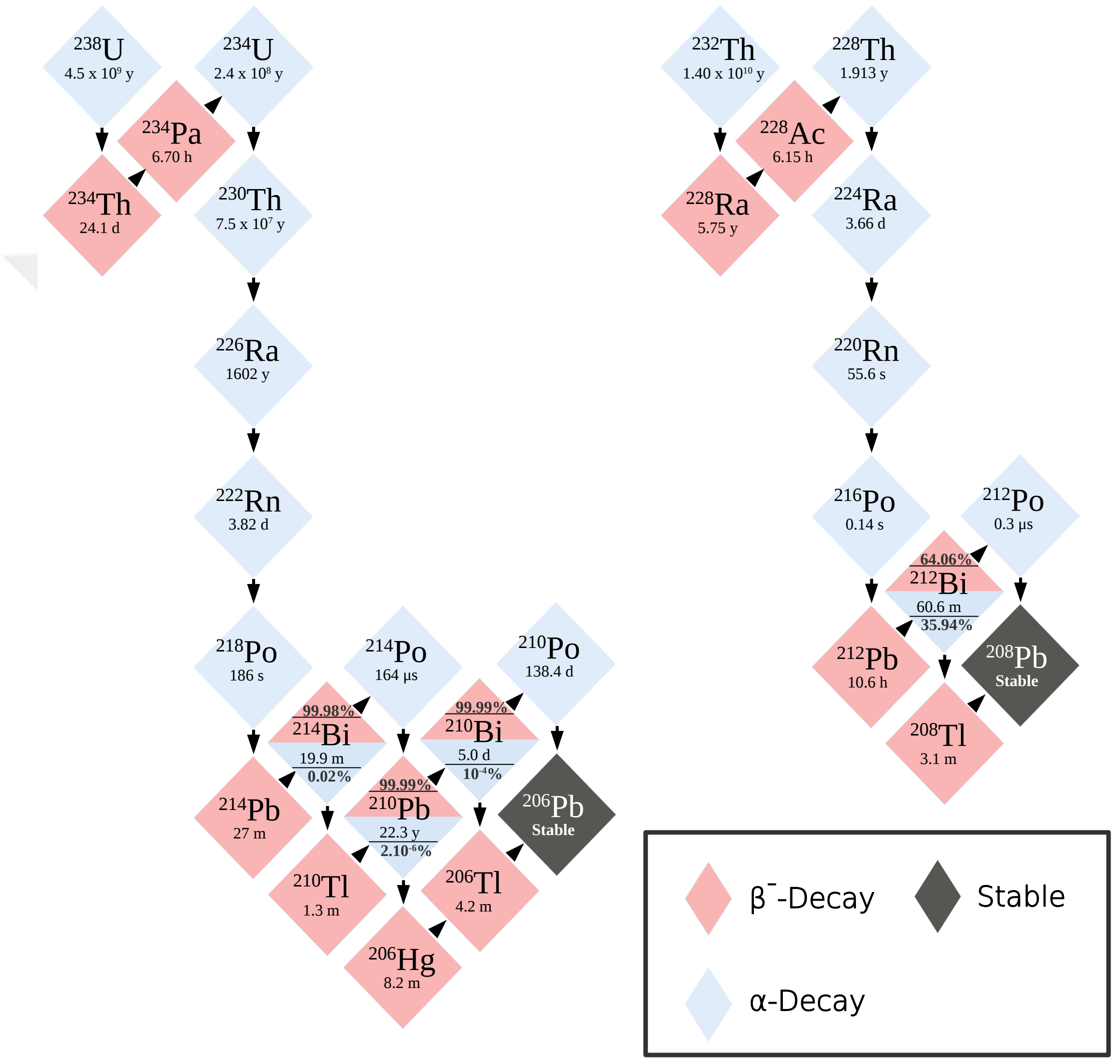

Figure 1.1 Uranium and Thorium decay chains

The γ de-excitation from Uranium and Thorium series is the main source of high energy photon production in the environment. Radon can be counted as an intermediate member of both series in the form of gas and it exists at earth surface with a rate of $\sim 6.2 \times 10^{-8}$ atoms m^{-2} day^{-1} (Ivanovich & Harmon, 1992). The ^{222}Rn as the longest-lived isotopes of radon with a half-life of $\tau_{1/2} = 3.8$ day is one of the strongest sources of airborne radioactivity and exists in laboratories at a radioactivity level of about 40 Bq cm^{-3} on an average (Heusser, 1995).

The isotope of potassium ^{40}K is ubiquitous and has a significant contribution to the background. Its abundance level is 0.0117% and decays primarily by β^- with 89.3% ratio and electron capture with 10.7% ratio by accompanied 1460.83 keV γ-ray.

Another isotopes ^{60}Co and ^{54}Mn, which are present at nuclear reactors, do also contribute to the photon background. Those isotopes emerge as air dust inside the building.

On the other hand, some long-lived isotopes activated by cosmic rays can decay by electron capture and cause the X-ray radiation as low energy photon production. These two channels can be appreciated as a main source of photon production for environmental radioactivity at every energy.

Secondary particles of cosmic rays can contribute directly to the background or indirectly by activation of isotopes. The fast cosmic neutrons induce dominantly the production of radionuclide inside the materials (Wei et al., 2017). This subject was and is still studied by many groups especially for rare event searches. This subject will be also reported in detail in Chapter 6 under configuration of experiment shielding system.

1.1.2 Neutron Background Sources

Neutron sources can be divided into two categories as in the previous section, the cosmic neutrons and ambient neutrons. Beyond that, neutrons have different classes according to their energy range. There are many definitions for neutrons but for convenience three classes will be used in this thesis as thermal (0-1 eV), epithermal (1 eV - 10 keV) and fast (10 keV-20 MeV) neutrons. A neutron during its traveling can be gradually thermalized by loosing its energy. So a fast neutron can reach as a thermal or epithermal neutron to the detector system, which means that all the energy must be considered. However, slow neutrons scattering process can be negligible due to undetectable recoil energy. Thus, observable neutron energy range would be different according to each detector's threshold.

Ambient neutrons are produced inside the materials by the natural spontaneous fission of ^{238}U and by (α,n) reactions with light elements initiated by α-particles from Uranium and Thorium series.

The high energetic cosmic muons can be a way for the fast neutron production by photo-nuclear reaction or photo-fission,

$$\mu^- + (Z,A) \rightarrow \mu' + (Z,A') + Xn + ... \tag{1.1}$$

These neutrons can be categorized as cosmic neutrons. Understandably, these neutrons are induced in the materials, which means the shielding materials can be sources for neutrons as well. Hence, inelastic scattering off muons must be well understood with the configuration of the materials of the shielding. This can be done by full GEANT simulation (Agostinelli, 2003; Mei & Hime, 2006).

1.2 Motivation and Goal of the Thesis

The goal of this thesis is to understand all the background sources as mentioned in Section 1.1 to reach physical contents as some given important subjects in Section 2.2 and the origins for future projects on rare event investigations like WIMP, neutrino and neutrinoless double beta decay searches.

However, eliminating all background signals in data is not possible for all particles, especially for neutrons as they only share part of their energy with the detector. But the partial energy spectrum of nuclear recoil of neutrons can be converted into neutron spectrum with developing some numerical methods. The contributions of neutrons can than be estimated by developing Monte Carlo simulation to subtract it from the actual data and physical data can be interpreted.

Consequently, the purpose of this thesis is to determine neutron background contribution on neutrino and WIMP candidate signals at Kuo-Sheng reactor neutrino laboratory (KSNL) on behalf of the Taiwan experiment on neutrino (TEXONO) research program.

CHAPTER TWO
EXPERIMENT SITE AND PHYSICS SEARCHES

Since its foundation in 1997, the TEXONO collaboration has focused on neutrino physics as well as astrophysics at low energy regime. The main focus of the collaboration is searching for interactions of neutrinos. On the other hand, together with the foundation of China dark matter experiment (CDEX) in China Jinping underground laboratory (CJPL), the first generation on dark matter searches had been started in China at low energy regime also. Collaboration consists of institutes from Taiwan, China, India and Turkey (Wong, 2015).

2.1 Kuo-Sheng Neutrino Laboratory

The KSNL is built at Kuo-Sheng nuclear power station II (KSNPS) situated at Jinshan district on the northern shore of Taiwan and located 10 m below (30 m.w.e) the ground level and 28 m far from core number one. The Power Plant has two cores separated at different buildings and 2.9 GW nominal thermal output for each core. The building and the laboratory location is shown in Figure 2.1.

A nuclear power reactor is the pure source for the electron anti-neutrinos ($\bar{\nu}_e$). In the center of the core the fuel of the fission is rich in terms of β^- decay and the $\bar{\nu}_e$ having energy up to 10 MeV is accompanied to each β^- decay. Total $\bar{\nu}_e$ production rate can simply be derived from the fission rate (N_f) which is defined as the ratio of the thermal power of reactor (P_{th}) to total thermal energy per fission (E_f). On an average 6.71 $\bar{\nu}_e$ are emitted in one fission and 205 MeV energy released per fission. Thus, typical neutrino yield per second at core can be defined as,

$$Y_{\bar{\nu}_e} = 6.71 \times N_f = \frac{6.71 \times P_{th} \times 10^9 J/s}{205MeV \times 1.602 \times 10^{-13} J/MeV} \ . \tag{2.1}$$

From Equation 2.1 approximately 2.0×10^{20} sec^{-1} $\bar{\nu}_e$ are emitted in a 4π solid

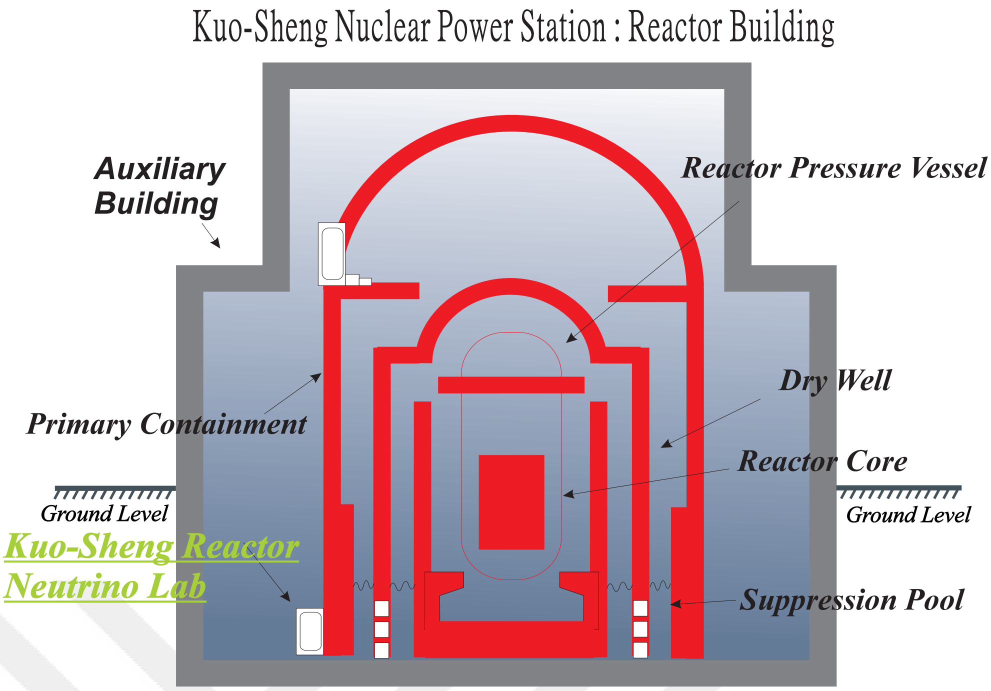

Figure 2.1 The schematic view (not drawn to scale) of the KSNL location in Kuo-Sheng nuclear reactor building (Wong, 2015)

angle from a 1 GW reactor. Therefore, in each core $\sim 6 \times 10^{20}$ sec^{-1} $\bar{\nu}_e$ are produced and by taking account to the 28 m distance from the center of the core, this number is reduced to 6.4×10^{12} cm^{-2}sec^{-1}.

Another important information is differential flux of the $\bar{\nu}_e$. A standard procedure to evaluate $\bar{\nu}_e$ spectrum is using the reactor operation data with a simulation software packages (Kuo, 2001; Tong, 2001). It is specifically developed with the association of commercial available software packages like SIMULATE-3 and CASMO-3 (Covington, 2001; Edenius, 1994). The rate of the fission is provided by KSNPS operation data for ^{235}U, ^{238}U, ^{239}Pu and ^{241}Pu at different position of the reactor core. The total $\bar{\nu}_e$ flux from different isotopes at different positions can be expressed as

$$\phi(\bar{\nu}_e) = \sum_{i,j} \frac{N_{ij}\phi_i(\bar{\nu}_e)}{r_j^2} , \tag{2.2}$$

where the "i" stands for the isotopes and "j" refers to the position of segment of fuel rod. Thus, a typical differential flux for $\bar{\nu}_e$ can be evaluated as is given in Figure 2.2.

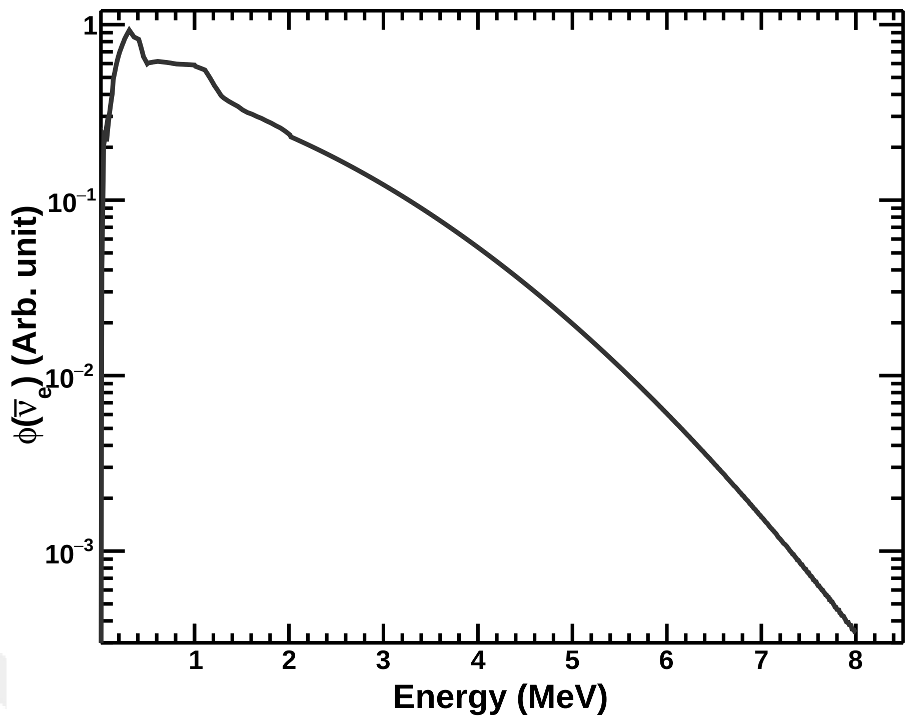

Figure 2.2 The differential flux for $\bar{\nu}_e$ at typical nuclear reactor operation (Wong, 2015)

2.2 Neutrino Studies on TEXONO Experiment

Neutrino interactions can be investigated under SM or BSM as an advance on new physics researches. Few important interaction outputs are discussed in this study such as neutrino electron scattering, neutrino magnetic properties and coherent elastic neutrino nucleus scattering (CENNS). Various Feynman diagrams in general form for of SM are shown in Fig 2.3. For the neutrino elastic scattering, there are two combinations of the diagrams which are charge current (CC) and neutral current (NC). Besides that, the CENNS contribution is only manifested by the NC diagram (See Appendix [A, B, C] to SM calculations).

2.2.1 Neutrino Electron and Antineutrino Electron Scattering

The differential cross sections of neutrino electron ($\nu_e - e$) and antineutrino electron ($\bar{\nu}_e - e$) scattering in the SM are given by Equation 2.3. The detailed calculations have

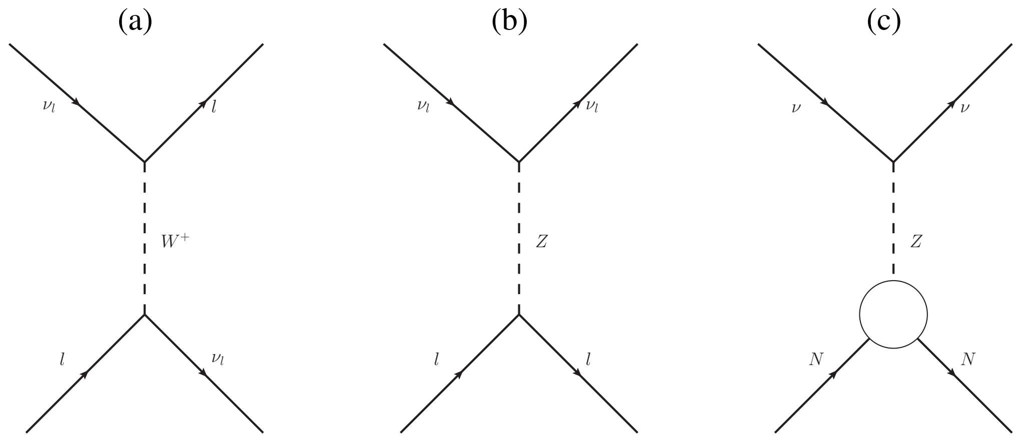

Figure 2.3 Feynman diagrams of $\nu_l - l$ elastic scattering by (a) neutral current (NC) (b) charge current (CC) and (c) of neutrino nucleus scattering $\nu_l - A$ CENNS

been derived in Apendix [A, B].

$$[\frac{d\sigma}{dT}(\nu_e(\bar{\nu}_e)e)]_{SM} = \frac{2G_F^2 m_e}{\pi E_\nu^2}\left(a^2 E_\nu^2 + b^2(E_\nu - T)^2 - abm_e T\right) \ , \tag{2.3}$$

where G_F represents the Fermi coupling constant. T is the kinetic energy of relative electron, E_ν represents the incident neutrino energy and the coefficient constants a and b are given in Table 2.1. Here, the axial vector coupling constants g_V and g_A are defined in terms of weak mixing angle as $-1/2 + sin^2\theta_W$ and $-1/2$ respectively.

Table 2.1 The SM coefficient expressions for differential cross section of $\nu_e - e$ and $\bar{\nu}_e - e$ given in Equation 2.3

Coefficients	$\nu_e - e$	$\bar{\nu}_e - e$
a	$(g_V + g_A + 2)/2$	$(g_V - g_A)/2$
	$sin^2\theta_W + 1/2$	$sin^2\theta_W$
b	$(g_V - g_A)/2$	$(g_V + g_A + 2)/2$
	$sin^2\theta_W$	$sin^2\theta_W + 1/2$

The differential cross section is given for various incident neutrino energies in Figure 2.4 (a), which is concerned with Equation 2.3, and the total cross section is given in Figure 2.4 (b) as integral form of the differential cross section. Further, 1 MeV threshold effect is also shown in the figure. For the total cross section, lower limit of the integral represents the threshold of the detector. Because each experiment has its own

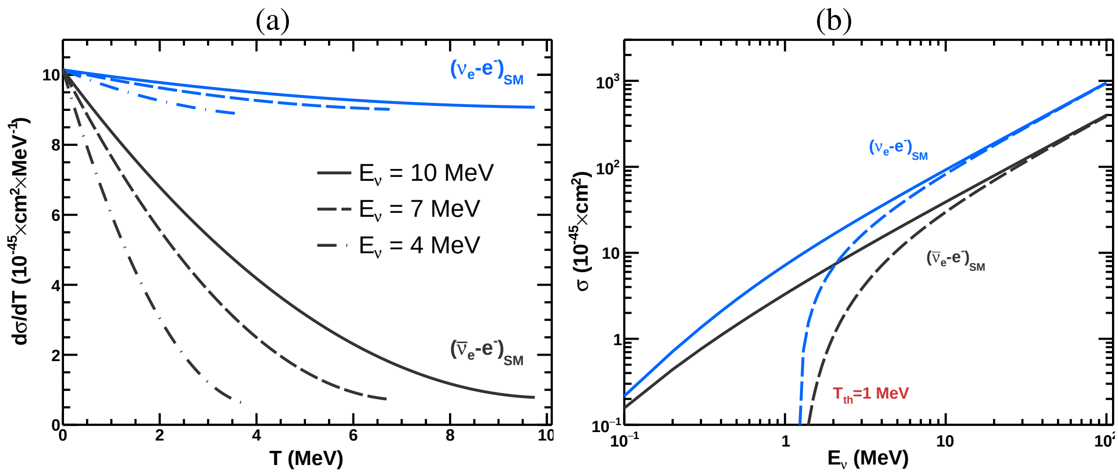

Figure 2.4 (a) The recoil energy spectra of the $\nu - e$ scattering for the various neutrino energies. (b) Total cross section of $\nu - e$ scattering. Dashed line expresses total cross section with 1 MeV threshold

threshold, this effect of the threshold should be attended according to the experiment. The differential cross section of $\nu_e - e$ is dominated by CC term which is proportional to incident neutrino energy while that of $\bar{\nu}_e - e$ is dominated by NC term which is proportional to scattered neutrino energy. This is the reason behind the difference between differential cross sections as it is clearly seen by Figure 2.4.

2.2.2 Neutrino Magnetic Moments

The neutrino electron scattering can be discussed on a framework of the new physics interaction via neutrino magnetic moment, which is usually expressed in units of the Bohr magneton (Equation 2.4)

$$\mu_B = \frac{e}{2m_e}; \qquad e^2 = 4\pi\alpha_{em} \ , \tag{2.4}$$

where m_e is the electron mass and α_{em} is the fine structure. The unknown vertex factor can have some achievement on new physics investigations. Especially, discussion of neutrino magnetic moment can help to understand Dirac and Majorana neutrinos. The SM with massive Dirac neutrinos gives small value for $\mu_\nu \backsim 10^{-19}[m_\nu/1eV]\mu_b$ which has no chance in any observation (Fujikawa & Shrock, 1980). On the other hand, Majorana neutrino transition moments can significantly raise μ_ν to the experimentally relevant ranges (Barr, 1990). According to this motivation, observation of finite number of neutrino magnetic moment would be strong signal for Majorana neutrinos.

The neutrino magnetic moment for neutrino energy E_ν after traveling distance L is given by Equation 2.5

$$\mu_\nu^2(\nu_l, E_\nu, L) = \sum_j |\sum_i U_{li} e^{-iE_\nu L} \mu_{ij}|^2 , \tag{2.5}$$

where U_{li} is the neutrino mixing matrix and μ_{ij} are the coupling constants with photon

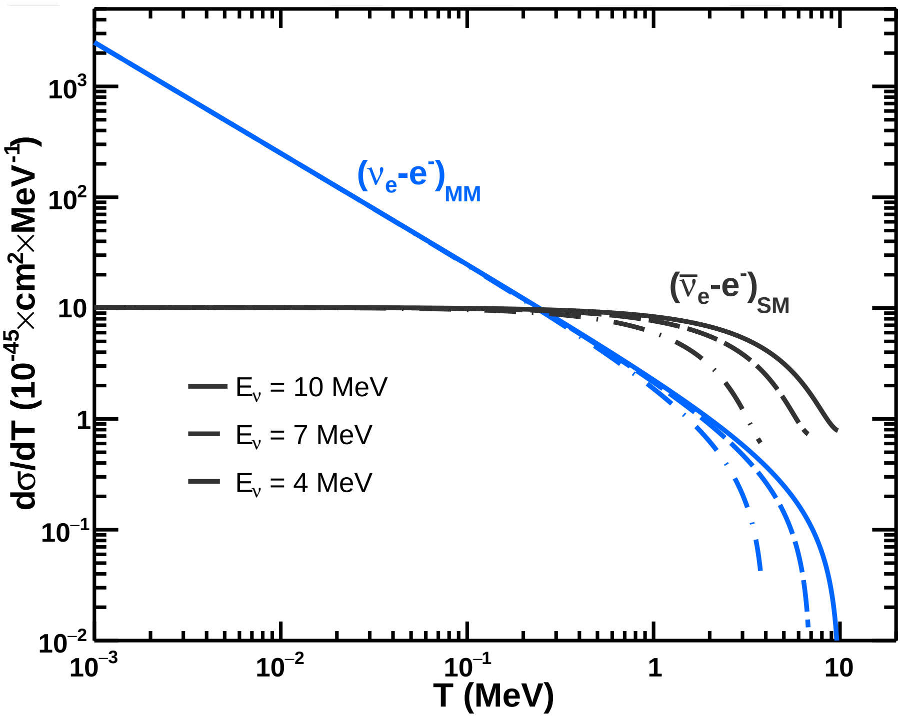

Figure 2.5 The differential cross section for neutrino magnetic moment which is given in Equation 2.6 and standard model of the anti-neutrino elastic scattering

between ν_i and ν_j. As a direct laboratory experiment, antielectron neutrino scattering with the electron recoil kinetic energy (T) can be observed for neutrino magnetic moment by using reactor neutrino sources. The differential cross section is given in Equation 2.6

$$\left(\frac{d\sigma}{dT}\right)_{\mu_\nu} = \frac{\pi\alpha_{em}^2\mu_\nu^2}{m_e^2}\left[\frac{1-T/E_\nu}{T}\right] . \tag{2.6}$$

As seen in Figure 2.5, the differential cross section for given Equation 2.6 is quite higher at 1-100 keV energy range. This opportunity constitutes great laboratory to investigate the neutrino magnetic moment properties and probe new physics.

2.2.3 Coherent Elastic Neutrino Nucleus Scattering (CENNS)

In the CENNS process, low energy neutrinos interact with the protons and neutrons in the nuclei coherently, which significantly enhances the cross section. It provides also important laboratory to study the quantum mechanical coherence effects in electroweak interaction and probe new physics as well (Barranco & Miranda, 2002). The CENNS process is also phenomenologically important for future dark matter direct detection experiments and astrophysical researches (Billard, 2013; Freedman, 1974).

The differential cross section of the CENNS in SM is given by Equation 2.7 (Papoulias & Kosmas, 2015) (See for details Appendix C)

$$\left[\frac{d\sigma}{dq^2}(q^2, E_\nu)\right]_{CENNS} = \frac{1}{2}\left(\frac{G_F^2}{4\pi}\right)\left(1 - \frac{q^2}{4E_\nu^2}\right)\left[\varepsilon Z F_Z(q^2) - N F_N(q^2)\right]^2 , \tag{2.7}$$

which is expressed in the three momentum transfer ($q \equiv |\overrightarrow{q}|$) as given by $q^2 = 2MT + T^2 \cong 2MT$. Here, E_ν is the incident neutrino energy and T is the observable nuclear recoil energy. $F_Z(q^2)$ and $F_N(q^2)$ are respectively the nuclear form factors for proton and neutron. $\varepsilon = (1 - 4sin^2\theta_W) \simeq 0.045$ remarks that the dominant contribution is from the neutrons. The calculations have adopted equal form factors for neutrons and protons as is assumed in (Engel, 1991) (Equation 2.8)

$$F(q^2) = \left(\frac{3}{qR_0}\right) J_1(qR_0) e^{(-q^2 s^2/2)} , \tag{2.8}$$

where $J_1(x)$ is the first order spherical Bessel function, $s = 0.5$ fm, $R = 1.2A^{(1/3)}$ fm and $R_0 = R^2 - 5s^2$. The form factor and the differential cross section of CENNS is shown in Figure 2.6 for different heavy nuclei (Xe, Ge, Ar), which are the popular detectors for dark matter and neutrino researches.

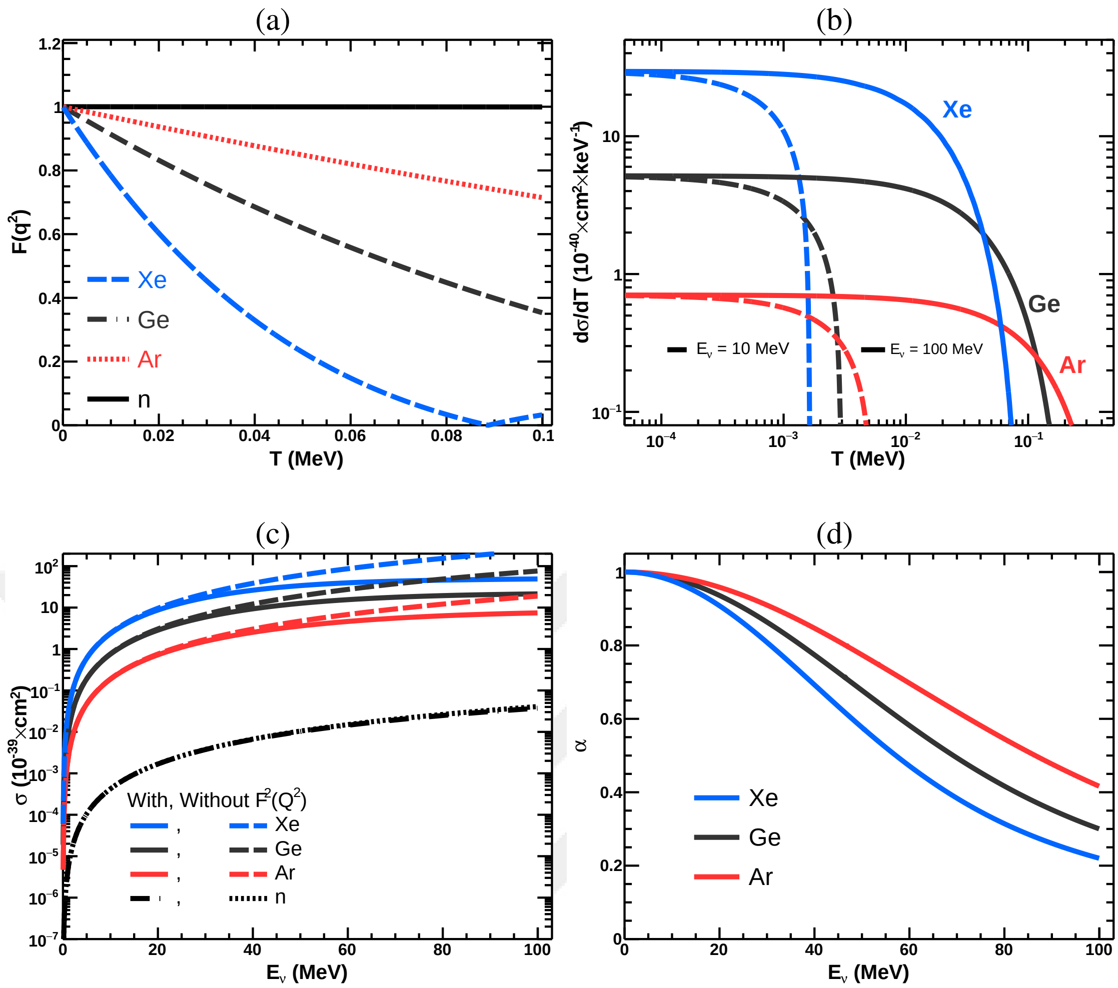

Figure 2.6 (a) Nuclear form factor given in Equation 2.8. (b) The differential cross section and (c) total cross section with and without form factor for CENNS. (d) Coherency factor against neutrino energy for different nuclei

At the limit of $T \to 0$ and $F(q^2) \to 1$, elastic scattering occurs with full coherence and the total cross section gets maximum value. Hence, coherence is related to $(\varepsilon Z - N)^2$ and Equation 2.9 is derived by this motivation for coherence factor defined as α,

$$\frac{\sigma(Z,N)}{\sigma(0,1)} = \left\{Z\varepsilon^2[1+\alpha(Z-1)] + N[1+\alpha(N-1)] - 2\alpha\varepsilon ZN\right\} . \tag{2.9}$$

The α factor ensures good discussion for constraints of the coherence level for different kind of neutrino sources. The limit of $\alpha \to 1$ can be accepted as full coherence and it has good efficiency at low recoil energy. Thus, we are accepting that the reactor

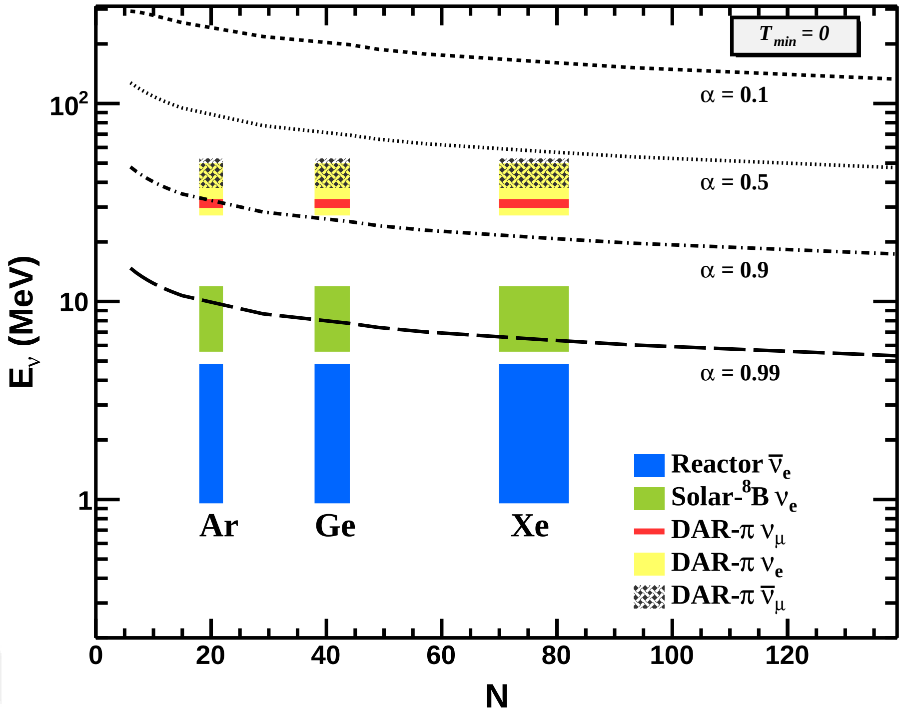

Figure 2.7 The α contours for different target nuclei in the unit of proton number projected to neutrino energy for different neutrino sources

neutrinos have provided excellent laboratory to observe CENNS and as seen in Figure 2.7 it is full coherent. However, observation of the CENNS from the reactor neutrino channels is quite difficult due to very low recoil energy and quenching effects of the detectors for the nuclear recoil.

2.3 Summary and Conclusion

The discussed differential cross section in the upper section can be converted to the event rate for known reactor neutrinos. To understand the constraints of interactions and predict proper experimental setup for relative interactions, we need to integrate differential cross section over the flux of neutrinos as is given in Equation 2.10

$$R_\chi = \rho_e \int_T \int_{E_\nu} \left[\frac{d\sigma}{dT}(E_\nu, T) \right]_\chi \frac{d\phi_\nu(E_\nu)}{dE_\nu} E_\nu \ , \tag{2.10}$$

where R_{χ} is event rate for relative χ interaction, ρ_e is the electron density for target material per kg unit, $\phi_{\nu}(E_{\nu})$ is the neutrino flux. The three interactions which are discussed at the earlier section have been shown in Figure 2.8 .

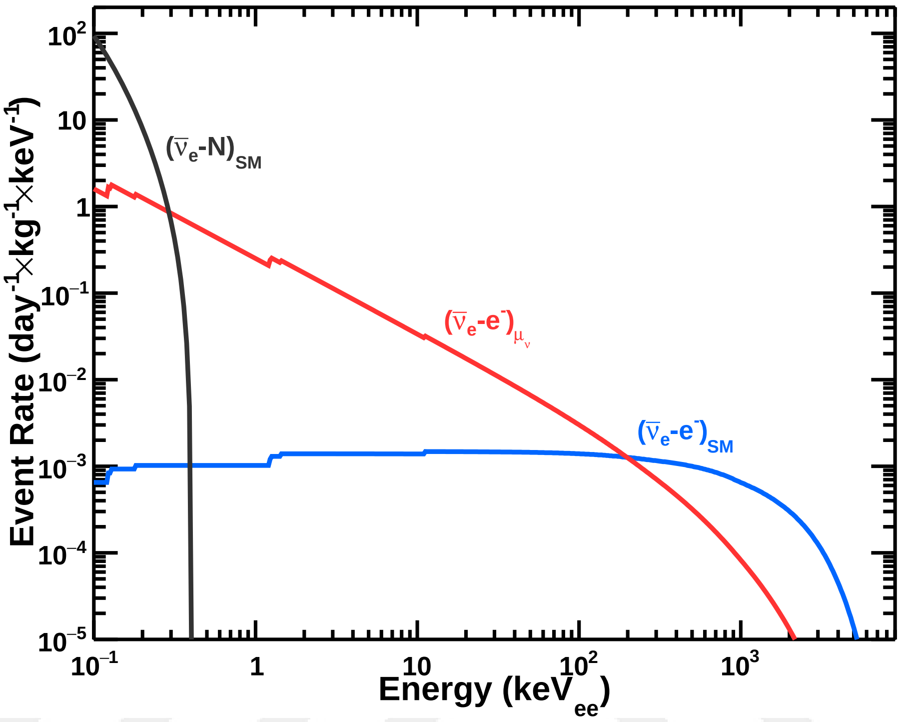

Figure 2.8 Event rate of discussed interactions for antineutrino flux

In the past, data was taken by large-target mass CsI(Tl) detector (see Figure 2.9) due to the rare interaction of neutrino electron scattering in SM, as is seen in Figure 2.8. The results are obtained at 3-8 MeV_{ee} energy range for reactor on/off 29882/7369 kg-days. On/off data residual spectrum is shown in Figure 2.10 (a) and the ratio between experimental measured values and theoretically estimated values was measured as follows (Deniz, 2010)

$$\frac{R_{expt}(\nu)}{R_{SM}(\nu)} = 1.08 \pm 0.21(stat) \pm 0.16(sys) \ . \tag{2.11}$$

In addition, the interference effect can be expressed by the following equation

$$R_{expt} = R_{CC} + R_{NC} + \eta \cdot R_{int} \ , \tag{2.12}$$

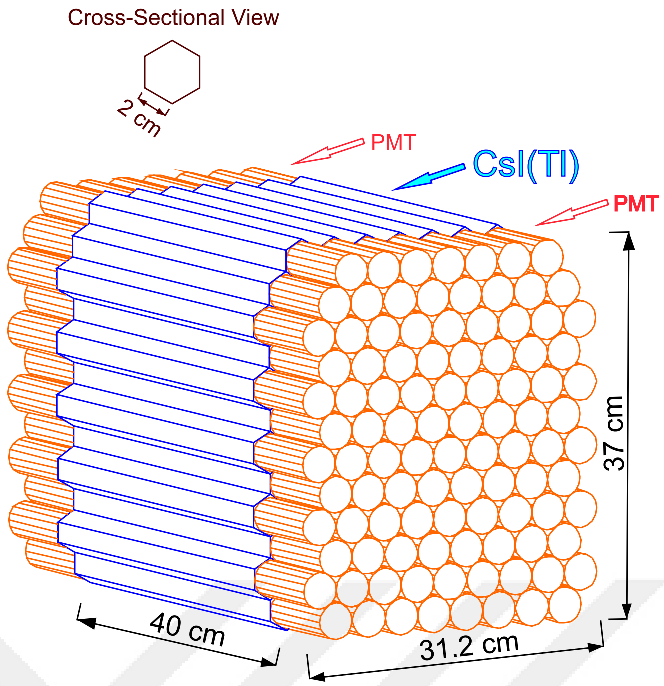

Figure 2.9 The schematic view of CsI crystal arrays (Figure is adapted from (Deniz, 2010))

where the parameter η is a measure to test SM prediction. The measured value of the η parameter is same with SM prediction $\eta(SM) = -1$ as is shown in Figure 2.10 (b) (Deniz, 2010).

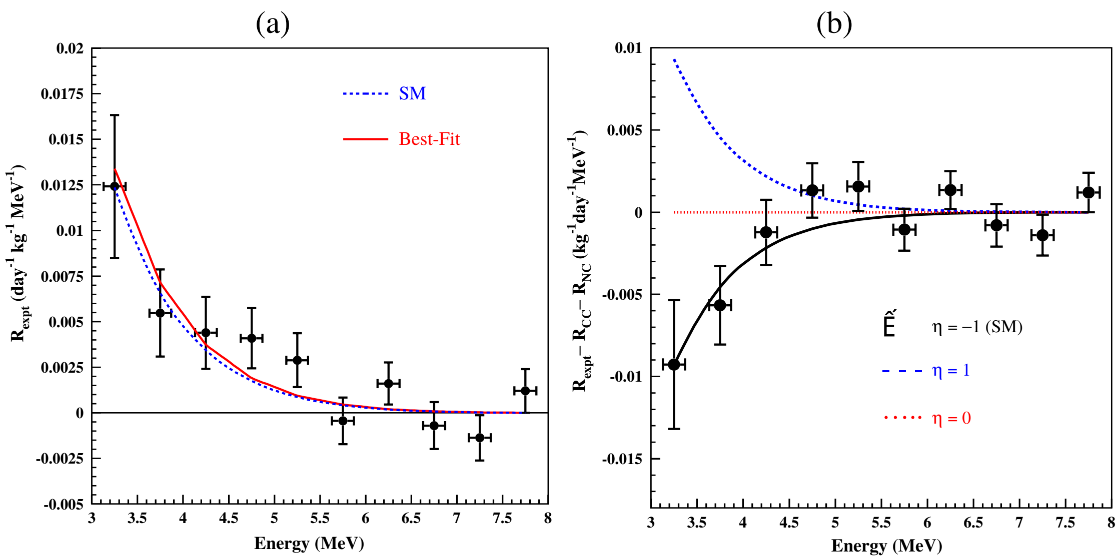

Figure 2.10 (a) The residual spectrum and the SM best fit. (b) The interference term sitting in SM prediction of $\eta = -1$ (Figure is adapted from (Deniz, 2010))

Another measurable parameter is the weak mixing angle which was measured as $sin^2\theta_W = 0.251 \pm 0.031(stat) \pm 0.024(sys)$

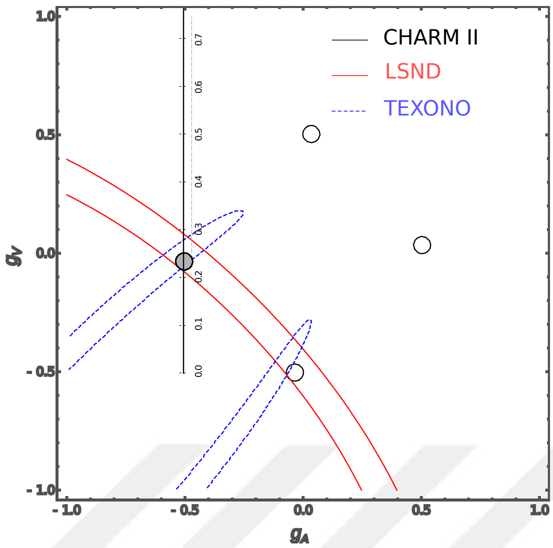

Figure 2.11 Allowed contours in g_A vs. g_V according to interactions of $\nu_e e$, $\bar{\nu}_e e$ and $\nu_\mu(\bar{\nu}_\mu e)$ from LSND, TEXONO and CHARM II experiments, respectively (Figure is adapted from (Tanabashi et al., 2018))

The allowed region on (g_V, g_A) space as a function of $sin^2\theta_W$ for $\nu_e e$, $\bar{\nu}_e e$ and $\nu_{mu}(\bar{\nu_{mu}} e)$ interactions from LSND, TEXONO and CHARM II experiments are illustrated in Figure 2.11. Result from these experiments agree in one point which is constraint the best limits for $sin^2\theta_W$ measurement (Tanabashi et al., 2018).

Due to higher cross section of neutrino magnetic moment and CENNS at lower energy, high-purity germanium (HPGe) detectors have excellent resolution to observe these interactions. Based on Figure 2.8, the $\bar{\nu}_e - e^-$ scattering via photon mediator has higher event rates at 10-100 keV energy range compared to the weak process. However, this range is not practicable for scintillator detectors. Therefore, Germanium detector has been used to measure neutrino magnetic moment properties and reactor on/off data has been taken for 570.7/127.8 days. Respectively the limit at 90% confidence level (C.L.) was put as follows Wong (2015)

$$\mu_{\bar{\nu}_e} < 7.4 \times 10^{-11}\ \mu_B\ . \tag{2.13}$$

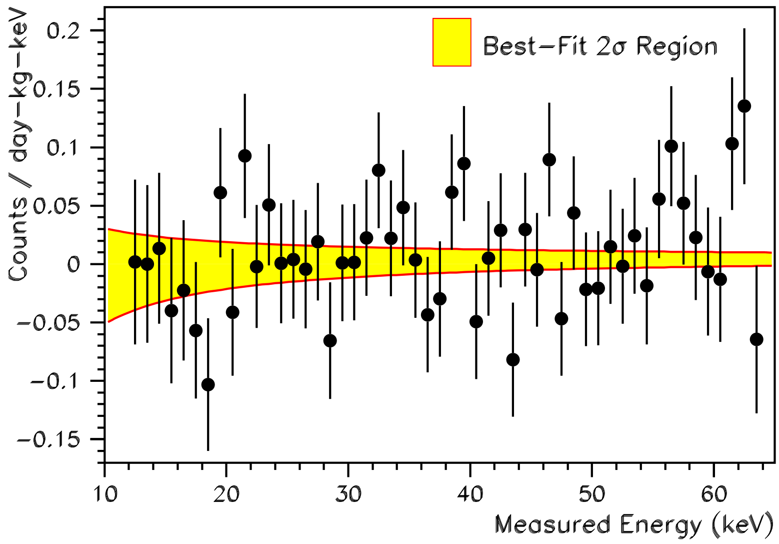

Figure 2.12 The allowed 2σ band on the search of the neutrino magnetic moment for the residual combined reactor on/off data (Figure is adapted from (Wong et al, 2007))

The given result probed the neutrino spin-flavor precession (SFP) mechanism at the relevant range to the solar neutrino problem (Barranco & Miranda, 2002; Wong et al, 2007). The residual on/off data spectrum and the 2σ band are shown in Figure 2.12.

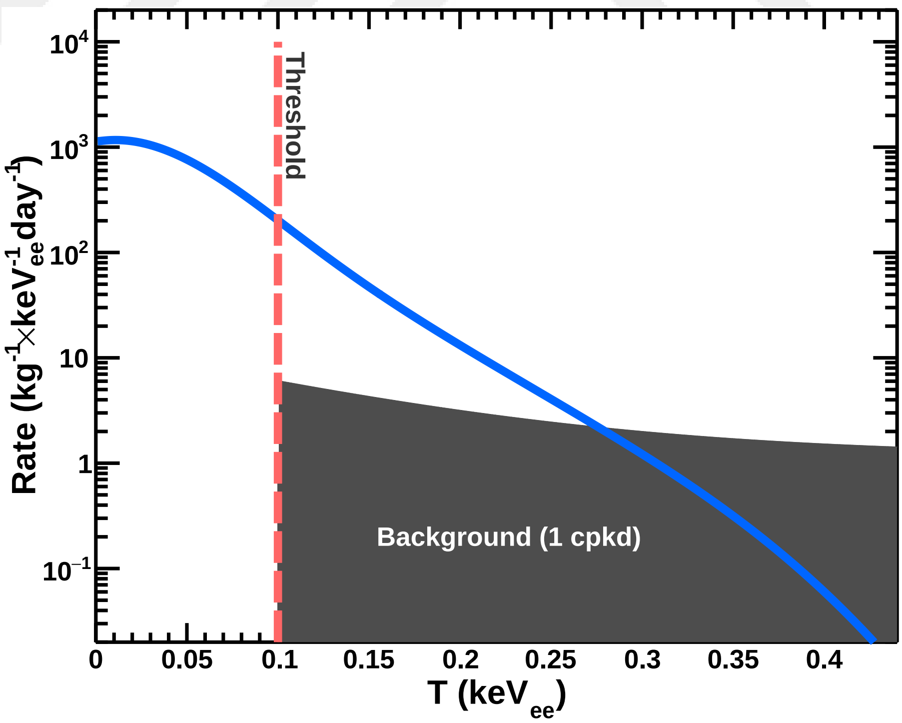

Figure 2.13 The CENNS event rate for reactor neutrinos. Resolution and quenching effects has been taken account in this example

The TEXONO research program has focused currently on CENNS for reactor neutrinos. As obtained in the previous section, the reactor neutrinos are fully coherent and as is shown in Figure 2.8 (b), CENNS has significantly higher event rate as had never been seen for weak process. This opportunity constitutes great laboratory to probe new physics researches and understand neutrino mechanism. However, the CENNS process needs to have low threshold and low background which is already a difficult problem. On the other hand, the enhancements in technology have lead to record >100 keV threshold for TEXONO group with new electro-cooling p-type point contact Ge (ECPPC) detector. As is shown in Figure 2.13, the TEXONO collaboration targets to achieve 1 count per kg-day (cpkd) of background and 100 eV threshold (the shown background in the figure has been given arbitrary as an example).

CHAPTER THREE
EXPERIMENTAL DESIGN

3.1 Background Suppression

Reducing the background for rare event searches is crucial to reach physical goal as mentioned in previous sections. So, each experiment will have its own setup by considering each physical investigation, experiment location and the conditions. Therefore, typically, deep underground laboratories are desired to avoid cosmic induced radioactivity. However, if the laboratory is not deep enough as is similar to the KSNL, another systems are required to discriminate and suppress the background. According to this motivation, the KSNL has passive and active shielding designs.

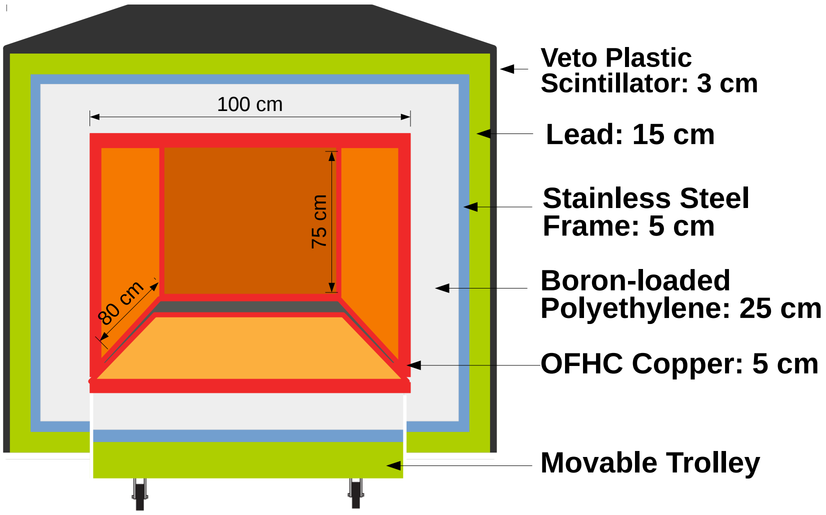

Figure 3.1 The schematic view of the shielding design for KSNL

In order to reduce local and cosmic radioactivity, the main volume with 100 cm $\times$ 80 cm $\times$ 75 cm is surrounded by 50 ton shielding as seen in Figure 3.1. The shielding contains lead, steel, boron-loaded polyethylene and oxygen-free high-conductivity (OFHC) copper for attenuation of the γ-ray background as well as the neutron background. The lead (Pb) at the outer side with 15 cm is superior material for shielding. However, it is also causative to muonic-induced Bremsstrahlung and secondary neutron radiation. Therefore, in a good agreement, 10-15 cm is adequate to reduce the ambient γ-ray activity without causing another kind of radioactivity. Moreover, the next materials as stainless steel and boron-loaded polyethylene will also reduce the muon-induced activity on Pb. Final material OFHC copper has role to reduce photon background due to nuclear excitation in upper materials.

In Figure 3.1, on the upper side, there are veto plastic scintillators with 3 cm thickness. On the top, there are four plastic scintillators and all around the side walls there are three of them. In total, there are twelve side panels and four top panels. These plastic scintillators are the part of the active shielding system and the schematic diagram of them is drawn in Figure 3.2(a).

The photomultiplier tubes (PMT) are connected to each plastic scintillator as is shown in Figure 3.2(b). At the top, left and right sides, each scintillator has four PMT connection as two on head side and two on end side. For the back and front side only two PMT connections are available for each scintillator. The top side plays major role to identify cosmic signals, therefore readout system is controlled by three logic circuits for each of them and side panels are connected to readout system with a specific logic. The schematic diagram is shown in Figure 3.3 and the description for three logic circuits is as follows;

2/4 logic (2/4): It is fired if two or more PMT have signal above the threshold.

Both side logic (BSL): System is triggered if the PMTs on both sides have signal above the threshold.

Q-logic (QL): If the voltage (amplitude) and charge from the signal are satisfied above the threshold, then system is triggered.

Trigger rate from the plastic scintillators is on average 5 kHz. Significant cosmic ray contribution comes from four top panels with 12 m^2 area as 2 kHz event rate and 1 kHz contribution from other twelve side panels. The remaining 2 kHz is related with γ-background and electronic noise. The detection efficiency is also tested by

(a)

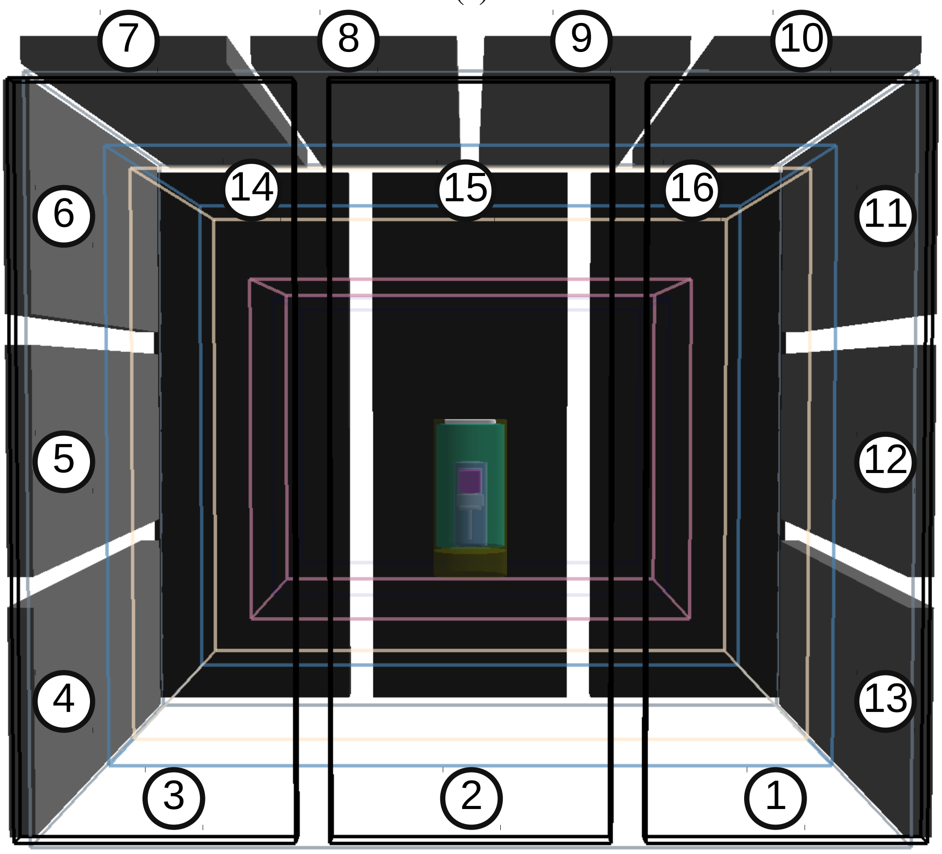

(b)

Figure 3.2 (a) The complete geometry of shielding system created in Geant4 package. Gray solid panels with numbers presents to 16 plastic scintillators, coloured line shows the passive shielding as seen in Figure 3.1 and the pink tube is the target inside the NaI(Tl) detector well. (b) The picture of shielding outside is showing photomultiplier tubes (PMT) connection to plastic scintillators and the control room is located immediately the left its

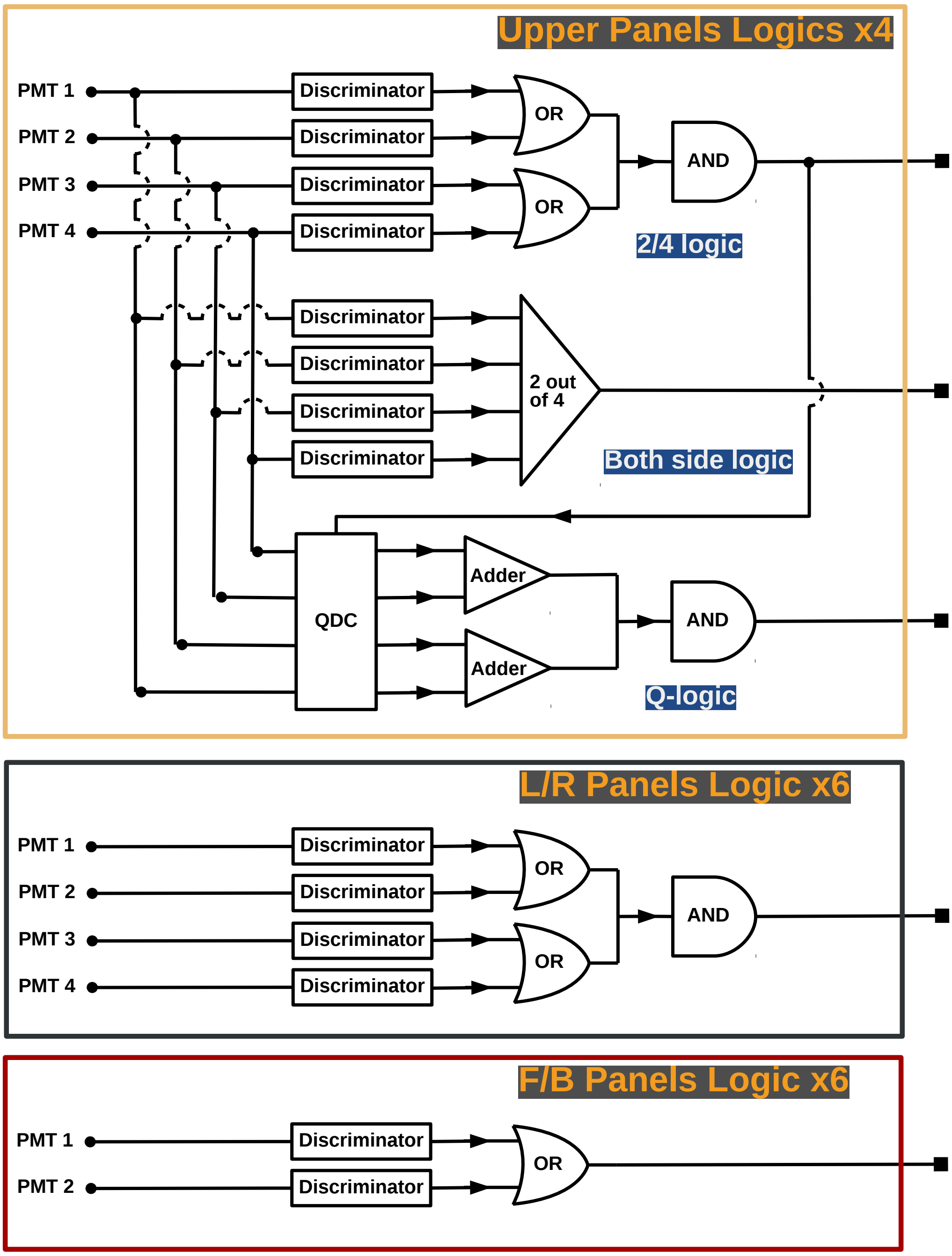

Figure 3.3 The schematic diagram of logic circuits of cosmic veto panels. Here the upper, left-right (L/R) and front-back (FB) represents the panel positions according to Figure 3.2(a)

NaI(Tl) scintillator inside the volume. High energy cosmic muons create a pure signal in NaI(Tl) detector. Thus, the coincidence events with NaI(Tl) and the cosmic panels show that plastic scintillators have 92% efficiency. The complete cosmic ray (CR) veto system provides time information between panel and main detector and this information is categorized as CR$^{\pm}$, here the "+" presents coincidence and "-" anti-coincidence conditions for cosmic ray hit.

At the inner side, there is another active shielding system using NaI(Tl) detector for anti-Compton (AC) shield. It provides energy and time information which consequently gives good opportunities for offline analysis. As is similar to CR tags to events, NaI(Tl) detector is also categorized as AC$^{\pm}$ for coincidence and anti-coincidence cases. At the bottom of the detector there is a well to cover the main detector. The schematic diagram of the inner side with an AC and the main detector is shown in Figure 3.4.

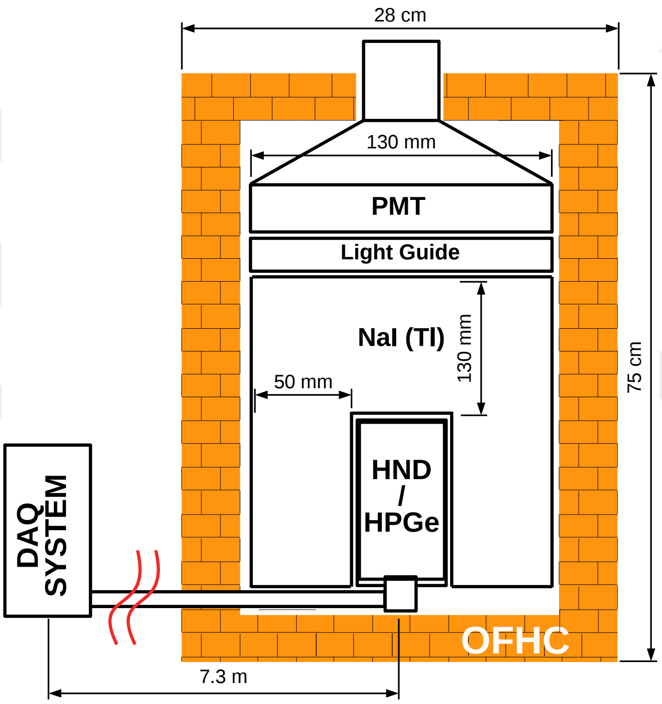

Figure 3.4 The schematic view of the inner target design with an anti compton detector (NaI(Tl)) and a main detector

The main detector in the experiment is HPGe and the entire system works based on its self-trigger. HPGe detectors have great opportunities due to their great energy resolution response and low threshold effects. On the other hand, a hybrid neutron detector (HND) having similar dimension with HPGe is performed in the experiment site by installing it in place of HPGe within the well of NaI(Tl) to understand neutron background *in situ*.

3.2 Germanium Detectors

The first practicable germanium detector was developed by using Lithium-ion drift compensation technique in 1963. The technique was invented by E. M. Pell in 1960 (Pell, 1960). The first Lithium-ion drift germanium Ge(Li) detectors were a revolution in γ-spectroscopy due to fifty time better energy resolution than NaI scintillators. However, despite its superior performance, Ge(Li) detectors must be kept at liquid nitrogen temperature from fabrication till operational duration. Once the detector reach room temperature, its basic structure gets damaged and becomes impracticable. In the next two decades after invention of Ge(Li) detectors, HPGe detectors were invented which, as opposed to Ge(Li), can stay in room temperature. Thus, HPGe detectors take widely using range for many applications nowadays.

The representative configuration of germanium detectors are planar and co-axial, however many others have various configurations. Their schematic view is shown in Figure 3.5. Point contact planar germanium detector has higher energy resolution and low threshold according to co-axial configuration. Especially, investigations showed that p-type point-contact germanium (pPCGe) detector energy resolution is significantly improved recently (Barbeau, 2007). Thus pPCGe has great opportunities for low energy experiments. On the other hand, in 1989, a successful n-type point-contact germanium (nPCGe) detector has been demonstrated (Luke, 1989). The inner contact has been shrunk into small size of disk in this configuration and detector capacitance reduced by large factor. As a consequence, those nPC and pPC Ge detectors are valuable for testing low-energy low-background experiments for rare event searches.

The clusters of charge carriers created at the site of interaction migrate towards the respective electrodes under the influence of electric field. The charge carrier movement induces current inside the detector. This current can be calculated by Shockley-Ramo theorem (Zhong, 2001). According to this theorem, current will be as follows

$$I = q\, v_d \cdot E_w \,, \tag{3.1}$$

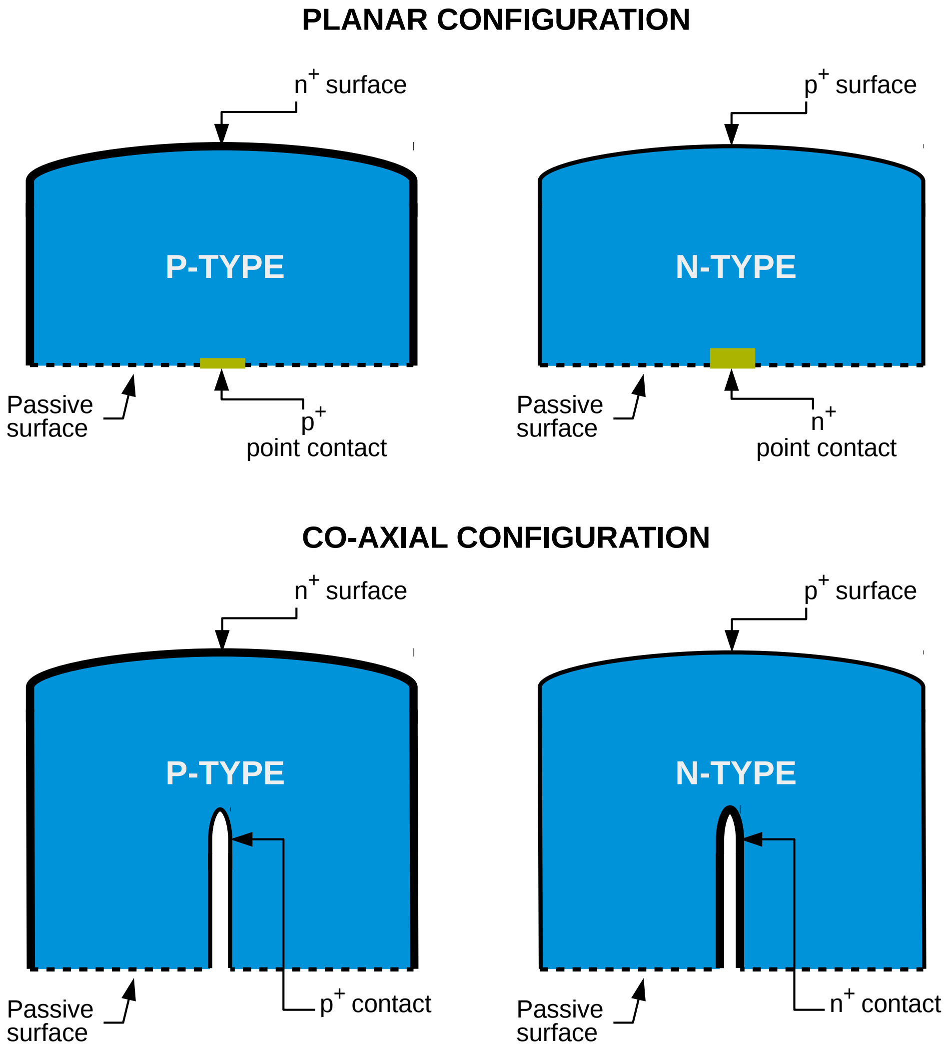

Figure 3.5 The schematic view for the planar and co-axial germanium detector configurations

where the q is charge, v_d is drift velocity and E_w is weighting field strength. Understanding the weighting potential and the charge drift in the field also provides the signal information. This opportunity has been used as pulse shape analysis (PSA) technique by various experiments. In this technique, energy depositions and interaction positions can be identified by Geant4 Monte Carlo simulation tool (Agostinelli, 2003). The pulse shape simulation is carried out by m3dcr and siggen software on created weighting potential (Radford, 2014). Thus, each simulated pulse is compared event-by-event with χ^2-fitting and as a consequence multi-site events rejected by 99% can be obtained (Cooper, 2011).

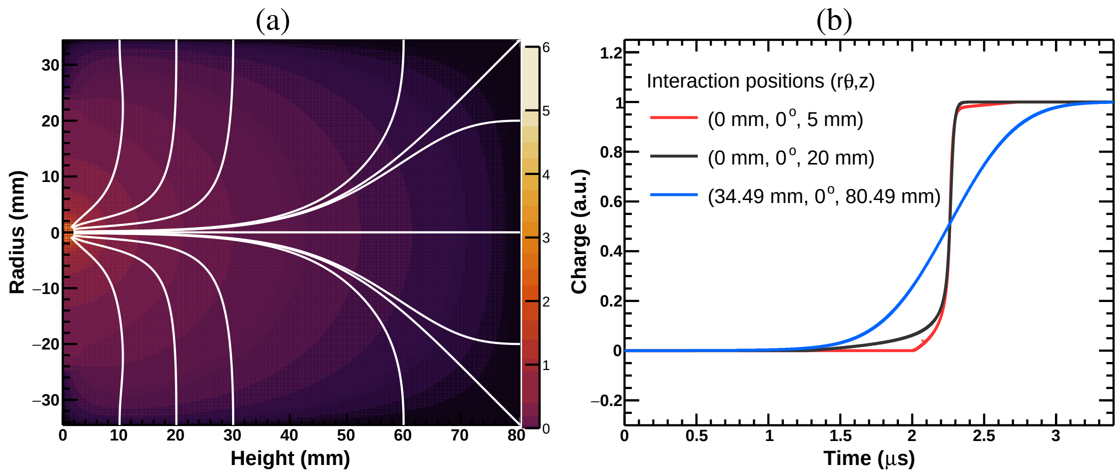

Figure 3.6 (a) Weighting potential distribution for 60 mm × 80 mm height pPCGe detector. White lines shows the charge carrier drifts from interaction point till point contact. (b) Pulse shape simulation according to different interaction position for given detector geometry and weighting potential in (a)

As an instance, in Figure 3.6, weighting potential distribution in 60 mm × 80 mm pPCGe and the charge carriers path from interaction to point contact, and the simulated pulse shapes at different interaction positions are shown. In practice and simulation, main difference among the pPCGe and nPCGe is the interaction position dependence of pulse shape in pPCGe.

3.2.1 Signal Processing and Experimental Setup

The signal processing on both nPCGe and pPCGe is provided first by preamplifier as an interface between the detector and signal processing electronics. Signals from germanium crystals are first amplified by front-end JFETs, then the charge in capacitance of the semiconductor detector is reset by preamplifier. The signal from the preamplifier can be shaped into another form and amplified by analog devices to acquire the desirable data. To digitize the signal, analyzing the trigger is also important. Thus, digitized signal can be saved into digital environment. This signal process is known as data acquisition (DAQ) and the simple DAQ circuit for germanium detector is shown in Figure 3.7(a). The raw signal from the direct output of preamplifier as illustrated in Figure 3.7(b), each reset time preamplifier creates signal as inhibit signal

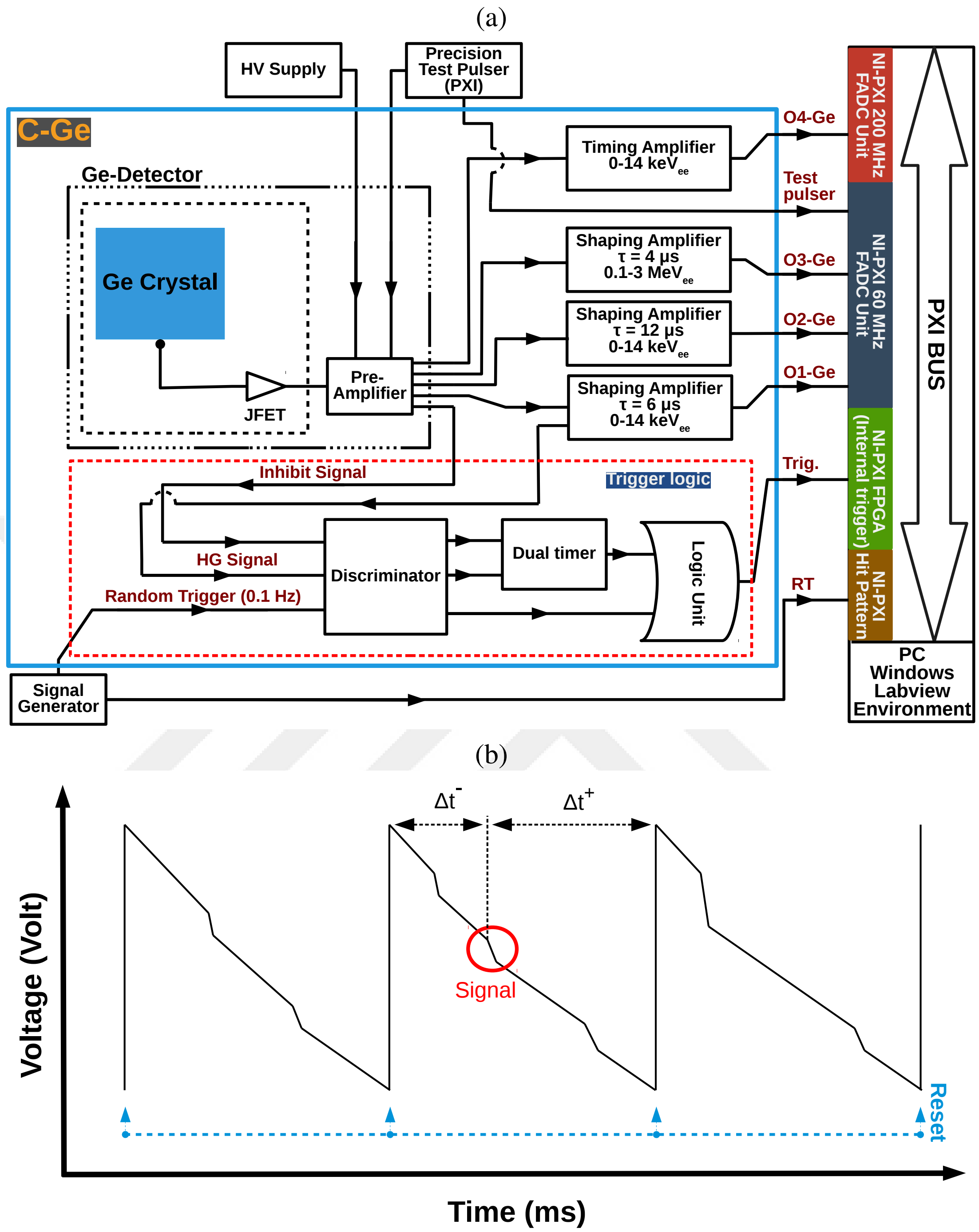

Figure 3.7 (a) The schematic diagram of simple germanium DAQ circuit. (b) Raw signal of Ge detector

to design the trigger signal as shown in Figure 3.7(a). This inhibit signal is prohibited by opening a window in dual timer. Thus, final trigger is controlled by OR logic with combination of signal generator with 0.1 Hz and a germanium signal without reset time. This also causes losing information in inhibit time, which is called as death time. The triggering logic is given in opened form in Figure 3.7(a) while the three outputs

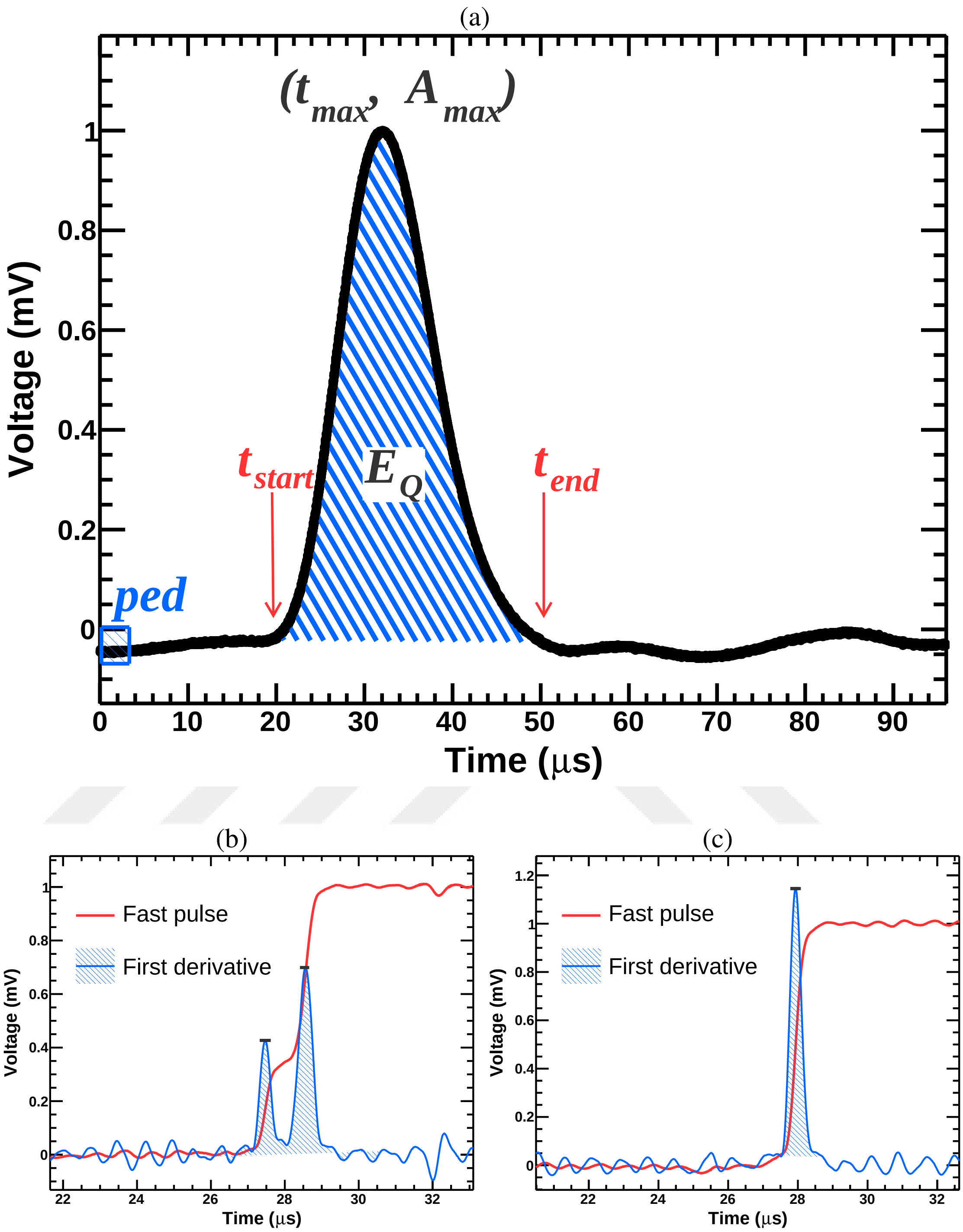

Figure 3.8 (a) The sample pulse as an output of shaping amplifier (SA). The fast pulse samples as an output of timing amplifier (TA) for, (b) multi-site event and (c) single-site event

from shaping amplifier (SA), signal generator and inhibit signal are connected to National Instruments (NI) device – NI SMB-2163. This device is connected to NI 5571R, which is composed of an NI FlexRIO FPGA (Field Programmable Gate Arrays). Thus triggering logic internally is build in digital platform. The open form also illustrates the building trigger in analog way.

The raw signal from the preamplifier is shaped and amplified by using Canberra 2026 shaping amplifier and Canberra 2111 timing amplifier. As illustrated in Figure 3.7(a), output from shaping amplifier as O1-Ge is shaped in Gaussian form by applying high-gain amplify, which is called as High-Gain (HG) channel. Therefore, HG channel has seted the low energy range within the 0-14 keV$_{ee}$. O1-Ge channel also provides the signal output to triggering logic. It is also the main channel that provides the desirable spectrum. O2-Ge channel helps to differentiate noise signal at low energy. O3-Ge channel is Low-Gain (LG) channel with high energy range (0.1-3 MeV$_{ee}$). As a final channel, O4-Ge provides the HG signal from timing amplifier (fast pulse) to differentiate the signals by using their pulse shape which is known as pulse shape discrimination (PSD) method. Examples of the signal forms from both shaping and timing amplifiers are illustrated in Figure 3.8. The parameters illustrated in Figure 3.8(a) help in analyzing the spectrum. Energy information can be obtained by maximum height of pulse (A-mode) or total charge of the pulse (Q-mode) as is given in Figure 3.8(a) by A_{max} and E_Q respectively. There the t$_{max}$ represents the time at maximum height and ped the electronic noise fluctuation known as pedestal. In Figure 3.8(b-c), the fast pulse examples as an output of timing amplifier for both multi-site and single-site events are given. In general, the rising slope has interaction position dependence in pPCGe detector. However, single-site and multi-site events are valid for both nPCGe and pPCGe detectors. Thus, the fast pulse provides the discrimination between these kind of events.

3.3 Complete DAQ Circuit for the KSNL

The advantage of building a DAQ system is being flexible. Thus, any experiment can be designed to reach a scientific goal. Therefore, the technology and the designing of DAQ systems become quite important in nuclear and high energy physics researches.

The operational DAQ at KSNL is built around NI instruments within the PXIe-1065 chassis with an embedded PXI-8108 real-time controller and extended by the flash analog-to-digital converter (FADC) and FPGA units. The complete DAQ circuit is shown in Figure 3.9.

The triggering system is the same as described in Section 3.2.1 and illustrated in Figure 3.7. The logics of plastic scintillators as is shown in Figure 3.3 are provided internally by the FPGA. However, the open form is illustrated in Figure 3.3. The timing starts by the coming signal from the plastic scintillators logic and ends by the system triggering. Thus the time difference between plastic scintillator and germanium detector triggering is recorded as time-to-digital converter (TDC) information.

The signal generator provides square pulse to the system in 0.1 Hz which is called random trigger (RT). This helps to measure zero energy and death time information. When the signal generator is triggered in the system, in general, other detectors stay quiet. Thus the information from the detectors is consistent with zero energy when they are quiet. On the other hand, the death time can measured by

$$\text{death time} = \left(1 - \frac{\text{measured RT}}{\text{generated RT}}\right) \times \tau_{real} \; . \tag{3.2}$$

The typical death time of the system in monitoring level is 12%.

Active shielding system is interested in coincidence and anti-coincidence cases. Plastic scintillator provides the time information and if any channel is consistent with cosmic signal, it is tagged as CR^{+}, otherwise it is tagged by CR^{-}. Typical event rate for each panel is illustrated in Figure 3.10. There are twelve channels related with top panel in the middle and another twelve channels in the left and right for the side panels. Multiple hit in cosmic panels shows that two or more plastic scintillators were fired at the same time. Therefore, it is understandable that most CR^{+} events are significantly correlated with top panels while the side panels are mostly associated with multiple hits by other panels.

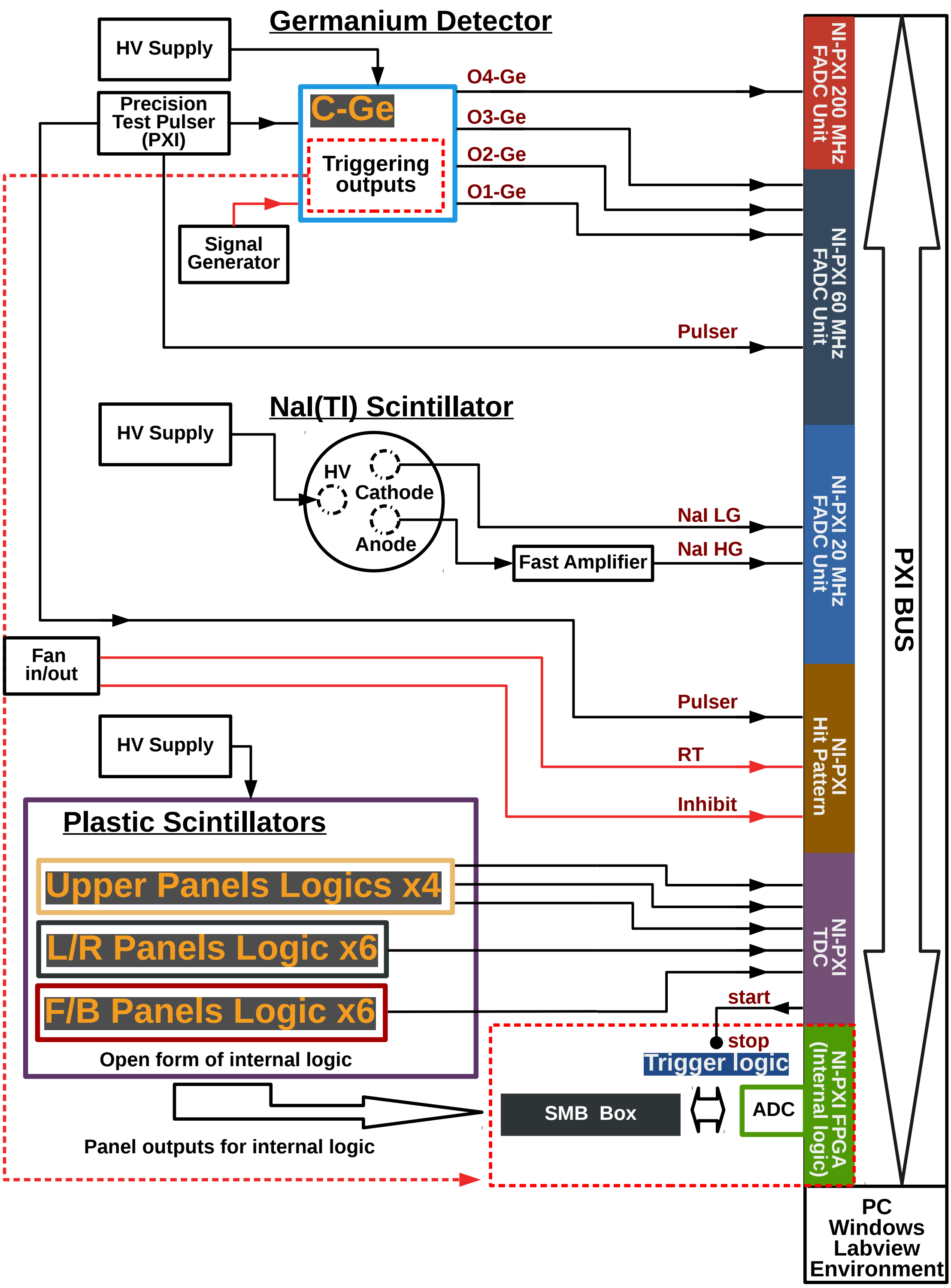

Figure 3.9 The schematic view of DAQ system in the KSNL. Some logics and DAQ circuits previously given is adapted from the Figure 3.3 and 3.7(a)

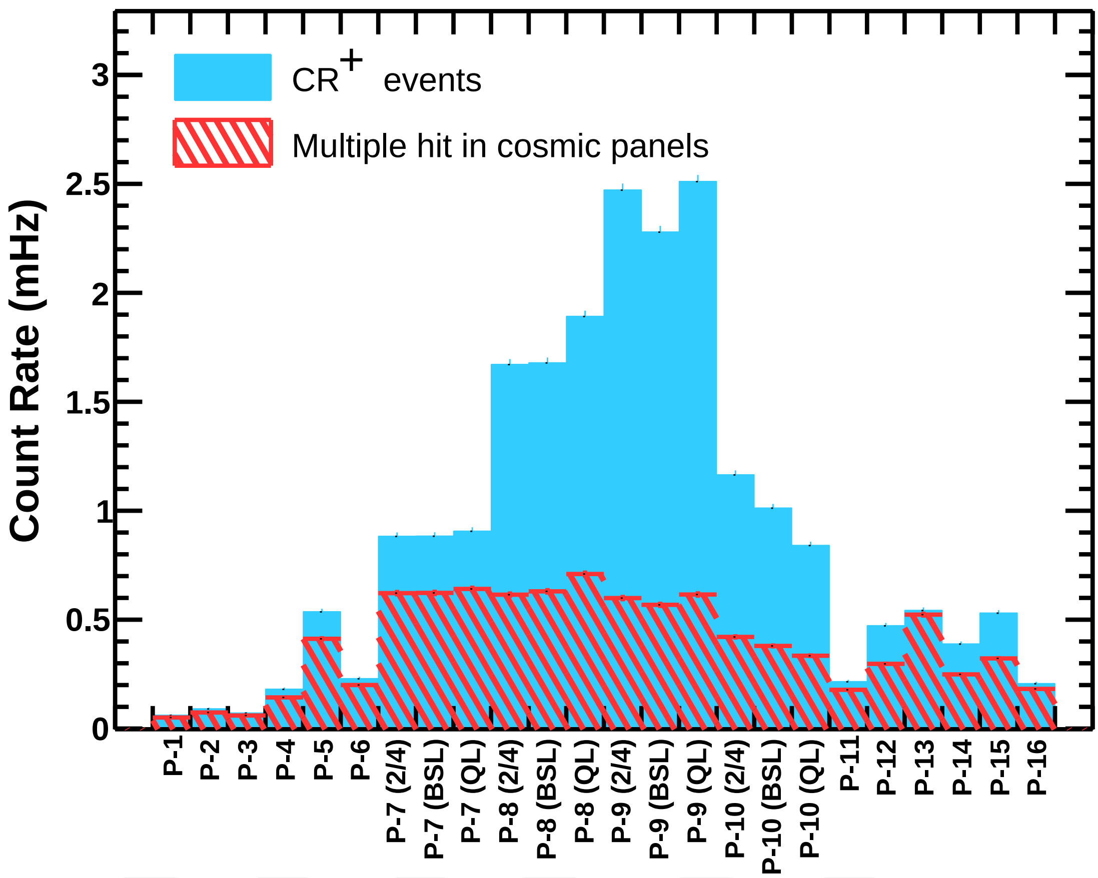

Figure 3.10 Event rate of the cosmic panel in coincidence case with Germanium (CR^+). The x-axis label present the plastic scintillator panel position (P-x) as illustrated in Figure 3.2(a) and the abbreviations in parentheses represent the logic for top panels as described in Section 3.1

Another active shielding system is AC which provides information of coincidence and anti-coincidence cases by NaI(Tl) spectrum. Above the threshold of the NaI(Tl) detector is considered as coincidence case and tagged by AC^+, otherwise AC^-. Thus, there are four spectrum channels by combining CR and AC active shielding system as $CR^\pm \otimes AC^\pm$ where +(-) denotes coincidence (anti-coincidence) of the CR or AC. In particular, $CR^+ \otimes AC^+$ tag selects cosmic induced particle and $CR^+ \otimes AC^-$ tag is correlated specifically with cosmic induced neutrons due to neutron insensitive AC detector. Also $CR^- \otimes AC^+$ tag selects ambient γ-induced background and $CR^- \otimes AC^-$ is associated with neutrino- or WIMP-induced candidate events uncorrelated with both CR and AC systems.

CHAPTER FOUR
CHARACTERIZATION AND PERFORMANCE OF HPGE

In the previous chapter, the DAQ composition and the data processing have been given. The data digitized from DAQ circuit needs to be organized with analyzable parameters for data analysis. Most of the analyzable parameters, except those from the direct information, are collected from digitized waveform as seen in Figure 3.8(a). The information are gathered either directly or indirectly from the waveform and are stored in ROOT-ntuple, which is an object-oriented data analysis framework for experimental particle physics (Brun & Rademakers, 1997). Thus, this framework can be controlled by C++ or python source codes to analyze offline data. Here the desired point to reach by analyzing data is $CR^- \otimes AC^-$ spectrum as being candidate of neutrino or WIMP induced events. Therefore, characterization of HPGe and its calibration are quite significant to reach physical goal with a pure sample of $CR^- \otimes AC^-$. The detector performance in this study is summarized for both nPC and pPC Ge detectors in Table 4.1. More studies for other detectors are given in Reference (Soma, 2016).

4.1 Energy Calibration of HPGe

Two different energy modes can be used as mentioned before in Section 3.2.1. Those are A-mode and Q-mode, which are the maximum height (A_{max}) and the integrated area (E_Q) within the time window [t_{start}, t_{end}] of waveform, as is illustrated in Figure 3.8(a). However, the established results show that as in Table 4.1, the root mean square (RMS) of A-mode (σ_A) is better than Q-mode RMS (σ_Q). Therefore, studies with A-mode provide better energy resolution and threshold.

Test-pulser events are produced by a precision pulse generator (NI PXI 5412) as was shown in C-Ge DAQ circuit in the previous chapter. Pulser events can be used in studies for testing detector energy response. The calibration of A_{max} into energy unit can be converted by polynomial function of linear behavior. However, deviation

Table 4.1 Summary table of performance parameters of nPC and pPC Ge detectors in this study. (Table is adapted from (Soma, 2016))

Performance Parameters	pPCGe	nPCGe	Uncertainties (%)
Modular Mass (g)	500	500	–
RESET Amplitude (V)	6.8	6.8	–
RESET Time Interval (ms)	~ 160	~ 170	–
Pedestal Noise			
Pedestal Profile RMS σ_A (eV$_{ee}$)	41	49	2.6
Area RMS σ_Q (eV$_{ee}$)	58	52	3.1
Pulser Width			
FWHM (eV$_{ee}$)	110	122	1.5
RMS (eV$_{ee}$)	47	52	1.5
X-Ray Line Width			
RMS (eV$_{ee}$)	87	104	3.4
Electronic Noise-Edge for Raw Spectra (eV$_{ee}$)	228	285	1.8

from linearity for A-mode can be expected when the pulse height is comparable with pedestal noise fluctuation. Calibration of such a small energy may not be practicable by radioactive sources. Therefore, using the test pulser for energy estimation is the ideal way for characterizing the linearity of energy. The energy estimation by using test pulser for both pPC and nPC Ge detectors is illustrated in Figure 4.1(a). As is seen in the figure, non-linear behavior appears below $\sim 6\sigma_A$, which is less than the noise edge of 7.3(7.6)σ_A for pPCGe(nPCGe). On the other hand, energy resolution of pulser events is a characterizing parameter for the contribution of electronic systems. It deteriorates below $2\sigma_A$ as is seen in Figure 4.1(b), which is also below the noise edge. Thus, the non-linearity effect or the electronic systems contribution to the energy resolution is ineffective above the noise edge and physical region of interest. However, the non-linearity effect is valid for zero energy in A-mode.

The n$^+$ surface of the pPCGe is fabricated by lithium diffusion and has a typical

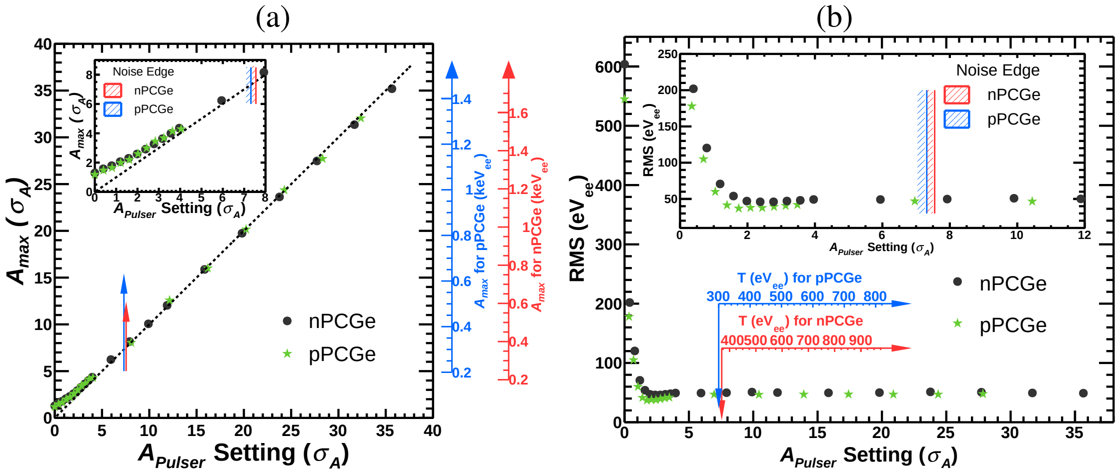

Figure 4.1 Test pulser response of nPC and pPC Ge detectors,(a) energy estimator A_{max} (b) RMS resolution

Table 4.2 The list of different radioisotopes

Parent Radioisotope	Daughter Nuclei	Daughter K-shell Energy (keV)	Daughter L-shell Energy (keV)	Parent Half-life
^{73,74}As	Ge	11.103	1.142	80.3, 77.8 days
^{68,71}Ge	Ga	10.367	1.298	271, 11.4 days
^{68}Ga	Zn	9.659	1.197	67.7 min
^{65}Zn	Cu	8.979	1.096	243.7 days
^{55}Fe	Mn	6.539	0.769	2.74 years
^{49}V	Ti	4.966	0.564	330 days

thickness of ∼1 mm, which suppresses external γs with energy less than 50 keV. Also the nPCGe detector does not have a thick entrance window and is housed in a copper cryostat of 1 mm thickness. Therefore, for both detectors the energy calibration in KSNL is provided internally by some long-lived cosmogenically activated isotopes as is listed in Table 4.2.

The calibrated typical spectra for the denoted X-ray lines in Table 4.2 and the noise edge correlation are shown in Figure 4.2 for both nPC and pPC Ge detectors in the KSNL.

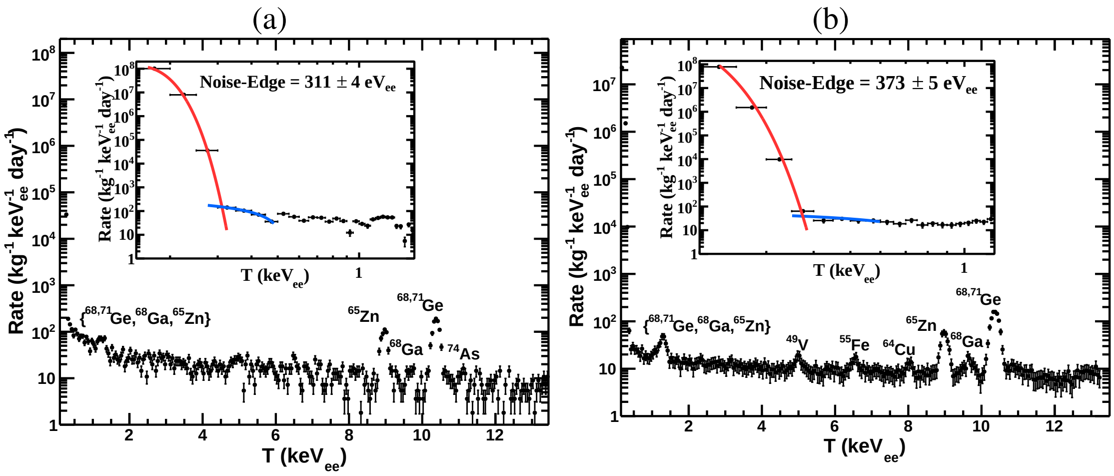

Figure 4.2 Typical spectra showing X-ray lines as denoted in Table 4.2 for (a) pPCGe and (b) nPCGe detector

4.1.1 Quenching Effect

As long as the nuclear recoil is concerned, the linearity of energy of the target material must be discussed as well. Commonly, the relationship between nuclear recoil energy and linear ionization energy is given as ratio by a factor, which is called quenching factor (QF). Knowledge of QF is essential for CENNS, WIMP, neutron scattering and so on, the signatures of which are due to nuclear recoils. This subject was studied first for germanium detectors by Lindhard et al. (1963). Then many groups have worked on the quenching factor for germanium detector as is depicted in Figure 4.3.

The result obtained by Transport of Ions in Matter (TRIM) software is (Ziegler, 1998) in a good agreement with existing data (Jones & Kraner, 1971,7; Messous et al., 1995; Shutt et al., 1992). Therefore, in this thesis work, the quenching effects on germanium recoil (Ge-recoil) are considered by TRIM software and, in general, energy is given under the tag of electron equivalent (eV$_{ee}$) unit.

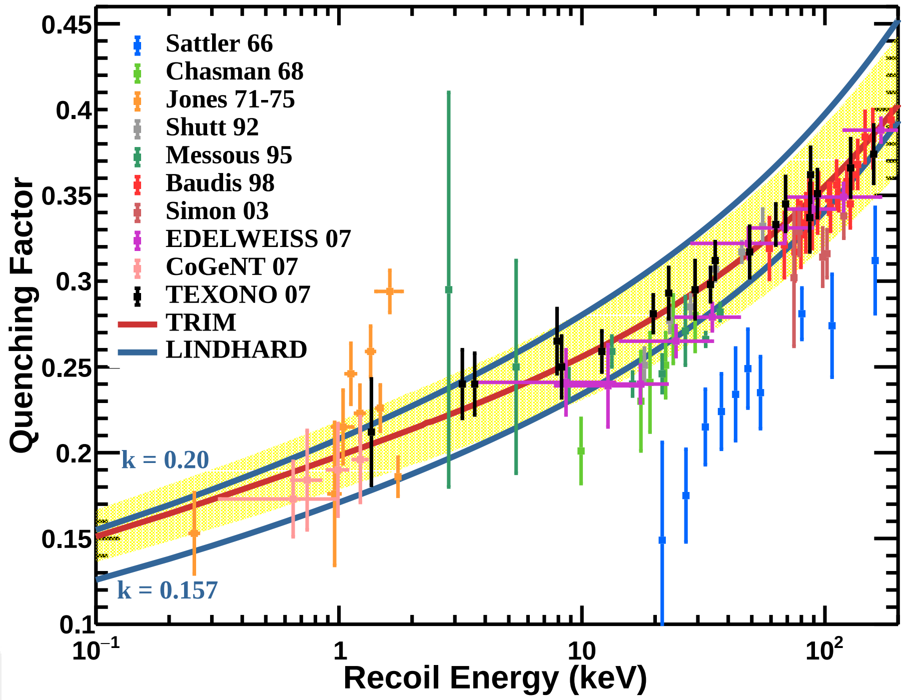

Figure 4.3 Quenching factor measurement on germanium by various groups with calculation from TRIM software and Lindhard model

4.2 Event Selection Rules

The events selection criteria are based on the basic filtering and the labeling of active shielding to separate the noise and uncorrelated events from physical signal and putting them in the correct channel. Therefore, the event selection analysis and understanding of each channel as well as controlling the efficiencies are quite important to avoid leakage among the channels. In addition, for the pPCGe detector, the PSD technique is valid to differentiate surface and bulk events due to events deformation of inactive n^+ surface on pPCGe. This layer acts like a barrier for internal radiation and the energy information is lost. Therefore, the technique is used to enhance the background at low energy region in nPCGe.

The basic filtering of the data as well as its efficiency are illustrated in Figure 4.4. In general, the basic filtering is provided by projection of A_{max} into another parameters (E_Q, ped and t_{max}), which are shown in Figure 3.8(a). Thus, the behavior of each parameter is observed on energy dependence and unphysical signals coming from elec-

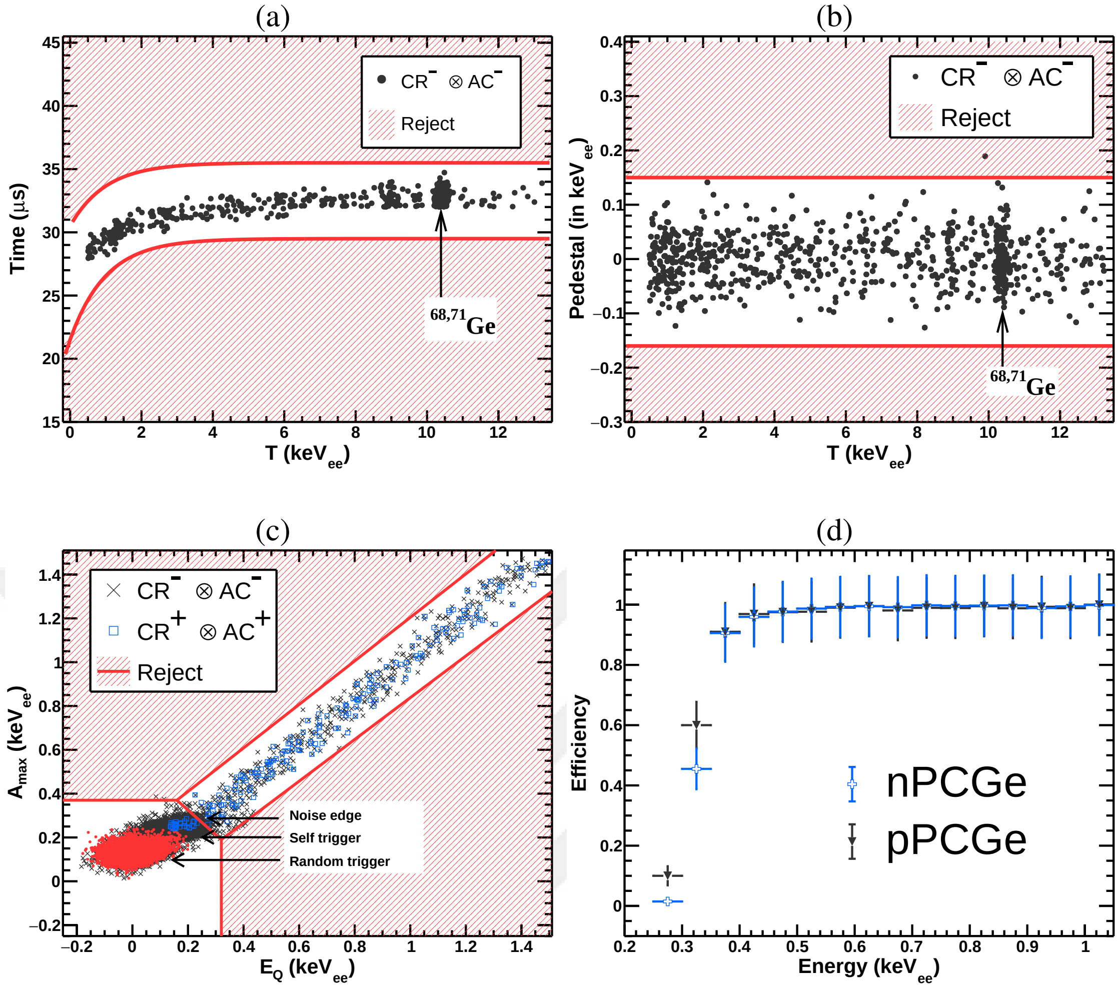

Figure 4.4 (a) The correlation among the A_{max} and t_{max}. (b) The pedestal distribution in different energies. (c) The projection of A_{max} into E_Q in energy unit. The association provides the precise noise edge selection. Self trigger and random trigger events are also shown. All the figure provides the information of basic filtering by removing out events in rejection areas and (d) the efficiency of basic filtering

tronics are rejected.

As is clearly seen in Figure 4.4(c), $CR^+ \otimes AC^+$ events are mostly physics-induced, therefore it is one of the best possible ways to distinguish the self-trigger pulse from physics-induced pulse. So, the fraction of $CR^+ \otimes AC^+$ events provides the efficiency of basic filtering as is illustrated in Figure 4.4(d). As a consequence, the efficiency of basic filtering for physics related signals is $<$99%.

4.2.1 *Active Shielding Labeling*

As was mentioned in the previous chapter, there are two active shielding systems, denoted as CR and AC. The CR system is based on the time difference among the germanium and the AC system is distinguished by NaI(Tl) signal. The selection band of CR^{+} and AC^{-} is illustrated in Figure 4.5. The cosmic coincidence events are accumulated in a specific region as is seen in Figure 4.5(a). The bending effect depends on the shaping time difference between plastic scintillators (10 ns) and germanium signals (6 μs). Besides that, anti-coincidence selection of AC system is the threshold of the NaI(Tl) detector and so the events are not physical signals of anti-compton detector as is illustrated in Figure 4.5(b).

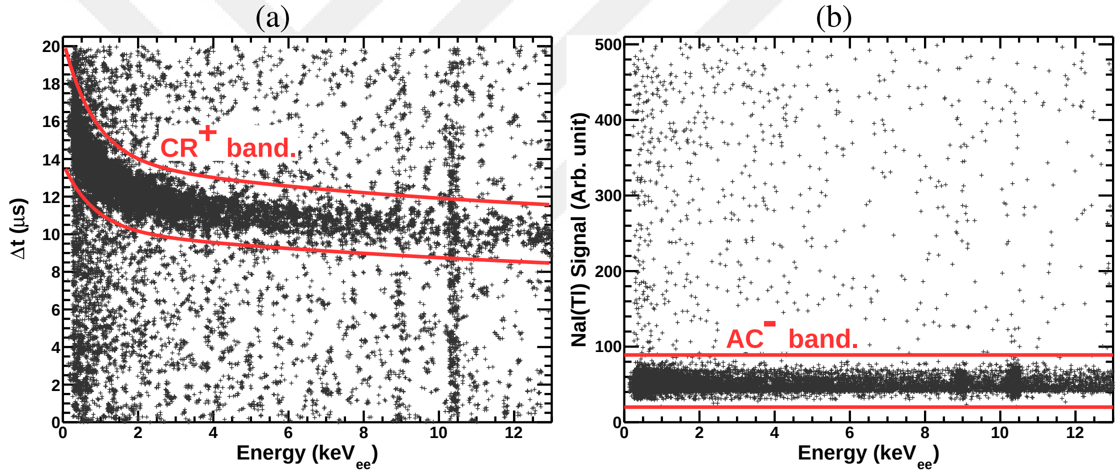

Figure 4.5 The projection of germanium signal into (a) CR signal and (b) AC signal

Besides separating active shielding systems into different channels, the efficiency of each channel must be understood. For instance, in Figure 4.5(a), the ^{68,71}Ge line emerged clearly in CR^{-} part as well as in CR^{+} band. But the main task of the CR system is to differentiate cosmic and cosmic-induced signals. However, the line of ^{68,71}Ge isotope occurs internally and is not related to cosmic-ray signals. Therefore, this is a strong sign of leakage among the CR coincidence and anti-coincidence channels. On the other hand, this internal line appears in AC^{-} system where it belongs genuinely and does not emerge in the part of AC^{+}. This may sign that the efficiency of AC detection is sufficient yet it should be investigated and determined properly.

The random trigger events are uncorrelated with CR and AC system selections. Therefore, the coincidence is not expected among the random trigger and other selection channels, which is an ideal condition to investigate efficiency. According to random trigger coincidence, the anti-concidence of AC system is inefficient by $\sim$0.5 % and the CR system by $\sim$8 %. On the other hand, the efficiency of CR detection can be measured by NaI(Tl) detector. At the higher energy of NaI(Tl) spectra, cosmic muon signals emerge without any contamination by other background signals. Thus, the coincidence of CR signals with the region of cosmic muon signal on NaI(Tl) detector provides the detection efficiency of CR signal, which is measured as $\sim$93 %. As a consequence, the leakage among the CR coincidence and anti-coincidence channels exists as expected and should be taken into account for the desired spectra.

4.2.2 The Pulse Shape Discrimination Method

The surface of pPCGe detector consists of Li-difused n^+ surface which is insensitive to radiation and is known as the dead layer. It is also a passive barrier against low energy radiation. The region immediately below this dead layer with weak electric fields is known as transition layer, where the slow pulse arises due to poor charge collection as was (and is) evidently shown in the past and currently (Aalseth et al., 2011; Sakai, 1971; Strauss & Larsen, 1967). Therefore, the energy information is lost in this region and needs to be differentiated of surface events.

The events for PSD method can be gathered by timing amplifier as is illustrated for various type of pulses in Figure 4.6. The TA-pulses are firstly smoothed by the Savitzky-Golay filter to be successfully fitted, which measures the slope of the rising part as follows

$$0.5A_0 \tanh[(t-t_0)s_0] + P_0 \ , \tag{4.1}$$

where A_0 and P_0 are respectively the amplitude and the pedestal offset. t_0 is the timing offset and s_0 is the slope which provides the characterization of TA-pulse by

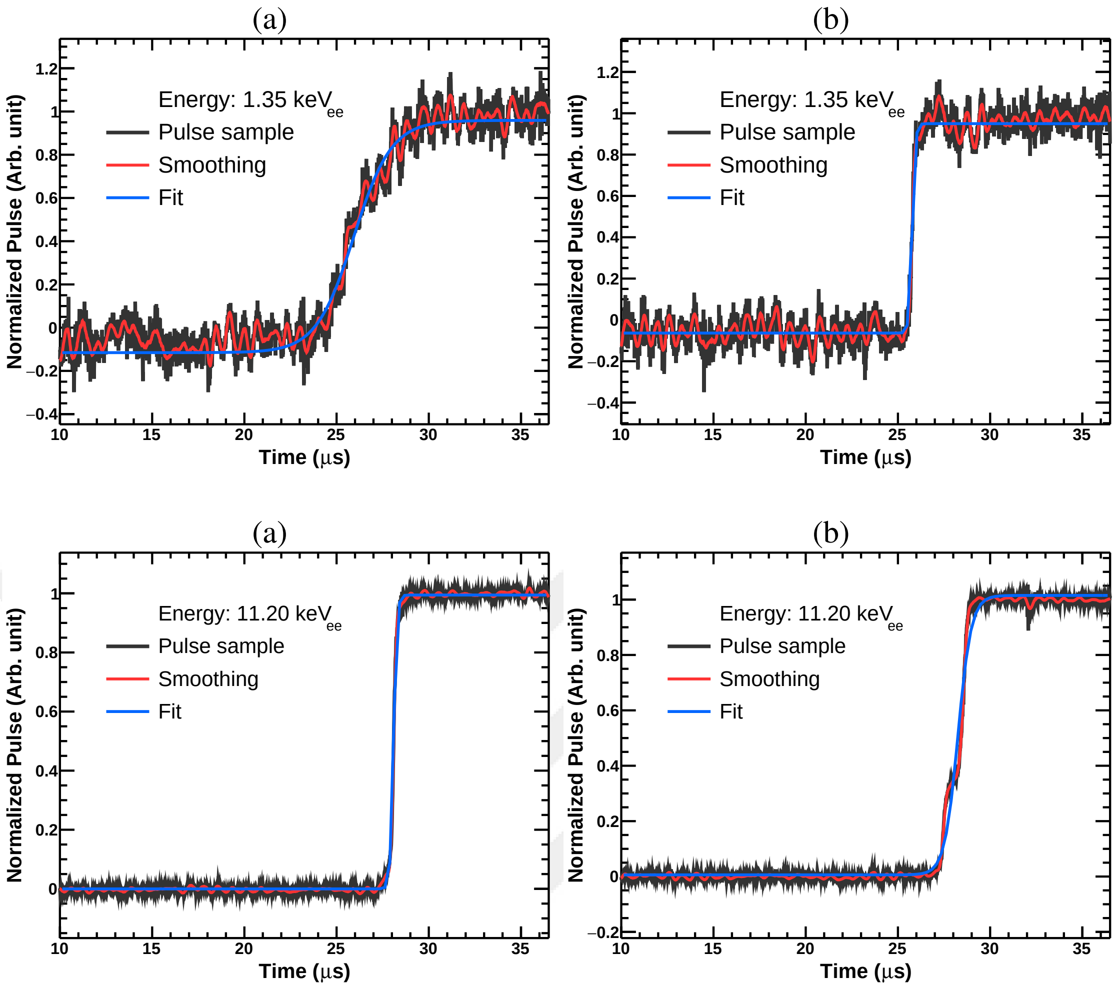

Figure 4.6 The pulse sample by taken with timing amplifier for various types, (a) surface, (b) bulk, (c) single-site and (d) multi-site events

$\tau = log(19)/s_0$. Therefore, the discrimination of pulse type by rising part slope as is illustrated in Figure 4.6(a) slow rising pulse as surface event – (b) fast rising pulse as bulk event, can be recognized by the parameter τ as is shown in Figure 4.7.

The single and multiple site events are valid for both detectors and as illustrated in Figure 4.6(d), the rising part of multi-site events behaves slower and this attitude causes them to discriminate among surface and bulk events in τ space, as is shown in Figure 4.7(a). For the nPCGe detector, the surface events do not occur, therefore multi-site events accumulate above the single-site events as is seen in Figure 4.7(b). As a consequence, the surface events must be rejected on nPCGe, however, at the low

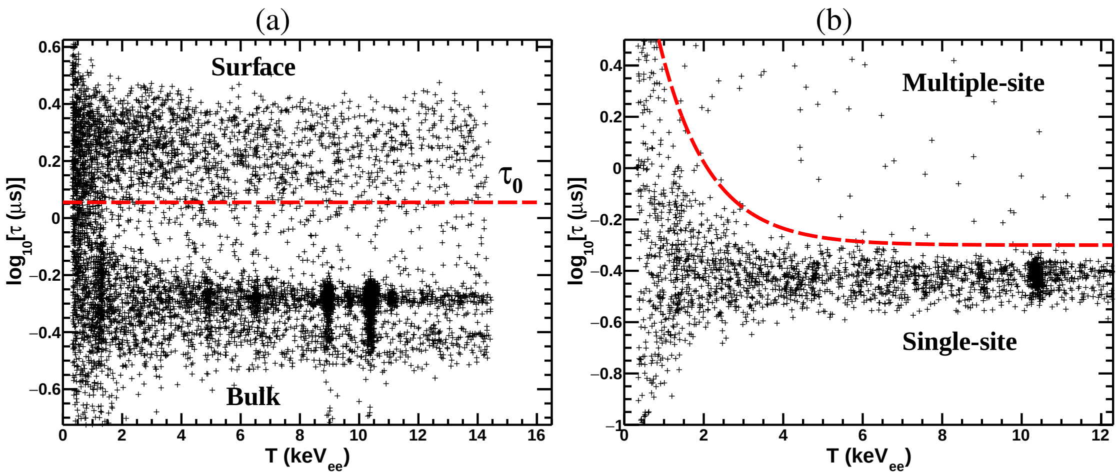

Figure 4.7 The projection of germanium signal into τ, (a) pPCGe and (b) nPCGe detector

energy due to the mixing of events, the discrimination of bulk and surface events is poor. Therefore, differentiating them at low energy should involve some statistical methods.

4.3 Efficiency Correction

The efficiency of selection criteria is not always close to 99%. Therefore, the correction is necessary for some selections. This correction can be achieved via statistical method by adding and subtracting among the channels, where the leakage and contamination occurs. In general, cosmic ray efficiency is ∼93 %, therefore all the experiment in KSNL needs correction for cosmic-ray leakage for all kind of detectors, like germanium detector and neutron detector as well. On the other hand, specifically, the pPCGe detector needs surface-bulk discrimination correction at the low energy as was mentioned in the above section.

4.3.1 CR Correction

The CR^+ leakage due to detection efficiency (∼93 %) and the CR^- leakage due to rejection efficiency as (∼92 %) are represented by λ and ε respectively. The very simple approach is used to define statistical background correction as follows

$$CR_R^{\pm} = CR_M^{\pm} - CR_L^{\mp} + CR_L^{\pm} \ , \tag{4.2}$$

where $\mathrm{CR}_M^{\pm}$ stand for the measured number of events, and $\mathrm{CR}_L^{\mp}(\mathrm{CR}_L^{\pm})$ is the number of events that leak into $\mathrm{CR}^{\pm}(\mathrm{CR}^{\mp})$ set as a result of the detection and rejection inefficiencies given as

$$\begin{aligned} CR_L^{+} &= (1-\varepsilon)CR_R^{+} \\ CR_L^{-} &= (1-\lambda)CR_R^{-} \ . \end{aligned} \tag{4.3}$$

Solving the coupled Equation 4.2 with given parameters in Equation 4.3 provides the statistical background correction model as real spectrum $\mathrm{CR}_R^{\pm}$ by

$$\begin{aligned} CR_R^{+} &= \frac{\varepsilon \times CR_M^{+} - (1-\varepsilon) \times CR_M^{-}}{\varepsilon + \lambda - 1} \\ CR_R^{-} &= \frac{\lambda \times CR_M^{-} - (1-\lambda) \times CR_M^{+}}{\varepsilon + \lambda - 1} \ . \end{aligned} \tag{4.4}$$

4.3.2 Surface/Bulk Correction

As was mentioned in Section 4.2.2, the characterization parameter τ was used for bulk surface identification and in the τ-space event mixing at low energy was illustrated in Figure 4.7(a). The bulk-signal retaining (ε_{BS}) and surface-background suppressing (λ_{BS}) efficiencies have to be calibrated as related factors between measured and real rates, denoted by (B_M, S_M) and (B_R, S_R) respectively, which are related by the following coupled equations (Li et al., 2014)

$$\begin{aligned} B_M &= \varepsilon_{BS} \times B_R + (1-\lambda_{BS}) \times S_R \\ S_M &= (1-\varepsilon_{BS}) \times B_R + \lambda_{BS} \times S_R \ . \end{aligned} \tag{4.5}$$

The three independent data samples were used on calibration of ε_{BS} and λ_{BS} such as ^{241}Am, ^{137}Cs and the CR^{+} $\otimes$ AC^{-} data as cosmic neutron reach background. The gamma sources of ^{241}Am and ^{137}Cs provide the surface-rich data sample while the cosmic neutrons provide bulk-rich background as measurement. The comparison of measurement and real rates is provided by simulation of gamma sources and cosmic neutron measurements from nPCGe are considered as real rates which has no anomalous surface effects.

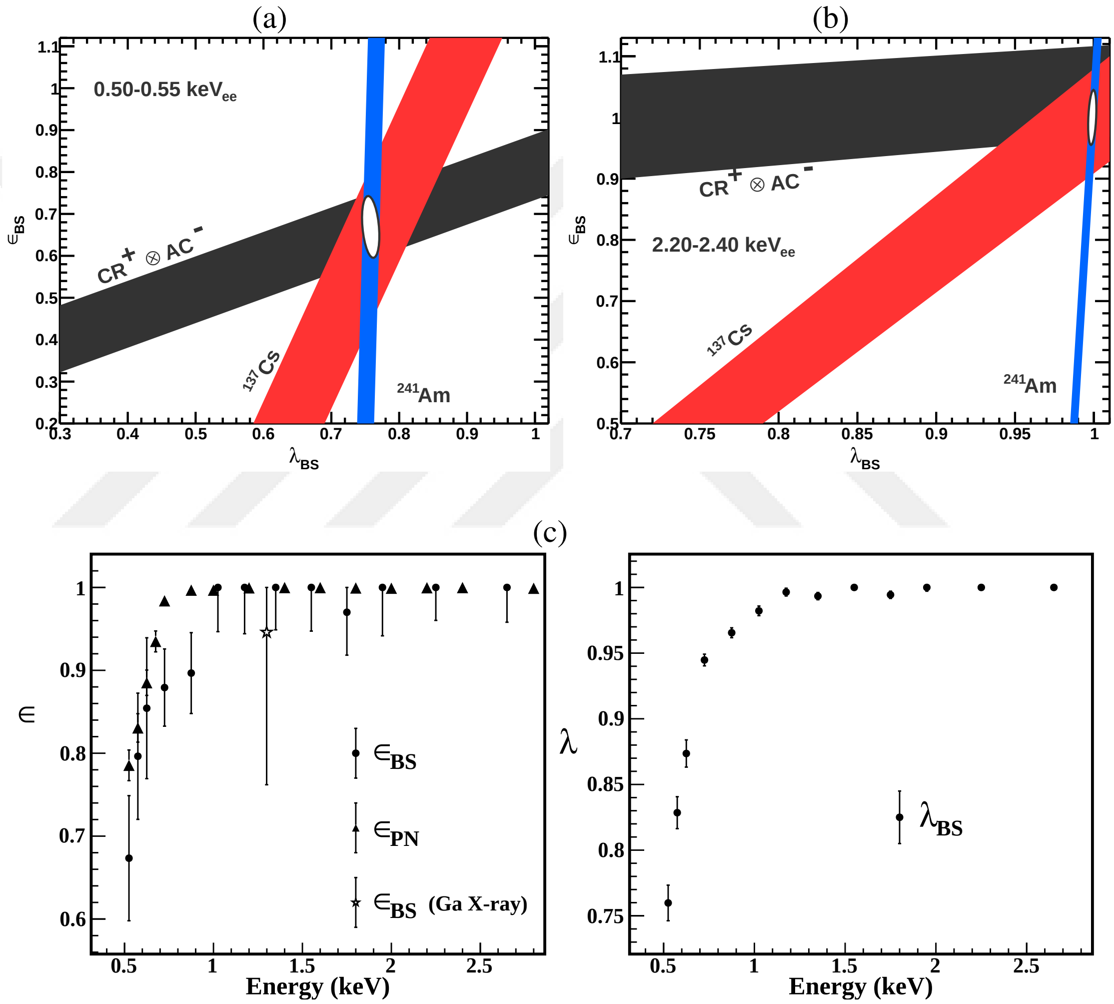

Figure 4.8 The allowed region of ε_{BS} and λ_{BS} derived by solving the coupled equations of 4.5 on the calibration data set at (a) 0.5–0.7 keV$_{ee}$ and (b) an energy bin at 2.2 keV$_{ee}$. (c) The measured ε_{BS} and λ_{BS} as function of energy with independent measurements on bulk/surface with Ga L-shell X-rays

By using the above-mentioned calibration data, ε_{BS} and λ_{BS} are derived by solving the coupled Equation 4.5 taking into account $B_M + S_M = B_R + S_R$. The solution on different energies provides the three allowed regions and merging point determines the efficiencies which is illustrated in Figure 4.8. Thus, physics samples can be obtained for measured ε_{BS} and λ_{BS} parameters by the following equation

$$\begin{aligned} B_R &= \frac{\lambda_{BS} \times B_M - (1-\lambda_{BS}) \times S_M}{\varepsilon_{BS} + \lambda_{BS} - 1} \\ S_R &= \frac{\varepsilon_{BS} \times S_M - (1-\varepsilon_{BS}) \times B_M}{\varepsilon_{BS} + \lambda_{BS} - 1} \ . \end{aligned} \tag{4.6}$$

4.4 Germanium Spectrum for the Neutrino and WIMP Candidate Signals

In this chapter, p- and n-type point-contact high-purity germanium detectors having 500 g mass are analyzed and their selection criteria are presented according to KSNL experiment requirements. After all, processes are applied as was mentioned above; the neutrino and WIMP candidate spectra are illustrated in Figure 4.9 for both pPC and nPC Ge detectors with their selection criteria and correction steps as well. As a consequence, it is understood that p-type PCGe detector has slightly better energy resolution as compared to that of n-type. However, due to active n^+ surface, the pPCGe detectors provide some characteristic pulse shape for surface events which mix together with bulk events at lower energy. Therefore, below 2 keV$_{ee}$ of the spectrum, some statistical methods are desired to differentiate bulk and surface events intensity. This is the important subject for low energy achievement on p-type PCGe detectors.

The background levels of both nPCGe and pPCGe detectors have similar behaviors. The excess is observed below 2 keV$_{ee}$ of spectra from both detectors. Besides that, the spectrum shape is flat as being typical background for Compton scattering of γ-ray events. Therefore, the region above 2 keV$_{ee}$ has events dominantly from photon background from γ-ray events and the characteristic X-ray emission lines from some cosmogenicly activated long-lived isotopes. It is known that neutron events come out at low energy on the germanium detector due to poor energy deposition by the recoil of high Z number nuclei and quenching effects. Therefore, the neutron background must be understood on germanium detectors spectra, especially below 2 keV$_{ee}$.

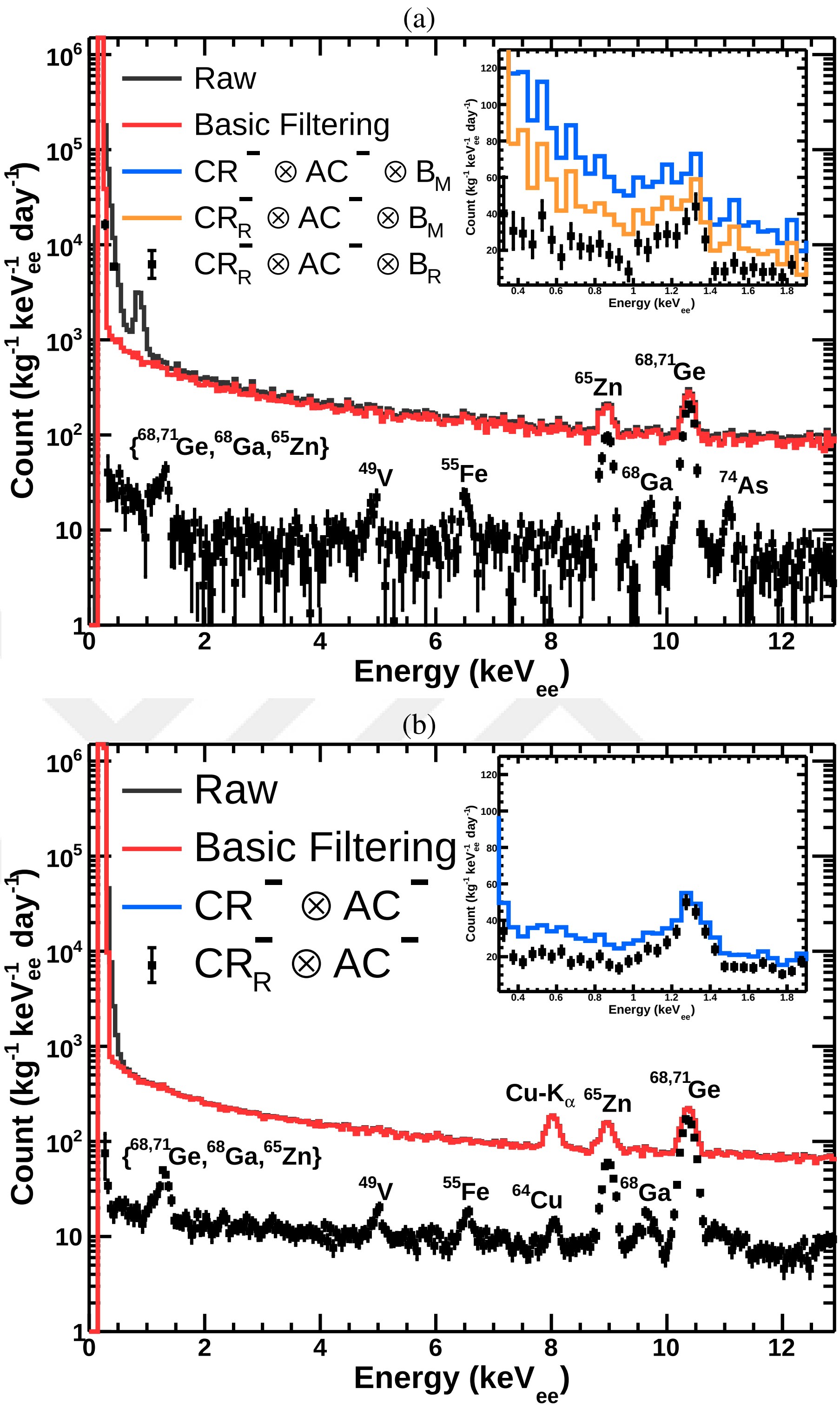

Figure 4.9 The final germanium results after various selection for (a) pPCGe and (b) nPCGe detectors. The correction effect on the spectrum is shown in inset figures

Recently, germanium detectors with sub-keV sensitives are popular on investigation of SM and exotic neutrino interactions as well as for searches of light WIMP.

The germanium detectors are also important for the neutrinoless double beta decay experiments, which desire low background and high energy resolution. Therefore, characterization of germanium detector is quite important. The development of germanium detector having high energy resolution and low threshold is still ongoing. These properties are essential for many groups and the innovative investigations will be successful. A new development demonstrates that operating the germanium crystal at cryogenic temperatures has successful achievements on low energy threshold (Agnese et al., 2016). Thus, the studies on CENNS can be successful according to new developments, which desire low threshold as was mention in Section 2.2.3.

CHAPTER FIVE
NEUTRON DETECTION

The neutron detection is a key topic on nuclear and fundamental researches since the appearance of neutron. However, this neutral particle weakly interacts by electric and magnetic field while going among the atoms, and the cross section is only limited by the nuclear forces which have quite short distance, thus it can go inside the materials and take long distance among them. Therefore, detection of neutron has some challenges. On the other hand, by the time, the cross section of neutron with the materials is well understood. Therefore, this creates an opportunity to use Monte Carlo simulation advantage in detection of neutron.

The scintillation can be used for fast neutron detection by the conversion of ionizing particle kinetic energy to observable light. But the light output would be the nuclear recoil energy quenched by some factor for relevant recoil. One of the most common materials for fast neutron detection is the hydrogen atom because of its high cross section. Energy dependence is well known for hydrogen and neutron can transfer entire energy with n-p scattering, unlike heavier nuclei. For thermal neutrons, the most popular reaction is neutron capture of Lithium $^6Li(n,\alpha)^3H$. In this reaction, the αs cause scintillation as observable light in the scintillator material, which means that the incident neutron energy can not be observed. Despite of this, thermal neutrons are a consequence of Maxwell-Boltzman distribution and their spectrum can be calculated by counting from the scintillation. On the other hand, fast neutron spectrum can be build from known nuclear recoil spectra for the monochromatic incident neutrons by some numerical method.

5.1 Design and Features of Hybrid Neutron Detector

The neutron detector designed in this study has a hybrid structure by bringing together two different types of target materials to operate at the same time. The fast

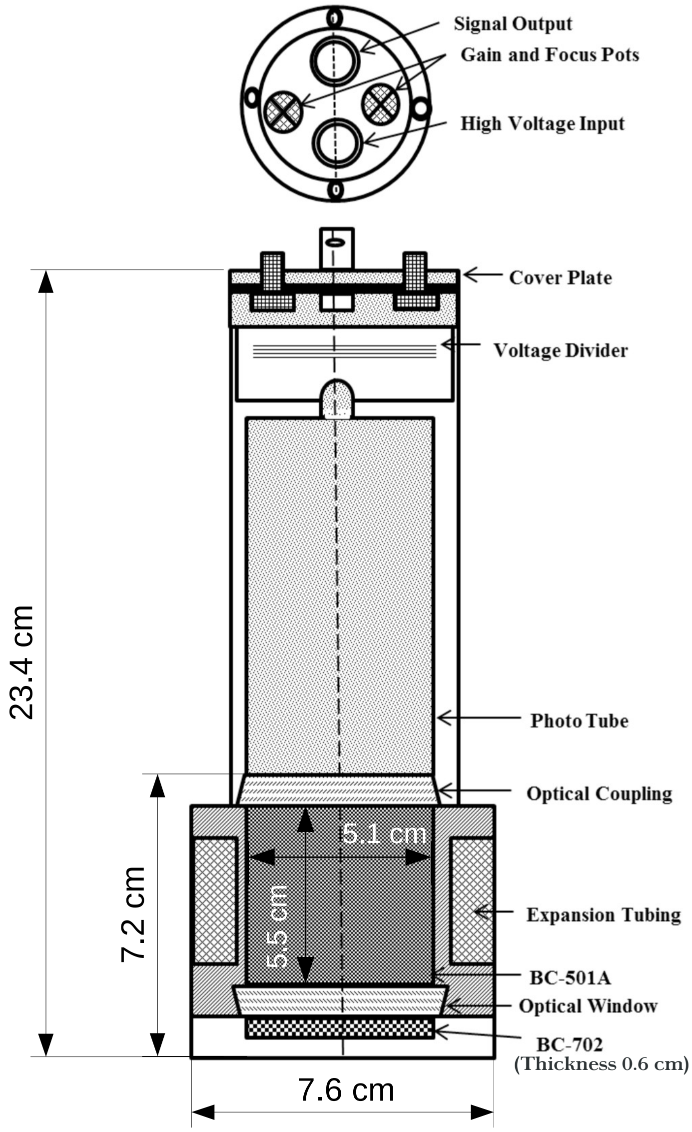

Figure 5.1 The schematic view of the HND

neutron sensitive BC-501A type liquid scintillator having 0.113 liter cell volume and the BC-702 type phosphor powder ZnS(Ag) scintillator having 11 mg of 95 % enriched ^{6}Li per cm^{3} are contructed as HND (Sain Gobain $\sim$ Liquid Scintillators, 2018; Sain Gobain $\sim$ Thermal Neutron Detector, 2018). A 5.1 cm diameter Hamamatsu photomultiplier tube (PMT) has been used for readout of light output from both scintillators. The schematic diagram of HND is depicted in Figure 5.1. The selected target materials provide different signal characteristics for nuclear and electron recoils. Therefore, different pulse shape generations of the detector due to different particles create an opportunity to identify events by PSD. This HND provides excellent discrimination against γ background (Adams, 1978; Kalyna et al., 1970; Sabbah et al., 1968). There are large number of studies for the PSD technique on event identification (Flaska, 2007; Swiderski, 2011).

The selected detector dimension is similar to HPGe detectors used in the KSNL. Thus, detector can be installed in place of HPGe detectors to measure neutron background *in situ*. However, for the characterization of HND and calibrating PSD technique to event identification require known neutron sources. For some safety reasons and to avoid the radioactive contamination during the characterization, the performance of HND has been measured outside the KSNL, in the Academia Sinica, where the offline data is stored.

The BC-501A fast neutron sensitive detector responses to the light output (LO) from the scintillation due to nuclear or electron recoil. Thus, the LO is associated with energy of recoiled particle depending on incoming particle. Therefore, obtaining the neutron energy from the LO requires building from each monochromatic neutron LO response. Namely, if each monochromatic LO is known, the neutron energy spectrum can be reconstructed by some numerical methods. The cheapest way to know LO responses monochromatically is the Monte Carlo simulation. However, the simulation must be matched with experimental result as well. Therefore, the compassion among the simulation and experimental data is essential for the characterization of HND. The Monte Carlo simulation in this study is developed by Geant4 tool (Agostinelli, 2003; Sonay, 2017).

5.1.1 Physical Interactions

As an organic scintillator, the BC-501A contains 4.82×10^{22} and 3.98×10^{22} atoms of hydrogen and carbon per cm^3, respectively. Its high density of hydrogen and carbon atoms makes it a good target material against fast neutrons (1-20 MeV) via the following reactions

$$\begin{aligned} p(n,n)p, \\ {}^{12}C(n,n)^{12}C, \\ {}^{12}C(n,\alpha)^{9}C, \\ {}^{12}C(n,n+3\alpha)\ . \end{aligned} \tag{5.1}$$

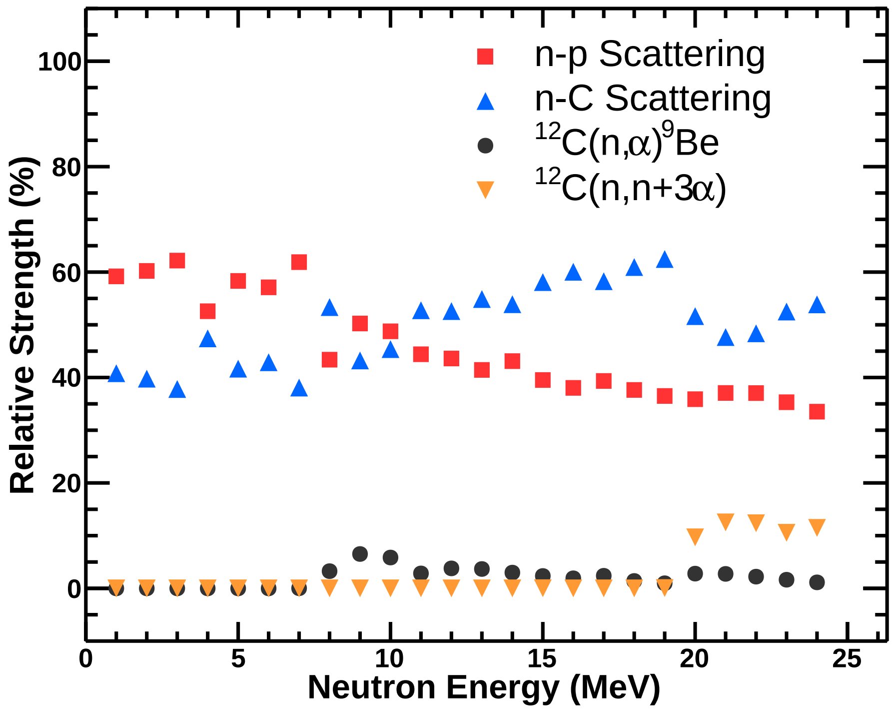

Figure 5.2 The Geant4 simulation of the proportional interaction ratio against neutron energy in BC-501A

The Monte Carlo simulation via Geant4 tool is depicted in Figure 5.2 and the proportions of the reactions are listed in Equation 5.1. As illustrated, the most dominant interactions are elastic scattering of neutron with proton and carbon. Other inelastic scatterings have small proportion and higher threshold of neutron energy. Besides that, regular neutron energy range is usually below 10 MeV in underground laboratories (Tomasello et al., 2008). Therefore, the elastic interactions have significant contribution to the LO and inelastic scattering can stay negligible in this study. On the other hand, the recoil energy by elastic scattering of neutron with carbon atoms will be less than proton recoil energy. The results in this study suggest that the carbon recoil does not give observable signal and the only important interaction is proton recoil.

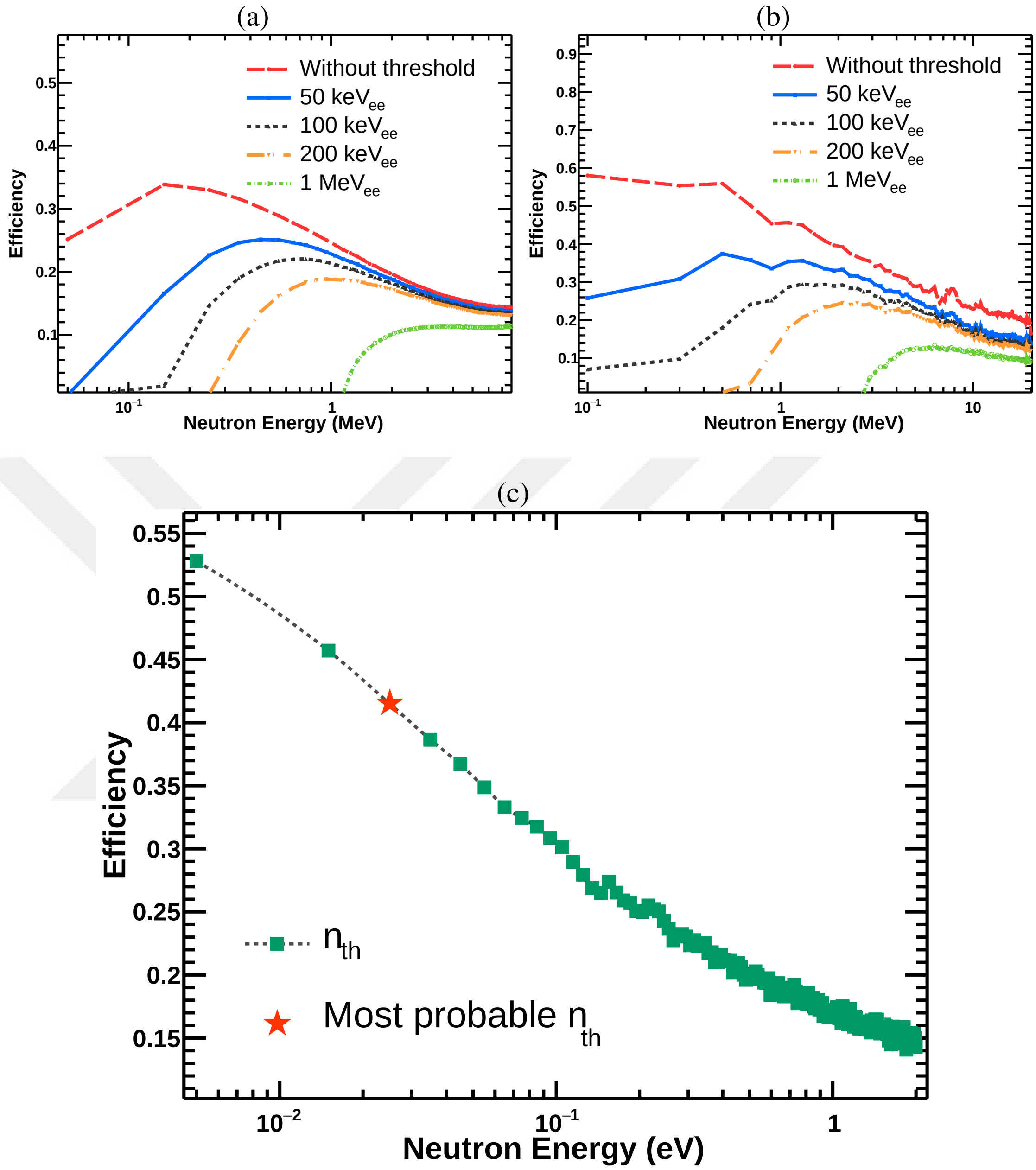

Figure 5.3 Simulated efficiency of BC-501A with respect to (a) incident γ energy and (b) incident neutron energy with threshold effects. (c) Simulated thermal neutron efficiency showed with most probable thermal neutron for BC-702

BC-702 detector is designed as a disc with 50.8 mm diameter and 6.35 mm thickness. The ^{6}Li atoms have high capturing cross section with thermal neutrons which is desirable for good efficiency of the detection. But the LO from the detector is not the recoil energy of the target as usual, indirectively, the α particles as output of the reaction provide the scintillation in ZnS(Ag) via the following reaction

$$^{6}Li + n \rightarrow {}^{3}H\ (2.05\ \text{MeV}) + \alpha\ (2.73\ \text{MeV})\ . \tag{5.2}$$

Therefore, the signal from the reaction does not provide the neutron energy in anyway. However, the discrimination strength of BC-702 for thermal neutrons is very good against the γs and neutrons and the count rate information can be converted to differential cross section by using Maxwell-Boltzmann equation.

The detection efficiency of different particles on HND can be also provided by Geant4 simulation as is illustrated in Figure 5.3. The different threshold effects are demonstrated in Figure 5.3(a-b) for BC-501A γ and neutron efficiency, respectively. Only the proton recoil has been taken into account in the simulation of BC-501A. The neutron capture and detection efficiency is simulated for BC-702 and is shown in Figure 5.3(c) with most probable thermal neutron at 0.025 keV.

5.1.2 Light Output and Quenching Effect

The LO of BC-501A can be produced by electron recoil due to scattering of e^- and γ particles. The light yield of the electron recoil is linear nearly above 100 keV (Knoll, 1989; Knox & Miller, 1972). On the other hand, the scintillating photon can be produced by photo electric effect, Compton scattering or pair production. However, the low Z value type of liquid scintillator has been dominated by Compton scattering at energies of a few MeV.

For scintillation detectors, the heavier particle such as neutron, proton, αs and other ions produce the LO by nuclear recoil and generally energy has non-linear behavior against LO (Birks, 1951). If we consider a fast electron, the LO can be described by

$$L = SE\ , \tag{5.3}$$

together with its differential form given as

$$\frac{dL}{dx} = S\frac{dE}{dx} \ , \tag{5.4}$$

where S is called absolute scintillation efficiency. Each individual scintillator molecule is excited by fast electrons without interacting with each other which consequently holds the linearity of energy. The ionizing particles heavier than the electrons of the same energy leave denser ionization in the same scintillating medium and dE/dx is larger for those particles. Therefore, scintillation response decreases as the recoil particle gets heavier, which is known as quenching effect.

This effect was tried to be explained by imposing the term BdE/dx to the Birks formula as follows

$$\frac{dL}{dx} = \frac{S\frac{dE}{dx}}{1+kB\frac{dE}{dx}} \ , \tag{5.5}$$

where B is a proportional constant and k is the quenching parameter. As in the case of fast electrons, the above formula can be reduced to Equation 5.3 on the limit of smaller dE/dx. For higher limit of dE/dx, however, it becomes

$$\frac{dL}{dx} = \frac{S}{kB} \ , \tag{5.6}$$

$$L = \frac{S}{kB}x \ , \tag{5.7}$$

which is proportional with LO for heavy ions at relatively low energies and called saturation effect (Birks, 1951,6). The Birks formula has worked well except for few discrepancies in data, when he firstly proposed it in 1951. Its modified version posted on the following years with higher order terms as extended Birks formula (Chou, 1952) is given as

$$\frac{dL}{dx} = \frac{S\frac{dE}{dx}}{1+kB\frac{dE}{dx}+C(\frac{dE}{dx})^2} \ . \tag{5.8}$$

Equation 5.8 fits the data better in case of the linear behavior for small dE/dx as $L = SE$ for recoil electrons. The LO can be defined as a function of recoil energy with semi-empirical formula studied by Cecil et al. (1979) and provided by the producer company (Sain Gobain ∼ Liquid Scintillators, 2018) as following

$$L(E) = A_1 \times E - A_2(1 - e^{-A_3 \times E^{A_4}})\ . \tag{5.9}$$

Thus, the L(E) is associated with electron equivalent (eV_{ee}) energy. The numerical values of parameters A_1, A_2, A_3 and A_4 in Equation 5.9 are listed in Table 5.1 and illustrated in Figure 5.4. These parameters have been taken from Cecil et al. (1979); Czirr et al. (1964); Verbinski et al. (1964) for α and proton and from Yoshida et al. (2010) for ^{12}C nuclei after best-fitting of the data.

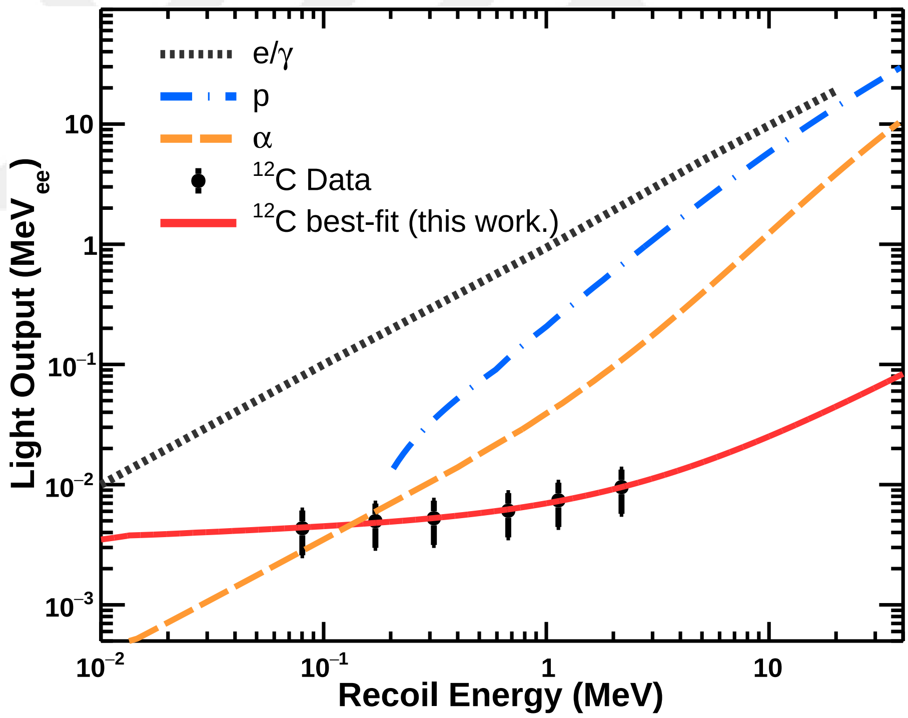

Figure 5.4 The LO from BC-501A due to different particles as function of their kinetic energy. The data for ^{12}C nuclei is adopted from (Yoshida et al., 2010)

The recoil energy of neutron is associated with scattering angle and given by the

Table 5.1 Quenching factor parameters as given in Equation 5.9 of BC-501A liquid scintillator for proton and alpha particles from (Cecil et al., 1979; Czirr et al., 1964; Verbinski et al., 1964) and ^{12}C nuclei from the best fit as illustrated in Figure 5.4 for the data from (Yoshida et al., 2010)

Particle	A_1	A_2	A_3	A_4
p	0.83	2.82	0.25	0.93
α	0.41	5.9	0.065	1.01
^{12}C	0.02	0.85	-0.006	0.069

following equation for different nuclei in the lab frame

$$E_R = \frac{4A}{(1+A)^2}(cos^2\theta)E_n \; , \tag{5.10}$$

where θ is the scattering angle of the recoil particle and A is the mass number of

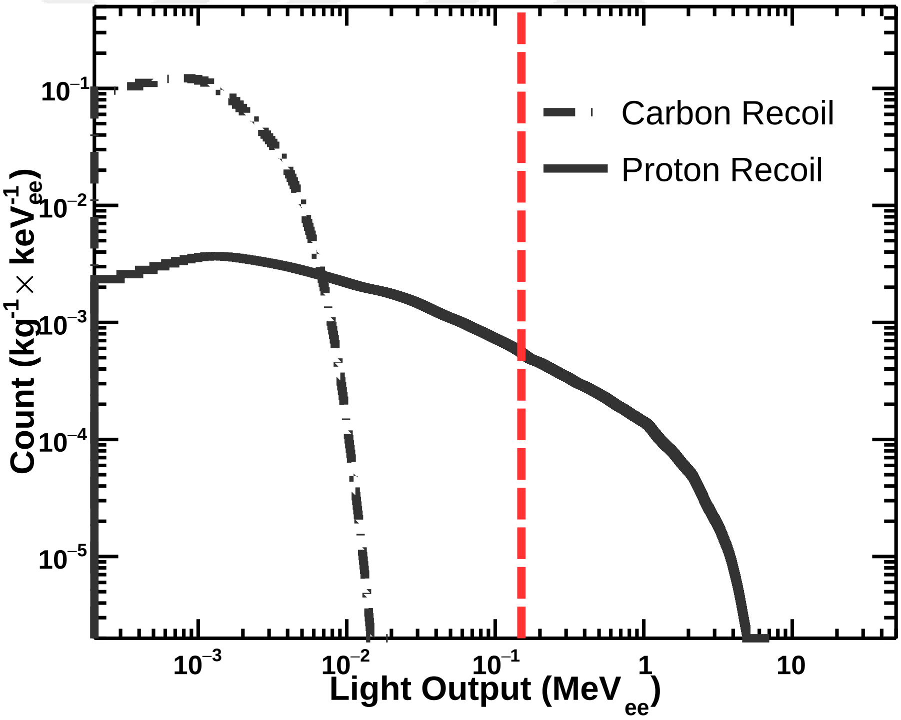

Figure 5.5 Simulated ^{241}AmBe(α,n) neutron spectrum for proton recoil and ^{12}C recoil

nuclei. Thus, the maximum energy is transferred to target particle for $\theta = 0$. It is understandable that if the target particle is the proton, neutron can transfer its all energy at the zero scattering angle. On the other hand, neutron can transfer a maximum of 28.4 % of its energy to the ^{12}C nuclei. Moreover, the quenching factor of ^{12}C nuclei is more sever than that of proton so that the highest LO from ^{12}C nuclei is 30 keV$_{ee}$ for 20 MeV neutron energy (Yoshida et al., 2010).

Once understanding the quenching factor, spectrum can be predicted by simulation. As an application of this study and understanding more the quenching factor from proton and ^{12}C nuclei, the ^{241}AmBe(α,n) neutron source is simulated and illustrated in Figure 5.5. As a consequence, the ^{12}C recoil is negligible in this study, which is below the detection threshold for underground neutrons below 10 MeV.

5.2 Data Taking and Detector Performance

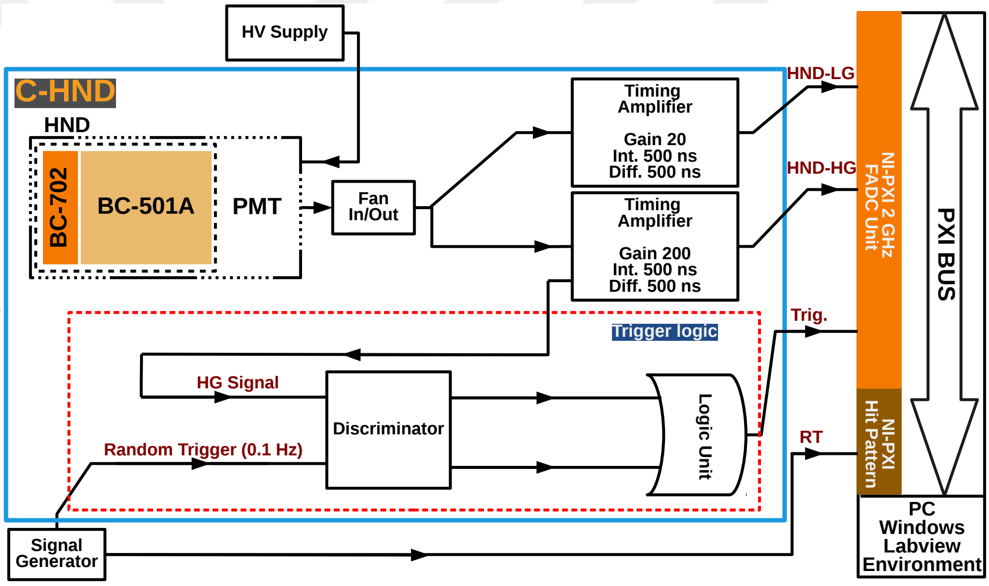

Figure 5.6 (a) The schematic diagram of DAQ circuit for HND

The simple DAQ circuit is illustrated in Figure 5.6. Devices and detector in operation are shown in Figure 5.7. The signal from the anode of the PMT is directly connected to fan in/out to create two identical signals to connect them with two TAs with gains of 20 and 200 for the high energy and the low energy settings, respectively. These two outputs directly feed the NI PXI-5154 FADC with 2 GHz sampling rates and 8 bit dynamic range. However, this rate is reduced in this FADC unit to 1 GHz sampling rates while two outputs connected. With this configuration, high and low energy can be covered at the same time.

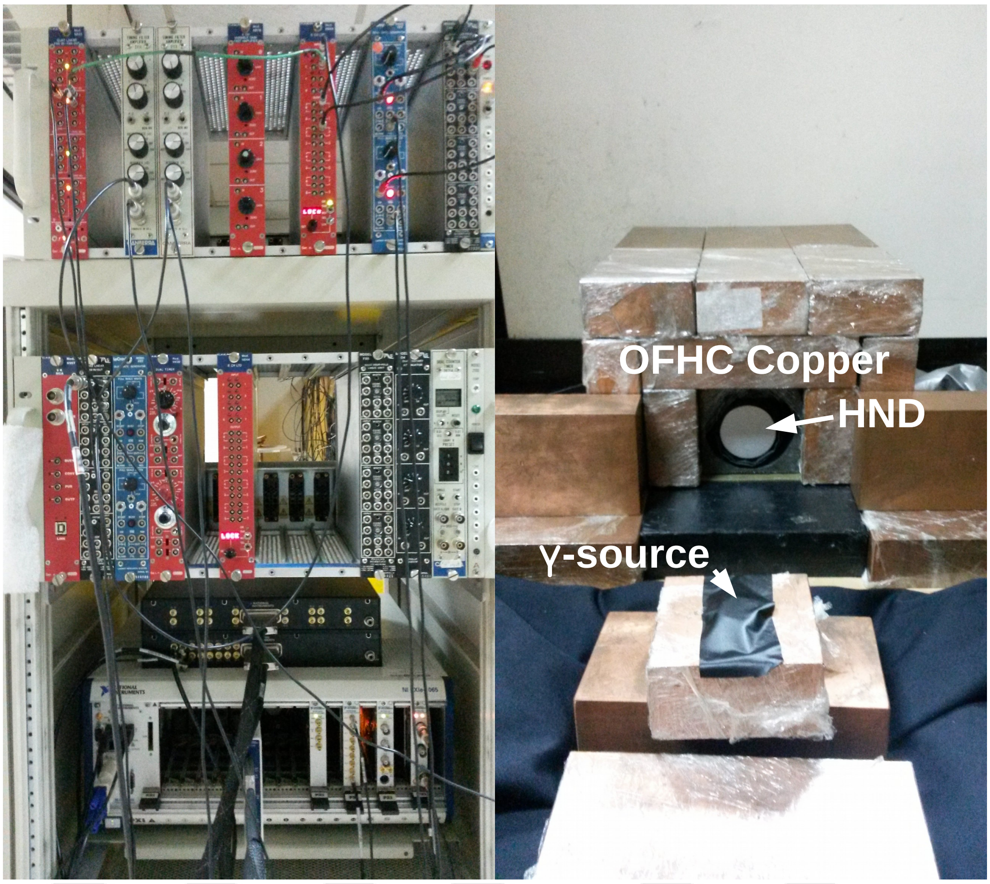

Figure 5.7 The operational devices in the left, and the HND is covered in OFHC copper in the right (Personal archive, 2016)

5.2.1 Event Identification

The shape and height of pulse are two significant parameters to characterize the event and resolution of discrimination. Shape of the signal from scintillation detector can be obtained by evolving the exponential decay behavior of the scintillator with the response function of the PMT and readout system (Knoll, 2000). For the case of a single decay time, the TA output can be described by the difference between two exponential term as follows, (Knoll, 2000)

$$E_{out} = \frac{E\tau_1}{\tau_1 - \tau_2}(e^{-t/\tau_1} - e^{-t/\tau_2}) \, , \tag{5.11}$$

where τ_1 and τ_2 are time constants of the differentiating and integrating networks on TAs, respectively. On the other hand, Marrone et al. (2002) explained that three exponential terms fit better than two terms and proposed the formula as following (Marrone et al., 2002)

$$L = A \times \left(e^{-\theta(t-t_0) - e^{-\lambda_s(t-t_0)}}\right) + B \times \left(e^{-\theta(t-t_0) - e^{-\lambda_l(t-t_0)}}\right) , \tag{5.12}$$

where A and B are normalization constants, t_0 is reference time and θ, λ_s, λ_l represent decay constants. Thus, the signal output from C-HND DAQ circuit as was explained in the above section is given in Figure 5.8(a) as smoothed with Equation 5.12 and normalized for different type of particles.

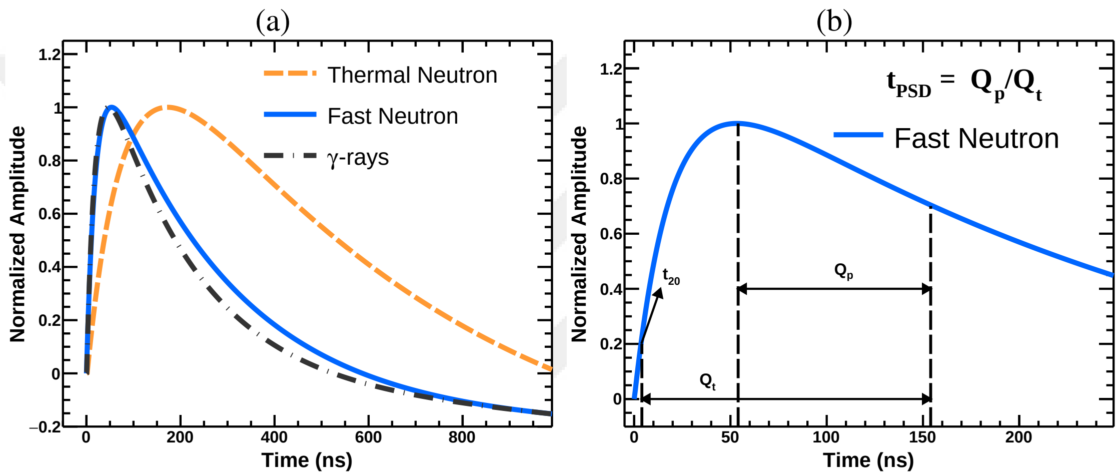

Figure 5.8 (a) Reference pulses for γ-ray, fast and thermal neutron events. (b) The PSD technique variables for integrating range from 20% of pulse height to specific point

As illustrated in Figure 5.8(a), different kind of particle interactions cause distinct signal productions. The ratio of normalization constants B/A in Equation 5.12 can describe different particles for specific scintillators (Marrone et al., 2002). On the other hand, the ratio of partial charges of signal is another method to describe different particles. For this PSD technique, the integration ranges for partial charge (Q_p) and total charge (Q_t) definition is illustrated in Figure 5.8(b) and described the PSD parameter by the following equation

$$t_{PSD} = \frac{Q_p}{Q_t} = \frac{I[(t_{20} + 50\ ns) : (t_{20} + 150\ ns)]}{I[(t_{20}) : (t_{20} + 150\ ns)]} , \tag{5.13}$$

where t_{20} is the time on 20% of pulse height and I denotes integration of the pulse area.

^{241}AmBe(α,n) is used as a calibration source in this technique.

On the other hand, discrimination via B/A ratio can be studied by obtaining the parameters from reference pulse of a specific γ source as in Equation 5.12. Thus, once the γ events are identified by obtaining parameters, the others can be characterized by mismatching of them. Therefore, the reference pulse has been obtained from the relevant peak of gamma events of ^{60}Co source for the parameters of decay constants θ, λ_s, λ_l and reference time t_0, as in following equation

$$L = A \times \left[(e^{-(t-0.52)/226.6} - e^{-(t-0.52)/17.23}) + 0.115(e^{-(t-0.52)/226.6} - 1) \right] , \quad (5.14)$$

where A remained as a free parameter. The exponential term in Equation 5.12 with λ_l decay constant goes unity with a small constant 3.72×10^{-14}. Thus, each individual pulse is fitted to Equation 5.14 to obtain the B/A ratio for event identification.

The results of both methods are illustrated in Figure 5.9. The LO distribution of ^{241}AmBe(α,n) and typical background are demonstrated for t_{PSD} parameter in Figure 5.9(a,b) respectively, and B/A ratio method against LO energy is shown in Figure 5.9(c). As is clearly seen from the three bands, the γ/n discrimination of HND is successfully obtained and thermal neutron discrimination is achieved perfectly. The combination of the two methods indicates that there is a consistency of the values on the PSD parameters of γ/n event identification. Both methods choose the same events as is illustrated in Figure 5.9(d). On the other hand, the efficiency of event identification is poor at low energy. The strength of the discrimination can be determined by Figure of Merit (FoM) as the following

$$FoM = \frac{(mean)_n - (mean)_\gamma}{(FWHM)_n + (FWHM)_\gamma} , \quad (5.15)$$

where the mean and FWHM can be obtained from the two-Gaussian fit by the following equation

$$(2\pi\sigma_1^2)^{(-1/2)} e^{-0.5[(x-x_1)/\sigma_1]^2} + (2\pi\sigma_2^2)^{(-1/2)} e^{-0.5[(x-x_2)/\sigma_2]^2} . \quad (5.16)$$

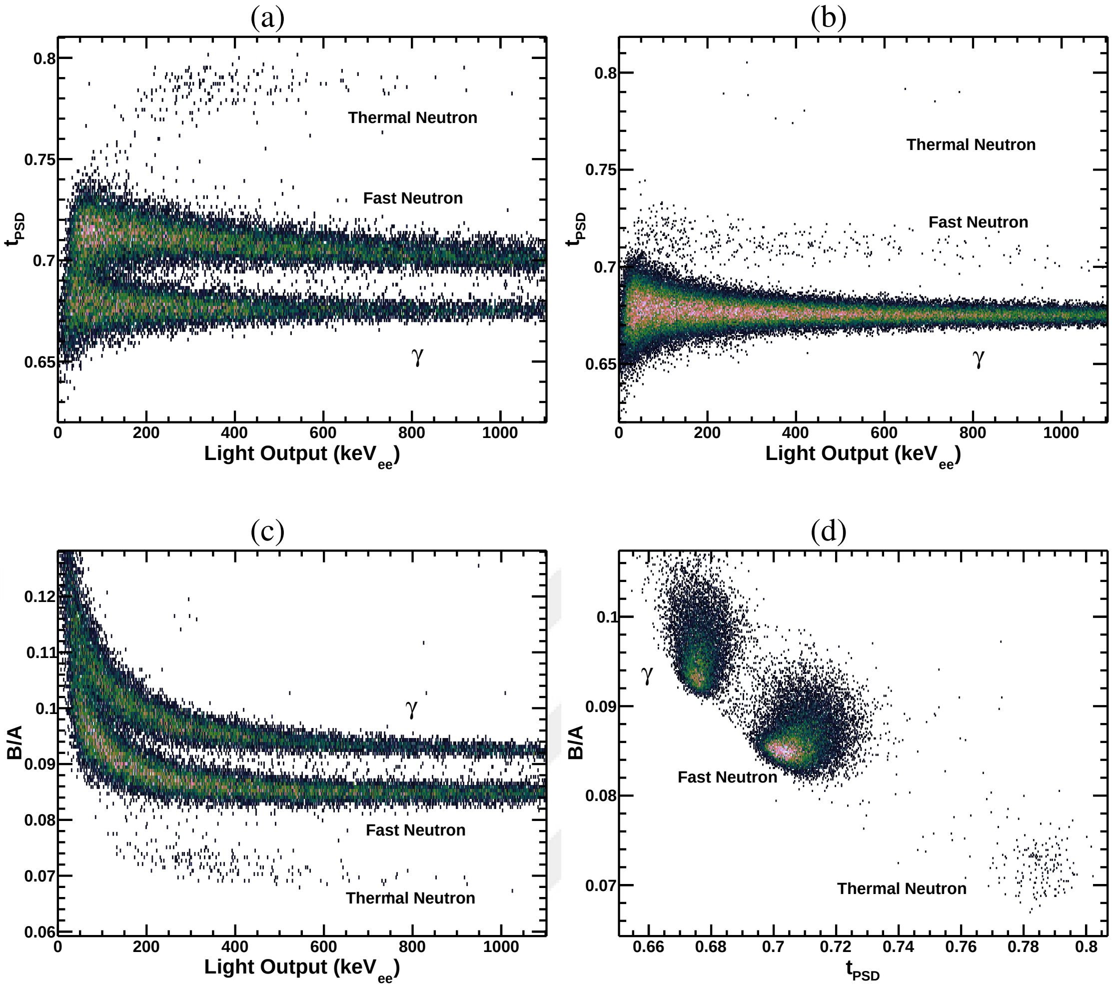

Figure 5.9 The distribution of t_{PSD} variable against LO for , (a) ^{241}AmBe(α,n) source and (b) background. (c) B/A ratio against LO and (d) comparison of both method by projecting B/A ratio into t_{PSD} method

The FoM in Equation 5.15 is demonstrated in Figure 5.10(a) with respect to energy. Strength of discrimination is defined as 1 for FoM. Therefore, the efficiency of discrimination is well enough when the LO is bigger than 150 keV$_{ee}$. The consistency of FoM is illustrated in Figure 5.10(b) and (c) at LO less and bigger than 150 keV$_{ee}$, respectively.

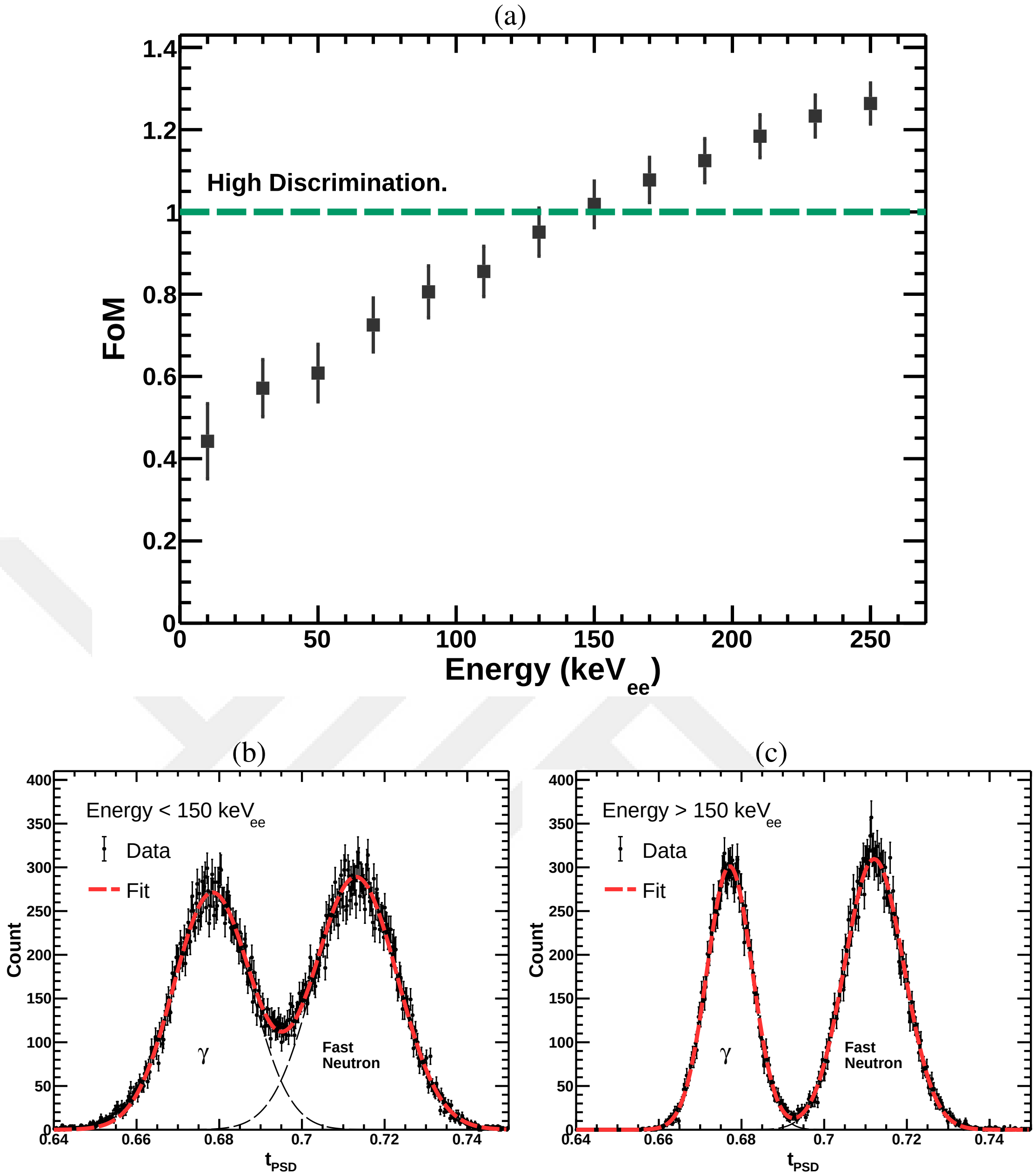

Figure 5.10 (a) The Figure of Merit (FoM) against LO. High discrimination is shown where the FoM exceeds one. (b) t_{PSD} parameter distribution for events (b) LO $<$ 150 keV$_{ee}$ and (c) LO $>$ 150 keV$_{ee}$

5.2.2 Energy Calibration

As was mentioned in Section 5.1.2, the γ source behaves linear against LO and the linearity is consistent with Compton scattering due to low atomic number of target material. Therefore, the γ sources are used for calibrating the energy as listed in Table

5.2.

Table 5.2 The γ sources list with their Compton edge energies that are used in the calibration of BC-501A liquid scintillator.

Source	E_γ (MeV)	E_c (MeV_{ee})
^{22}Na	0.511, 1.274	0.341, 1.062
^{137}Cs	0.662	0.478
^{60}Co	1.173, 1.332	0.963, 1.120

Moreover, every detector has different uncertainty for energy, which is known as energy resolution. This is important information for the detector characterization furthermore, Monte Carlo simulation does not provide the detector resolution therefore spectrum has to be considering with resolution effect for the comparison of experimental data. In addition, for this study Geant4 simulation is provides the response matrix of LO for building neutron energy spectrum. Therefore the characterization of detector energy resolution and the applying its to simulated spectrum is crucial. Thus, the LO resolution function is given by following equation (Klein & Neumann, 2002)

$$\frac{dL(FWHM)}{L} = \sqrt{\alpha^2 + \frac{\beta^2}{L} + + \frac{\gamma^2}{L^2}}\,, \tag{5.17}$$

where α correspond to the position dependence of light transmission, β is related with statistical variation of photoelectron production mechanism and multiplying and γ is associated with electronic noise which is very small and negligible in general.

Thus, the linear energy calibration and the detector resolution function as is given in Equation 5.17 are characterized by fitting to the calibration source listed in Table 5.2 as is illustrated in Figure 5.11 (a) and (b), respectively.

The measured values of resolution function in Equation 5.17 are $\alpha = 12.4\%$, $\beta = 6.1\%$ and $\gamma = 0.008\%$. On the other hand to performing the resolution function on the

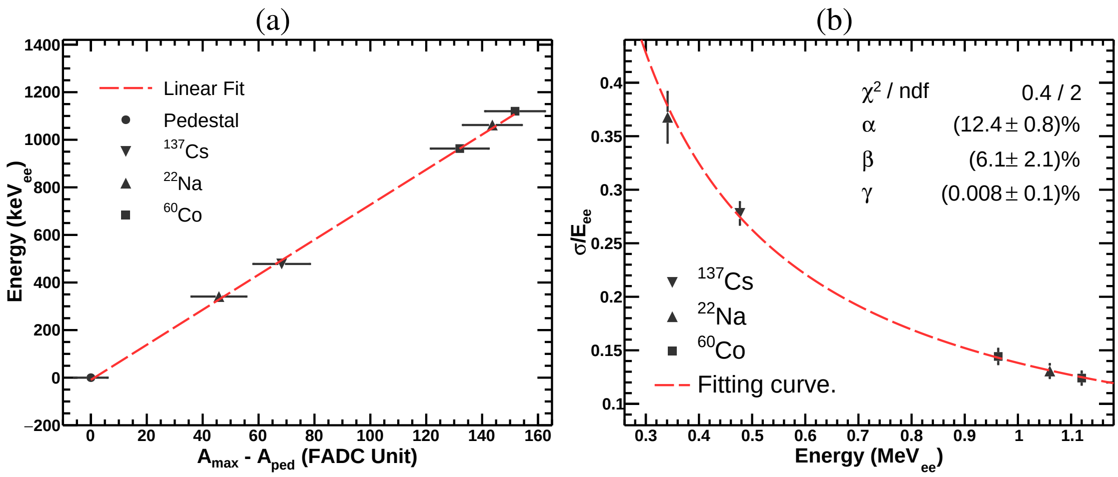

Figure 5.11 (a) Energy calibration of BC-501A in the parameter space of electron equivalent energy against net amplitude of the signal. (b) Energy resolution of BC-501A

simulation, Gaussian distribution for the central energy L_0 can be used as following

$$R_{sim}(L) = \sum_k \int_{L-\Delta L}^{L+\Delta L} \frac{C_k}{\sqrt{2\pi\sigma^2(L_k)}} e^{-0.5[(L'-L_k)/\sigma(L_k)]^2} dL' \,, \tag{5.18}$$

where $R_{sim}(L)$ is simulation light output at energy L, C_k is the count at kth bin and the $\sigma(L_k)$ is represent Gaussian width as an energy dependent, which can be calculate from Equation 5.17 by adopting FWHM conversion of FWHM= $2\sqrt{2ln2}\sigma$ (Glimore, 2008) as following equation

$$\sigma(L) = \frac{dL(FWHM)}{2\sqrt{2ln2}} = \frac{1}{2\sqrt{2ln2}} \sqrt{\alpha L^2 + \beta L + \gamma} \,. \tag{5.19}$$

Thus, detector resolution effect can be adopted on simulation result by using Equation 5.18. The measured data and simulation results with and without resolution are illustrated in Figure 5.12.

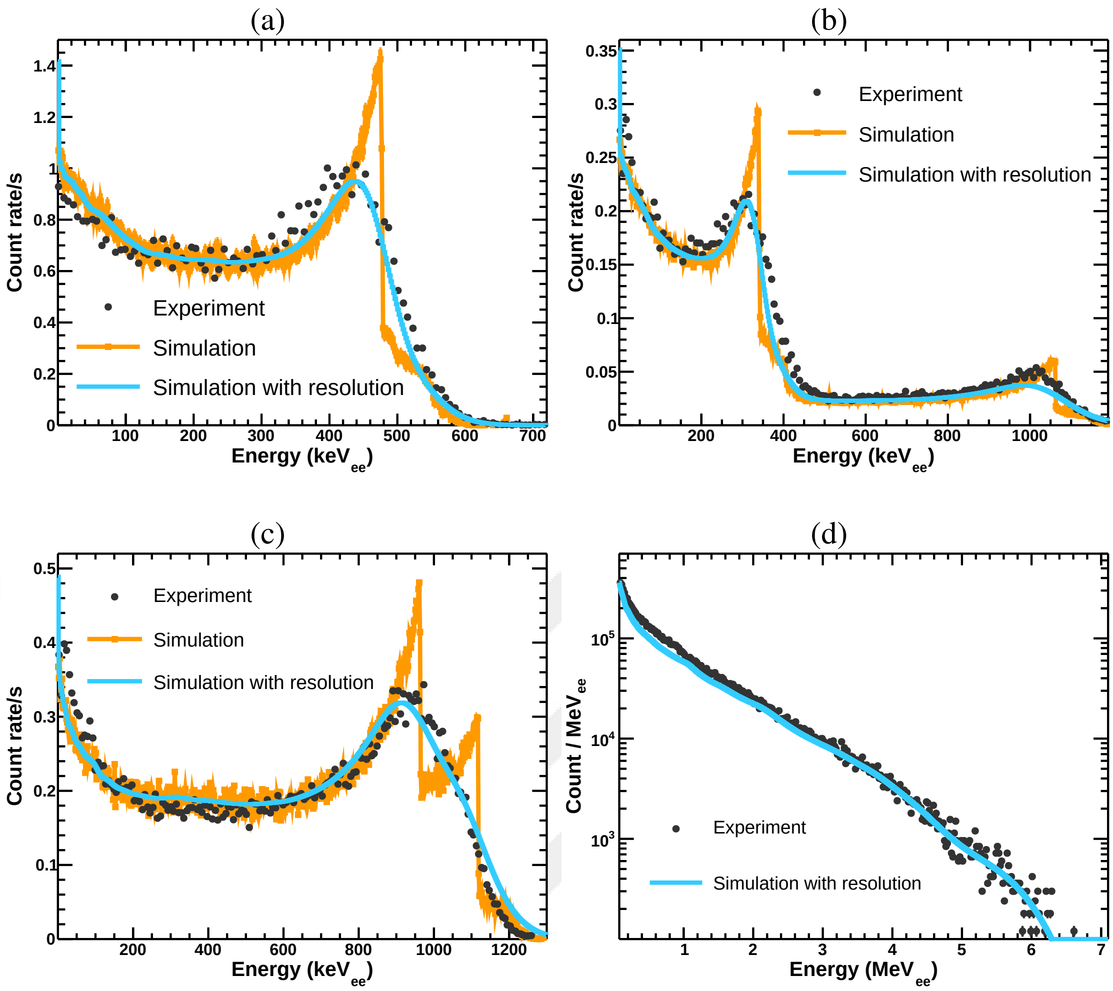

Figure 5.12 Measured data and simulated predictions with and without detector resolution for (a) ^{137}Cs, (b) ^{22}Na, (c) ^{60}Co and (d) ^{241}AmBe(α,n) sources

5.3 Construction of Neutron and Gamma Spectra

So far that the spectra from LO obtained as recoil energy in electron equivalent conversion of quenching effect. Moreover, the events are differentiated by PSD method thus nuclear recoil and electron recoil spectra as well. This two recoil spectra can be constructed in to neutron and gamma energy spectra by known monochromatic LO spectrums. In the measurement of particle detection on HND carried under an arbitrary particle flux of $\phi(E)$, the measured spectrum $N(L)$ can be obtained from

$$N(L) = \int_0^{\infty} \phi(E)R(L,E)dE \ , \tag{5.20}$$

where E is represents incident particle energy, L is corresponds to recoil energy and $R(L,E)$ is the response function of light output at relevant incident particle energy. The integral given in Equation 5.20 may not be solvable for $\phi(E)$ in analytic way. Therefore, the Equation 5.20 can be reorganize for a real measurement as following

$$N_i(L_i) = \sum_j \phi_j(E_j) R_{ij}(L_i, E_j) \; , \tag{5.21}$$

where $R_{ij}(L_i,E_j)$ is similar version of Equation 5.18 for those monochromatic incident particle with energy E_j and called as response matrix (RM) in this form which is provide the simulated LO spectrum for monochromatic incident particle. In this study RM is created by 1000 neutron beam from 0 to 20 MeV and each LO spectra is produced in probability unit. The response of the detector is start from 100 keV neutron energy. The RM sample for few γ and neutron beam is illustrated in Figure 5.13.

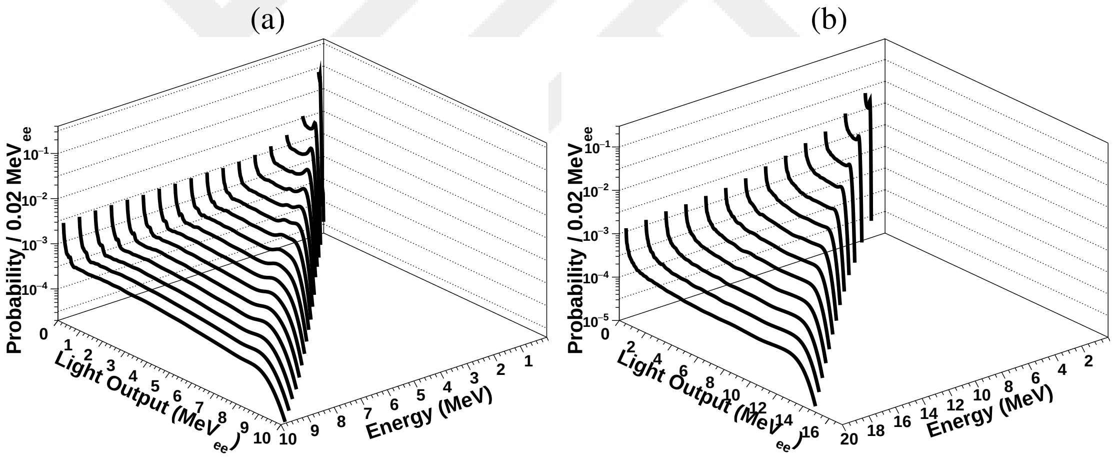

Figure 5.13 The response matrix for few (a) γ and (b) neutron beam

The solution of Equation 5.21 to finding $\phi_j(E_j)$ requires developing a computational method for numerical deconvolution which is widely used in in neutron spectroscopy and dosimetry applications as called unfolding method. The LO from the measurement is called as folded spectra and constructed spectrum from its by unfolding method is called as unfolded spectra. This method had been developed in widely use for γ/neutron dosimetry measurement to use where it is important to know the abundance of the γ/neutron radiation like nuclear facilities. There are several algorithms for unfolding in literature. However in this study, two of them used which are Doroshenko (Wolski, 1995) and Gravel methods (Matzke, 1994). Both method are using iterative algorithms.

The algorithm of Ddroshenko method is given by following equation

$$\phi_j^{n+1} = \frac{\phi_j^n}{\sum_i R_{ij}} \sum_i R_{ij} \frac{N_i}{\sum_k \phi_k^n R_{ik}} \ , \tag{5.22}$$

where N_i is the ith bin of the measurement, R_{ij} is response matrix and ϕ_j is neutron flux. The algorithm is working with an initial ϕ_j^0 flux and the last iteration is provide the neutron flux. The decision of the ending point of iteration algorithm is one of the problem for such that iterative methods. To testing of the algorithm, the folded spectrum can be reconstruct from the obtained flux as given Equation 5.21 previously. Thus, the reconstructed recoil spectrum can be define as

$$N_i^{(R)} = \sum_j \phi_j^n R_{ij} \ . \tag{5.23}$$

Thus, the matching of recoil spectrum and reconstruction of its can be test by χ^2-testing as follow

$$\chi^2/n.o.f = \frac{1}{n.o.f} \sum_i \frac{\left(N_i^R - N_i\right)^2}{\sigma_i^2} \ , \tag{5.24}$$

where σ_i is the error of measurement. In this way, end point of the iteration can be determined by χ^2-testing.

On the other hand, the Gravel unfolding method can be written from following equation

$$\phi_j^{n+1} = \phi_j^n exp\left(\frac{\sum_i W_{ij}^n ln\left(\frac{N_i}{\sum_k \phi_k^n R_{ik}}\right)}{\sum_i W_{ij}^n}\right) \ , \tag{5.25}$$

where W_{ij} is a weight factor defines as,

$$W_{ij}^{n} = \frac{R_{ij}\phi_j^n}{\sum_k \phi_k^n R_{ik}} \frac{N_i^2}{\sigma_i^2} . \tag{5.26}$$

Both algorithm is developed for computational application by ROOT (Brun & Rademakers, 1997) interface with C++ source code and shared in public (Sonay, 2017). The unfolded spectrum results for folded γ spectras which are illustrated in Figure 5.12 are demonstrated in Figure 5.14.

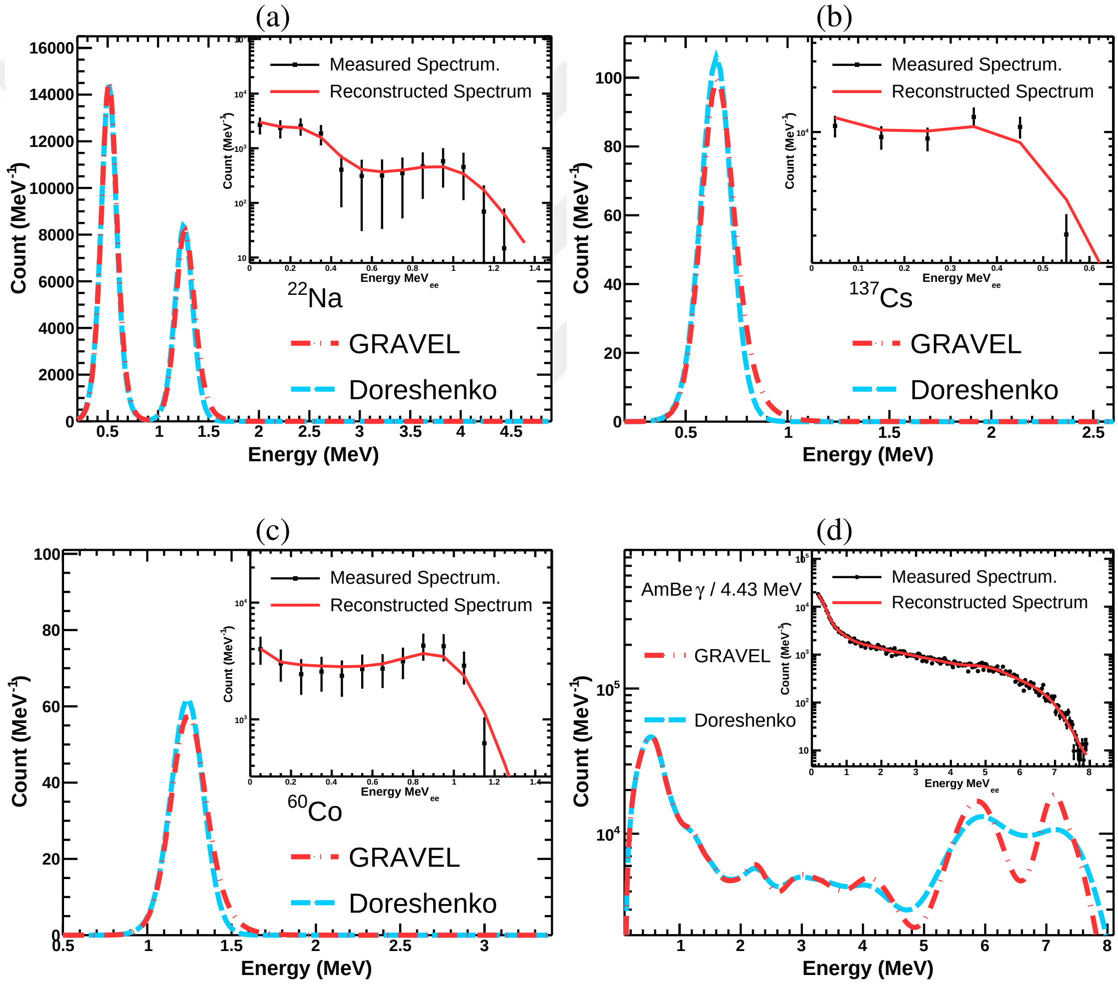

Figure 5.14 Folded and unfolded spectra for γ sources (a) ^{22}Na, (b)^{137}Cs, (c)^{60}Co, (d) ^{241}AmBe(α,n) sources. Reconstructed folded spectrum shows the fitting to data

The γ-ray peaks location at the mean of ^{22}Na, ^{137}Cs, ^{60}Co are (524 $\pm$ 27.8, 1277.8 $\pm$ 93.1) keV$_{ee}$, (666.9 $\pm$ 80.6) keV$_{ee}$ and (1254.7 $\pm$ 105.9) keV$_{ee}$, respectively.

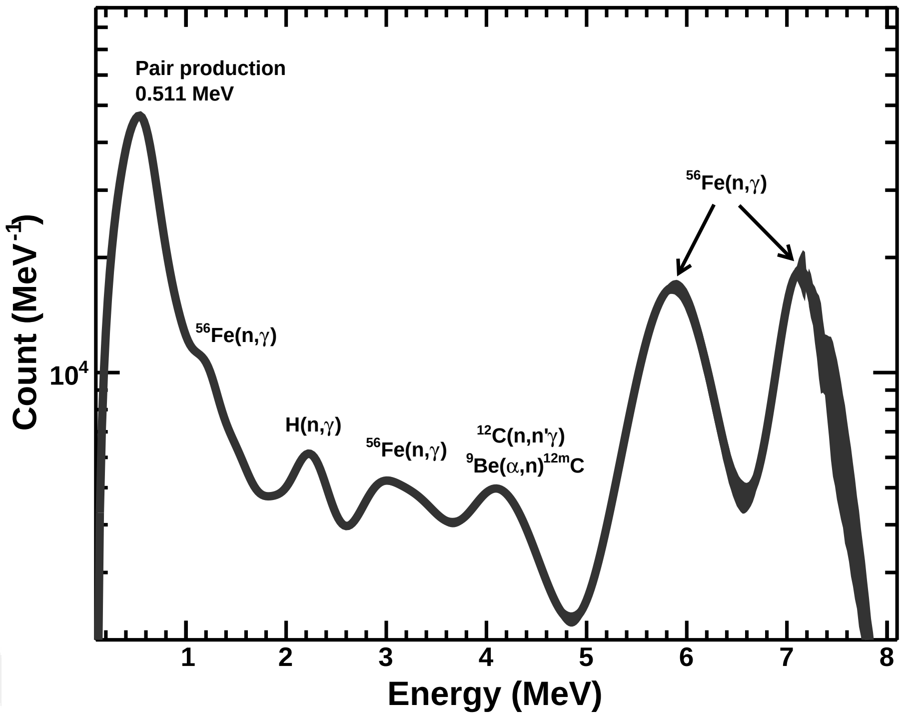

Figure 5.15 Unfolded γ spectrum of ^{241}AmBe(α,n) source by neutron capture of elements and ^{9}Be(α,n)^{12m}C line at 4.43 MeV due to reaction of neutron source

Both method have slightly similar results. However, the significant distinction emerges in Figure 5.14(d) for the unfolded spectra of ^{241}AmBe(α,n) source. The peaks on the figure have better distinction for Gravel method yet its still has poor resolution so much that peaks and single escape (SE) peaks cannot separated. The γ-peaks due to neutron captures are illustrated in Figure 5.15 for ^{56}Fe(n,γ) on several energies (7.6, 5.9, 3.0, 1.1) MeV, H(n,γ) at 2.26 MeV and ^{12m}C line at 4.4 MeV due to inelastic neutron scattering with carbon and ^{9}Be(α,n) reaction. The unfolded γ spectrum may not be applicable due to poor energy resolution according to other scintillation detectors. However, the emerging of some characteristic γ-ray peaks shows that, the unfolding method is working successfully and may be applicable on neutron spectrum detection.

The neutron folded spectrum of ^{241}AmBe(α,n) source as well as the reconstructed folded spectrum from the unfolding, and the simulated LO is shown in Figure 5.16(a). The unfolded spectrum from simulated LO is represented on background for both unfolding method in Figure 5.16(b). The matching of its with the measurement AmBe neutron spectrum from Kluge and Weise (1982) is quite good as expected which is an

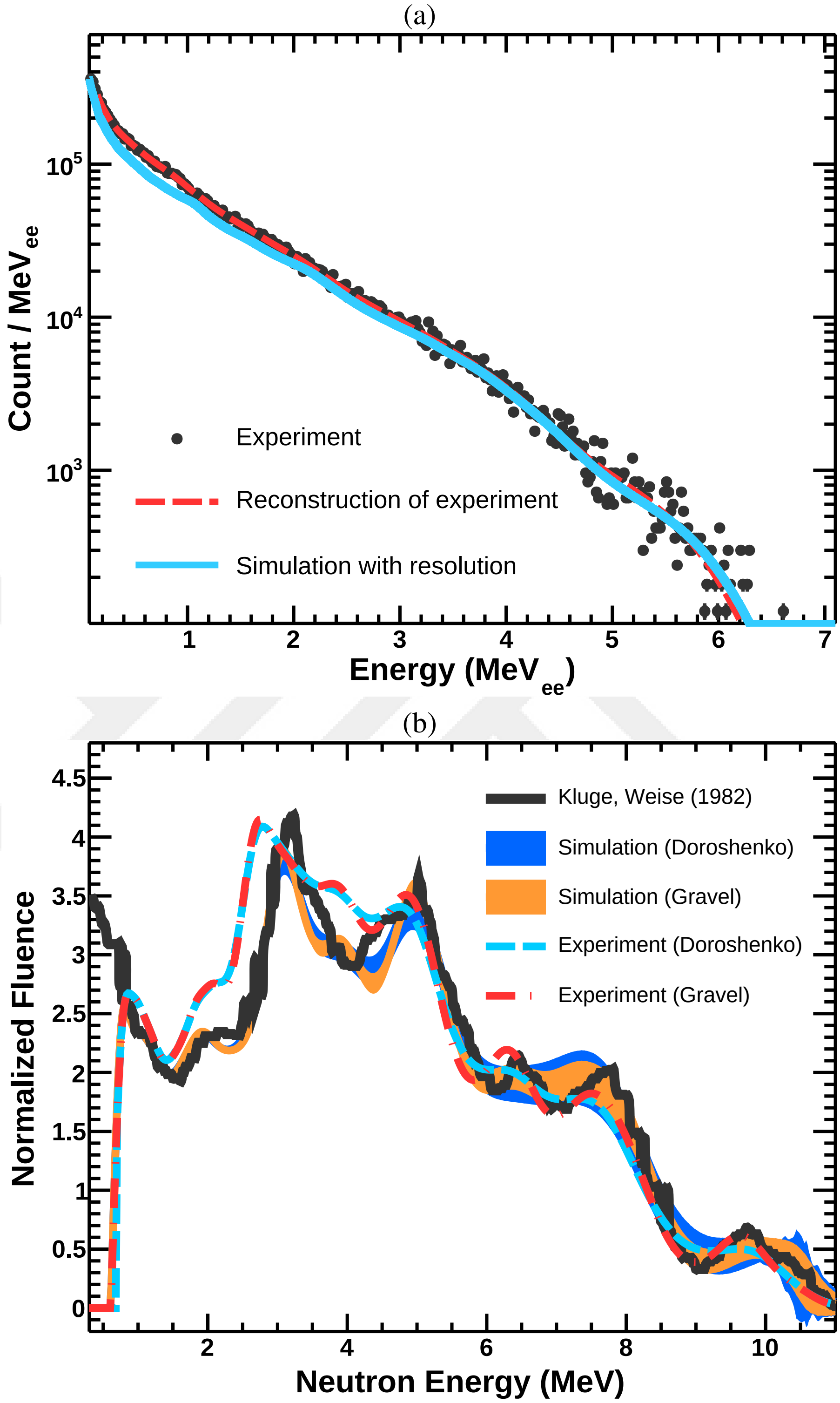

Figure 5.16 (a) Measured and simulated spectrum of ^{241}AmBe(α,n) and the reconstruction from unfolded spec ϕ_j by Equation 5.23. (b) The unfolded ^{241}AmBe(α,n) for both technique of Doroshenko and Gravel in comparison with the measurement of Kluge and Weise (1982) and the unfolded spectra from the simulated LO (Kluge & Weise, 1982)

strong evidence that showing the method strength. On the other hand, the unfolded spectrum of experimental data is matching well at higher energy as in recoil spectrum well. The excess at low energy among the experimental data and simulation as illustrated in Figure 5.16(a), is emerge unfolded spectra in (b) as well.

It is understood from the results, the unfolding method prove itself by testing on known neutron and gamma spectrum sources and it is applicable for neutron spectrum measurements. Therefore fully characterized this HND can be move on the experiment site for measuring of the thermal and fast neutron flux and their spectrum as well. Thus, once the spectrum are measured under same shielding configuration, the neutron background contribution on HPGe spectrums can be understood.

CHAPTER SIX
NEUTRON BACKGROUND IN THE KSNL

Thus far, the HND characterization is completed and neutron spectra construction by unfolding method is compared with known ^{241}AmBe(α,n) source. The γ/n discrimination of HND is investigated and founded that the neutron transferring its energy above the 150 keV$_{ee}$ LO is differentiated well. In this schem, the same DAQ circuit was moved to integrating on the KSNL scene and was installed at the same location as the various HPGe within the well of an NaI(Tl) AC detector and kept under the same shielding configurations and data taking conditions. Thus, the fast and thermal neutron activation among the background channels of KSNL can be investigated and the contribution of neutron background on the neutrino and WIMP candidate spectrums of HPGe detectors as illustrated in previous sections in Figure 4.9 can be determined. This can be done by Geant4 simulation after determined the neutron background *in situ*.

However, before starting the experimental details of neutron background measurement, the X-ray lines in the HPGe results of the neutron induced isotopes can be researched to obtain neutron rate. Thus the experiment of neutron background under the same identical shielding configuration with HPGe can be tested through the consistency with HPGe result.

6.1 Neutron Induced Isotopes on the HPGe Spectrum

The HPGe spectrum can be directive on prediction of neutron background. The lines on the HPGe which are used in calibration as give in Table 4.2, are mostly activated by cosmic induced neutrons. The most dominated line at 10.37 keV$_{ee}$ occurs by K-X line of ^{68,71}Ge electron capture (EC) and ^{68}Ga as daughter of ^{68}Ge is decaying to ^{68}Zn by electron capture and radiate K-X line at 9.66 keV$_{ee}$. Possible producing paths of ^{68,71}Ge by neutron interaction is summarized in Table 6.1.

Table 6.1 The production paths of ^{68,71}Ge isotopes due to neutron interaction

Channel	Interaction	Decay of Product	Half-Life of Product
n-inelastic	^{70}Ge(n,3n)^{68}Ge	^{68}Ge(e$^-$,ν_e)^{68}Ga – ^{68}Ga(e$^-$,ν_e)^{68}Zn	270.95 (day) ,67.7 (min)
n-inelastic	^{72}Ge(n,2n)^{71}Ge	^{71}Ge(e$^-$,ν_e)^{71}Ga	11.43 (day)
n-capture	^{70}Ge(n,γ)^{71}Ge	^{71}Ge(e$^-$,ν_e)^{71}Ga	11.43 (day)

Therefore, time variation of two X-ray line due to EC of ^{68,71}Ge and ^{68}Ga isotopes can be investigate for understanding of neutron background contribution. The time variation of those X-ray lines are shown in Figure 6.1(a)-(b) and the rate from the time variations is illustrated on nPCGe CR$^-$ $\otimes$ AC$^-$ spectrum in Figure 6.1(c). The data was collected a total of 347 live-time day for this 500g nPCGe. The measured rates of ^{68,71}Ge and ^{68}Ga are summarized in Table 6.2.

Table 6.2 Summary of the measured ^{71}Ge/^{68}Ge (10.37 keV$_{ee}$) and ^{68}Ga (9.66 keV$_{ee}$) K-X rates at KSNL − for both transient and in equilibrium components

Channel	Half-Life ($\tau_{\frac{1}{2}}$)(day)		Rate
Measurements	Nominal	Measured	(kg^{-1} day^{-1})
^{71}Ge from Transient 10.37 keV$_{ee}$ K-X	11.43	10.63 ± 1.08	2.70 ± 0.90
^{68}Ge from Transient 10.37 keV$_{ee}$ K-X	270.95	275.76 ± 9.01	23.9 ± 6.4
^{68}Ge from Transient 9.66 keV$_{ee}$ K-X	270.95	246.74 ± 46.16	2.2 ± 0.6
Equilibrium 9.66 keV$_{ee}$ K-X			
=^{70}Ge(n,3n)^{68}Ge			< 0.39
Equilibrium 10.37 keV$_{ee}$ K-X			
=[^{70}Ge(n,γ)^{71}Ge+^{70}Ge(n,3n)^{68}Ge]			12.40 ± 3.70

The time variation of both isotope ^{71}Ge/^{68}Ge is not tending to zero, which is mean that, isotopes feeding by neutrons and at the some point reaches to equilibrium. This equilibrium levels are given in Table 6.2 as well. The level of 9.66 keV$_{ee}$ is consistent with zero thus it is understood from that, the daughter of ^{68}Ge and it self does not feed by neutrons under the KSNL shielding. On the other hand, this is known that from the Geant4 simulation, the threshold of ^{70}Ge(n,3n)^{68}Ge interaction is above 20 MeV neutron energy. The interaction of germanium with the neutrons and production of

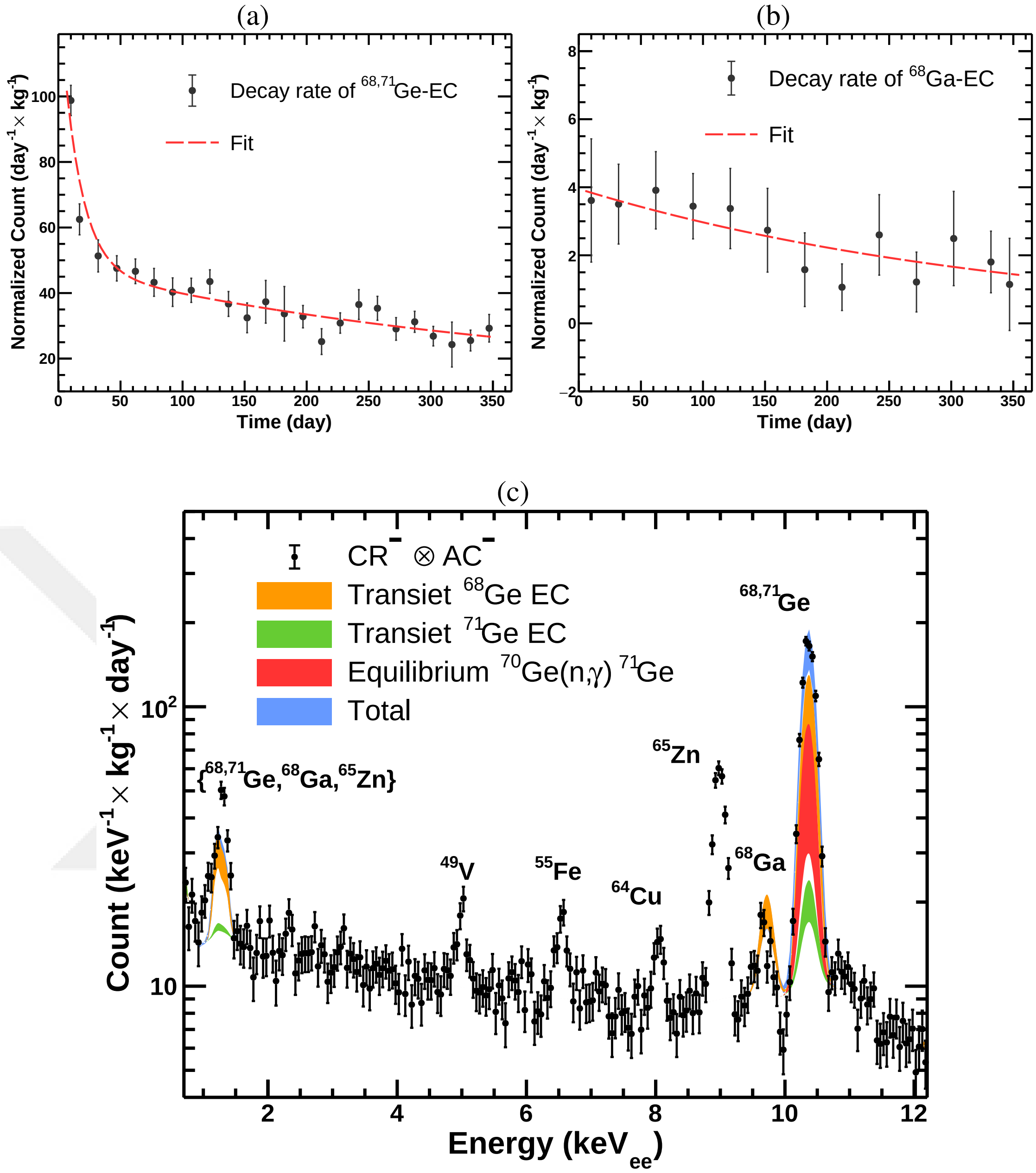

Figure 6.1 The time variation of X-ray lines of (a) ^{68,71}Ge at 10.37$_{ee}$ keV and (b) ^{68}Ga at 9.66$_{ee}$ keV. (c) nPCGe CR^{-} $\otimes$ AC^{-} spectrum and superimpose of X-ray lines according to their rate which are measured from (a) and (b)

^{71}Ge/^{68}Ge isotopes are illustrated in Figure 6.2 as relatively each other.

As a consequence, under the shielding of KSNL, only contributor of the equilibrium level of 10.37 keV$_{ee}$ line is from the ^{71}Ge isotopes due to neutron capture of the ^{70}Ge, where the expected neutron spectrum is below 10 MeV for underground lab-

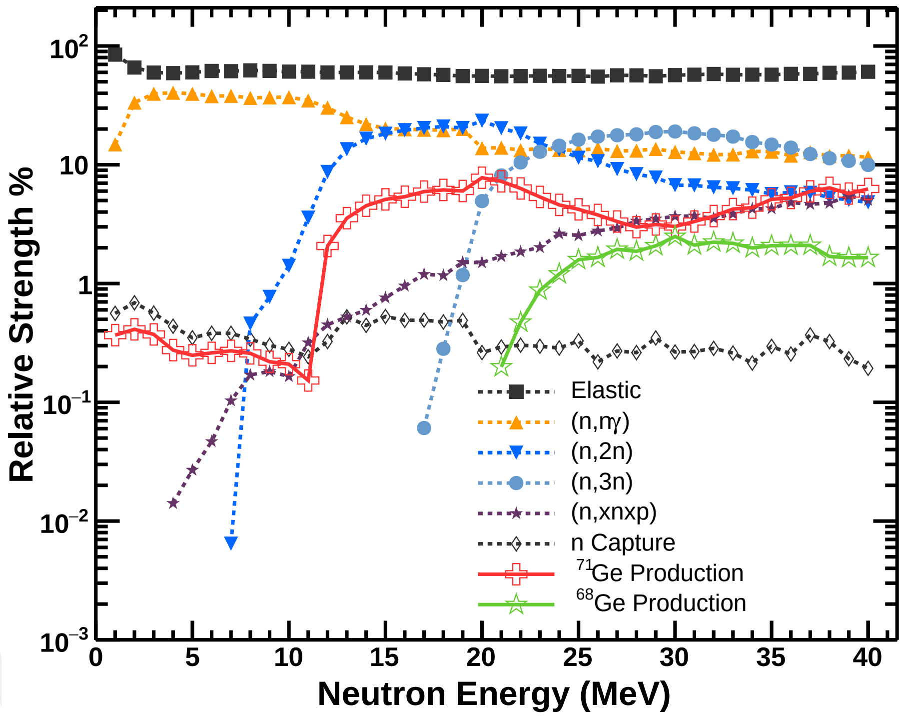

Figure 6.2 The relative strength of neutron interactions with germanium against neutron energy and the production of ^{71}Ge/^{68}Ge isotopes

oratories. Therefore, the measured neutron background should be consistent with the ^{70}Ge(n,γ)^{71}Ge equilibrium yield by $\Delta R_n \times R_n$ where ΔR_n is the efficiency of ^{70}Ge(n,γ)^{71}Ge interaction on the germanium for the measured spectrum and R_n is the measured rate.

6.2 Integration of HND in to KSNL.

The characterization of HND was performed at outside the KSNL. Therefore, the optimization of HND for the KSNL experiment is necessary. This optimization has to be done very carefully on DAQ integration level on KSNL and the basic filtering, CR and AC system calibration as well as event identification on the analyzing part should be repeated for this new detector. However, this parts was done once as expleined in Chapter 4 and all the procedure was repeated also for HND with few difference. The main difference is categorizing particles by the PSD method that allows the identification of neutron events which is the main goal of this study.

6.2.1 Experimental Setup

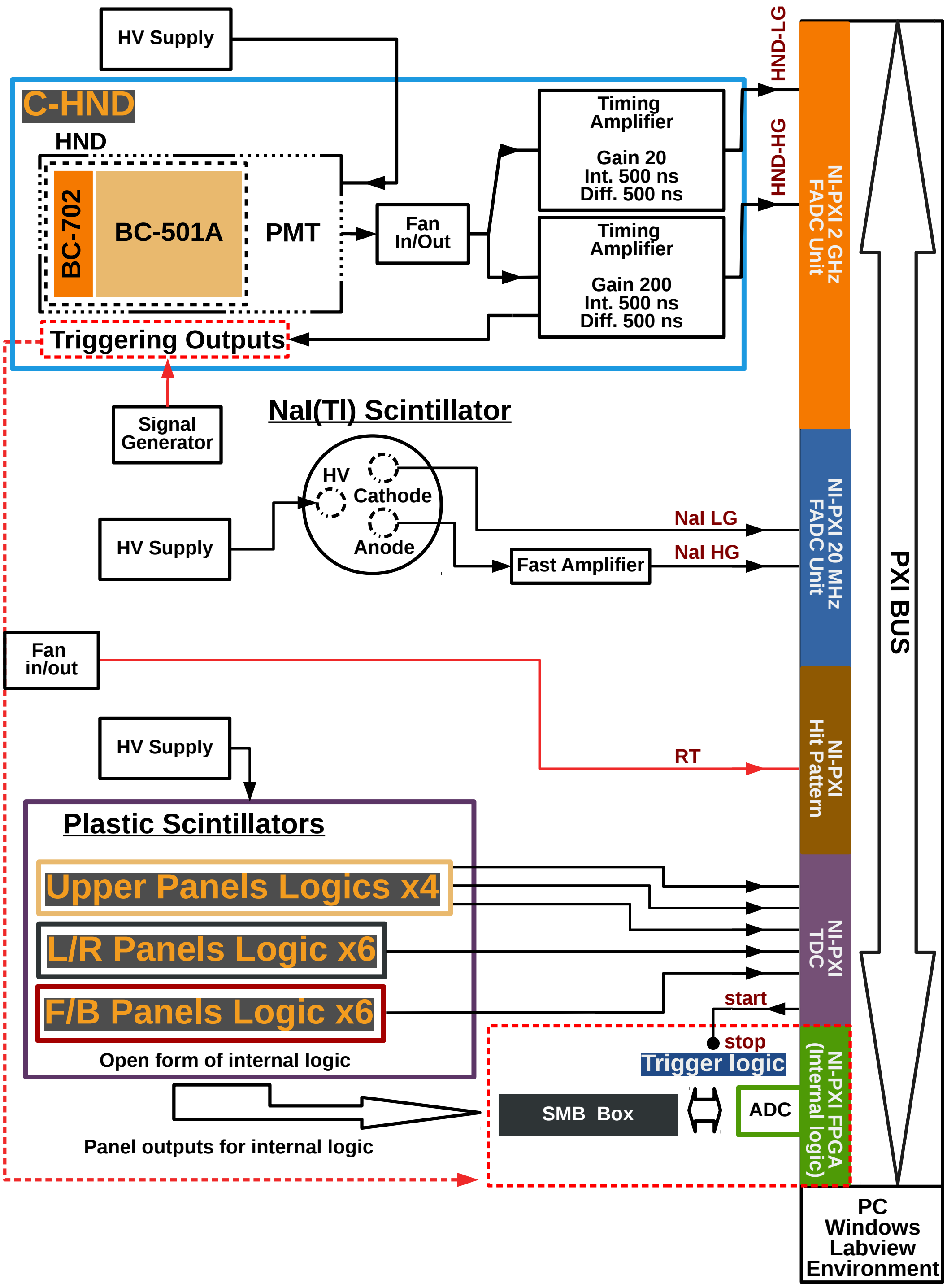

Figure 6.3 The schematic view of DAQ system in the KSNL for HND. Triggering system as same as shown in Figure 5.6

The data taking system of KSNL is similar as described in Section 3.3. In the DAQ circuit as illustrated in Figure 3.9, the germanium detector section (C-Ge) is replacing with C-HND which is shown in Figure **??**(a). Therefore, inhibit signal, test pulser, 60 MHz and 200 MHz FADC units has removed from the system and NI PXI-5154 FADC unit with 2GHz sampling rates was installed in place of the removed FADCs as illustrated in Figure 6.3. The data was collected a total of 33.8 live-time day for the HND.

6.2.2 Event Selection and the Efficiency of Integrated System

The HND data was collected under same identical shielding of HPGe experiment. For this data set, the selection rules has performed as similar with HPGe analysis as basic filtering, active shielding labeling and the PSD method of HND owns. The PSD selection for event identification is illustrated as three band (γ/n$_{fast}$/n$_{thermal}$) in Figure 6.4. The parameter of PSD selection from the two method for t_{PSD} and B/A are similar as depicted in previous chapter as in Equation 5.13 and 5.14, respectively. The correlation between this two method is illustrated in Figure 6.4 (b) as evidence of two independent method selecting same events under tagging of γ, n$_{fast}$ or n$_{thermal}$.

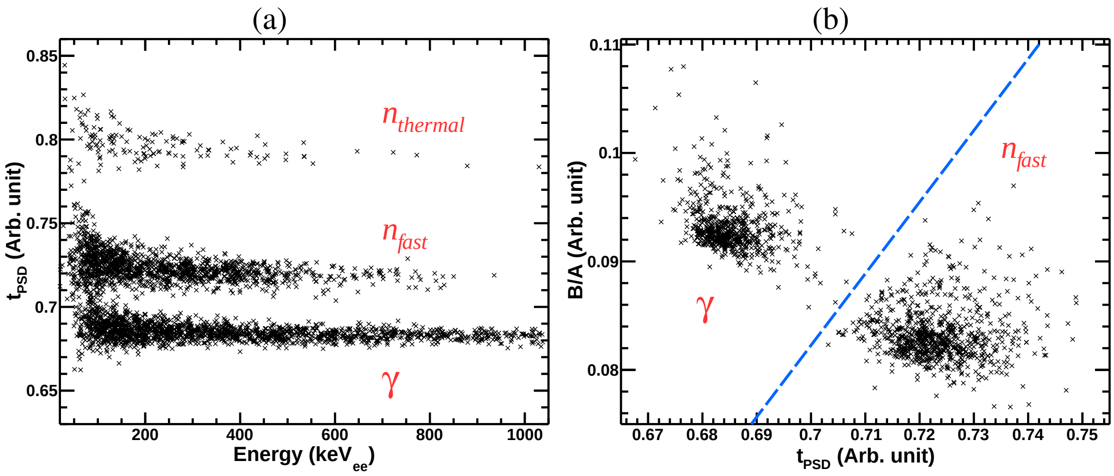

Figure 6.4 (a) The distribution of t_{PSD} variable against LO. (b) Comparison of two method among the B/A and t_{PSD}

The labeling of CR and AC system is illustrated in Figure 6.5, Thermal and fast neutrons demonstrated in Figure 6.5 (a) and (b) for CR and AC tagging, respectively.

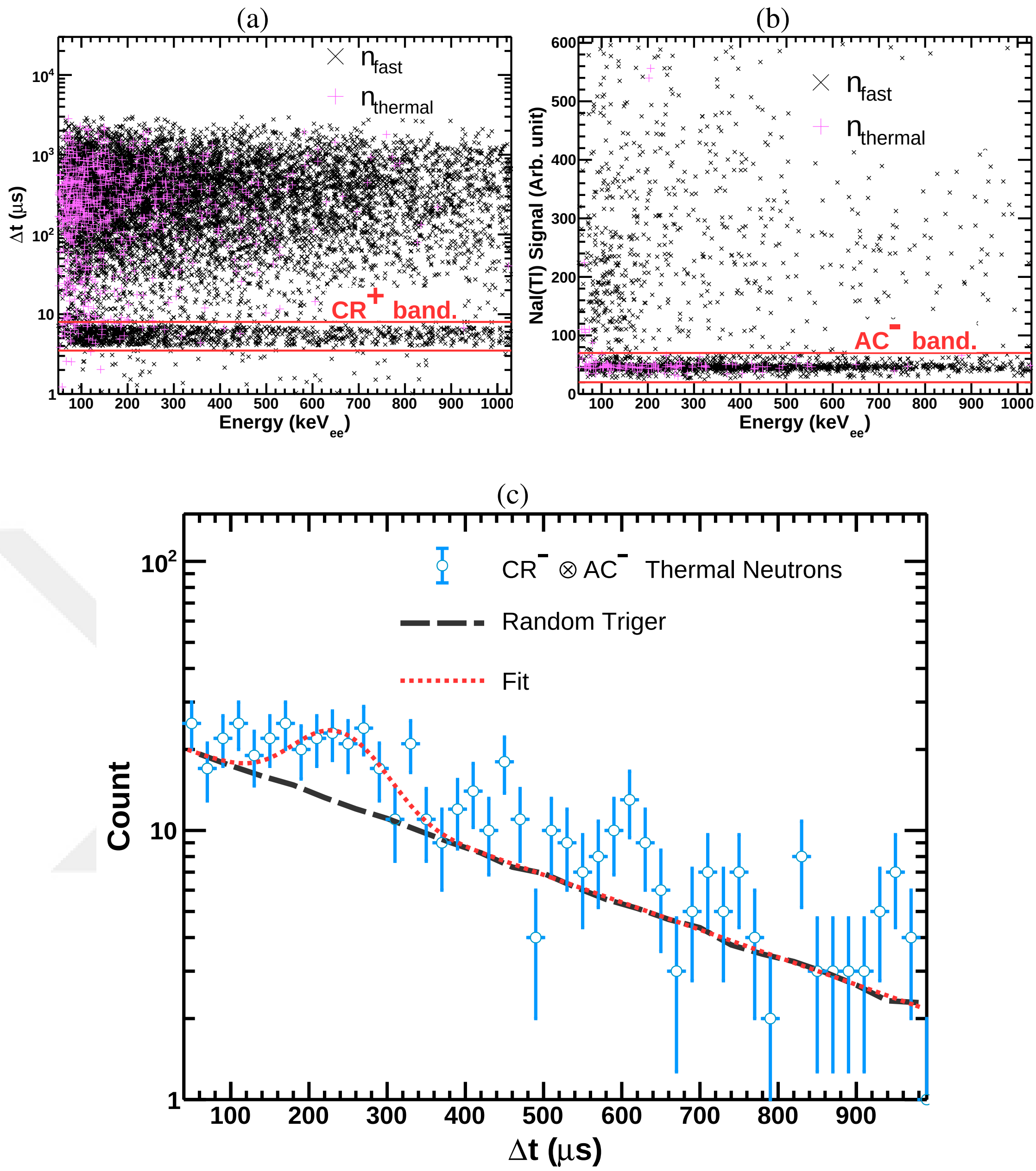

Figure 6.5 The projection of HND signal into (a) CR signal, (b) AC signal. (c) The time difference among the previous CR^+ with $CR^- \otimes AC^-$ events

It is understandable from the figure that, most of the thermal neutrons tagged by $CR^- \otimes AC^-$, which is mean that, most of them are not coincidence with CR and AC system. In general, thermal neutrons are scattered multiple times inside the materials which is causes the delaying. The cosmic ray induced fast neutrons can be thermalized by losing their energy while scattering through inside the materials and delayed those thermal neutrons can reach the HND. Therefore, this delayed thermal neutrons related with cosmic rays can be investigate by time difference of those event with previous CR^+. This time difference is illustrated in Figure 6.5 (c) with accidental coincidence from random trigger events are superimposed. The correlation is observed in time scale of about 200 μs, indicating that part (20%) of thermal neutron capture events can be matched to the thermalization of specific cosmic-ray events.

On the other hand, the detection efficiency of CR^+ system (λ) is measured $\sim$94% and the rejection efficiency of CR^- system (ε) is about $\sim$95%. The efficiency correction for CR system has done as explained in Section 4.3.1.

6.3 Internal Contamination of HND

The desired background channel under the tag $CR^- \otimes AC^-$ provide the internal background of the detector with the ambient neutron background together, which channel is the neutrino and WIMP candidate channel for HPGe. The ambient neutron background is emerged in this channel due to neutron insensitive AC detector. Therefore, intrinsic radiopurity of the HND should be determine to differentiate internal and neutron background. The photon background sources from the ^{238}U and ^{232}Th as explained in Section 1.1.1 is also significant source for α background. This could be negligible for HPGe detector but the impurity of the HND is not good as its. Also alpha particles and neutrons cannot be differentiate by PSD method. However, the event rate and the contamination level of uranium and thorium isotopes can be determined via time variation of specific channels. Once the determined one or two channel, the event rate can be calculate due to equilibrium of decay chain.

In this study, double pulse events was observed as displayed in Figure 6.6(a) and their time variation between two pulse was measured. The first pulse in this sample matches with β^-/γ band and second one is fit with neutron band, which means that, it is the candidate α event. Therefore, from the assumption, the reference of αs has collected from second pulse from this β^-–α decay sequence and illustrated all event pulses in Figure 6.6(b). The α and neutron pulse shape quite similar and there was not observed a significant discrimination by PSD method for α events in this study.

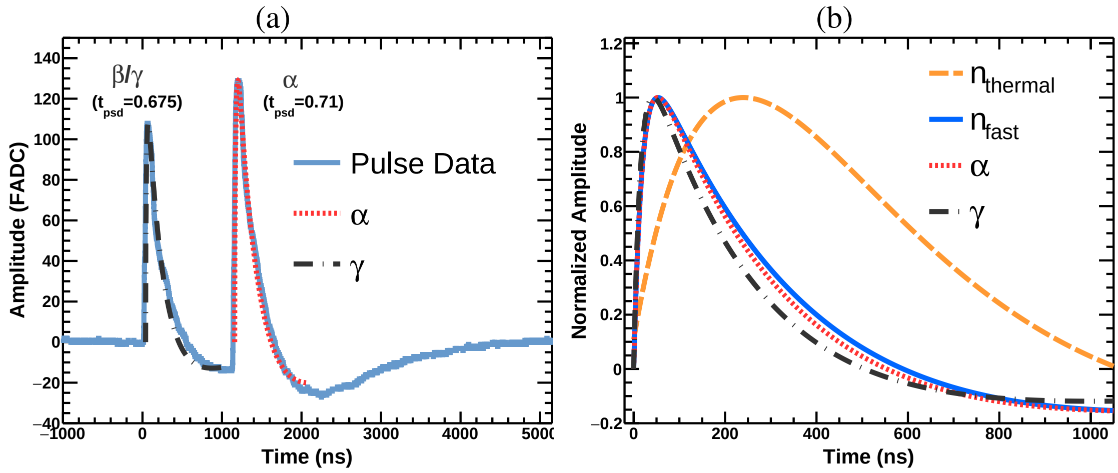

Figure 6.6 (a) The double pulse event sample, first pulse is an electron event and second pulse is and α event. The α reference is collected from those second pulses as demonstrated in (b). (b) Reference pulses of HND from various events

On the other hand, the time difference distribution between the two pulse is illustrated in Figure 6.7(a) and its consistency is observed as a sequence of ^{232}Th as β–α decay. Therefore the assumption is confirmed which claim the second pulse is an alpha event. As depicted of ^{238}U decay chain in Figure 1.1, the most traceable decay sequence is the α–α cascade from the ^{222}Rn to ^{214}Pb due to short half-life of ^{218}Po. Therefore, the specific condition can be determine in time and energy scale to obtain the time variation of this cascade as illustrated in Figure 6.7(b). As a consequence, the measured half-lives from both time variations was lead to description of two decay sequence from independent sources as following,

DS$_1$ Within the ^{232}Th series, there is 64% branching ratio for ^{212}Bi to decay via a β-α cascade –

$$
\begin{aligned}
^{212}\mathrm{Bi} &\rightarrow {}^{212}\mathrm{Po} + \bar{\nu}_e + e^- + \gamma' s \; (\mathrm{Q} = 2.25 \text{ MeV} \; ; \; \tau_{1/2} = 60.6 \text{ min}) \\
^{212}\mathrm{Po} &\rightarrow {}^{208}\mathrm{Pb} + \alpha \; (\mathrm{Q} = 8.95 \text{ MeV} \; ; \; \tau_{1/2} = 0.30 \; \mu\mathrm{s})
\end{aligned}
$$

DS$_2$ Within the ^{238}U series is the α-α cascade from ^{222}Rn –

$$
\begin{aligned}
{}^{222}\mathrm{Rn} &\rightarrow {}^{218}\mathrm{Po} + \alpha \; (\mathrm{Q} = 5.59 \text{ MeV} \; ; \; \tau_{1/2} = 3.82 \text{ d}) \\
{}^{218}\mathrm{Po} &\rightarrow {}^{214}\mathrm{Pb} + \alpha \; (\mathrm{Q} = 6.12 \text{ MeV} \; ; \; \tau_{1/2} = 3.10 \text{ min})
\end{aligned}
$$

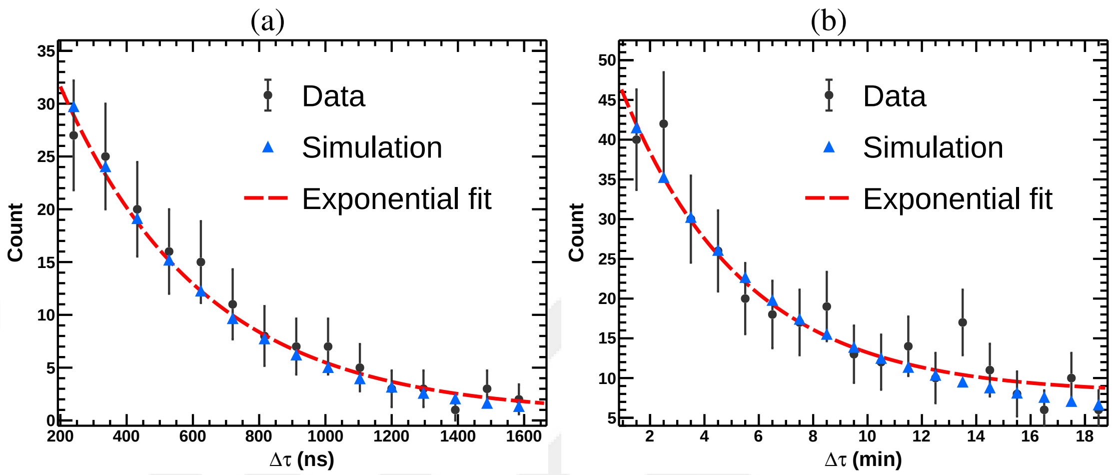

Figure 6.7 Time variations distribution for (a) β–α events from DS$_1$, (b) α–α events from DS$_2$

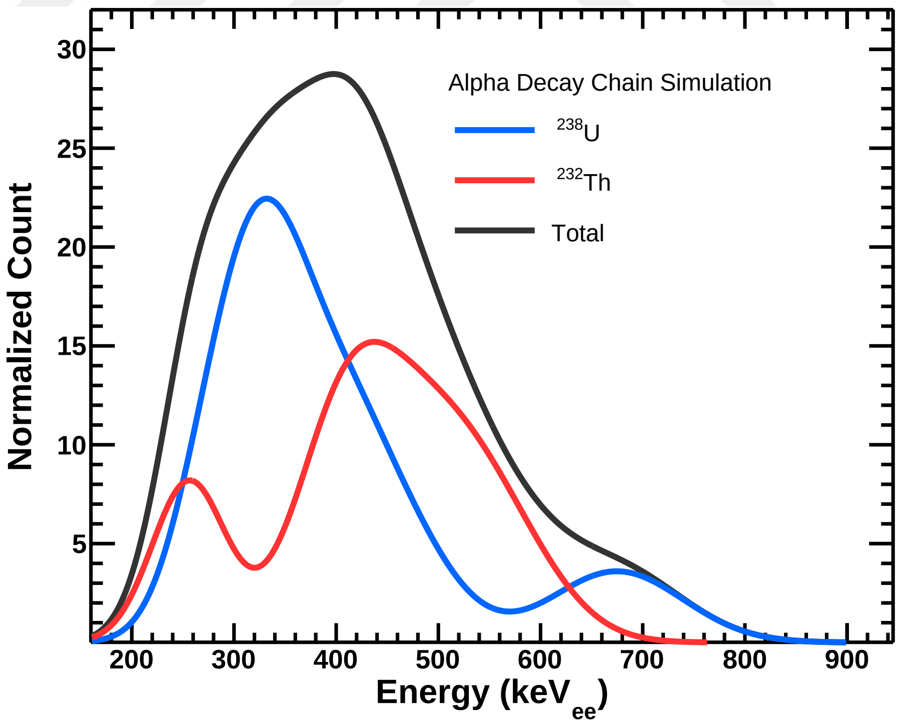

Figure 6.8 Simulated α energy spectrum of ^{232}Th and ^{238}U decay chains normalized by measured activity for DS$_1$ and DS$_2$ signature in Table 6.3, respectively

The event rate of the mother isotopes are measured by best fit of their simulation

Table 6.3 Summary of measured values and inferred radioactivity levels of the two cascade sequences

Series	DS_1 ^{232}Th	DS_2 ^{238}U
Signatures	β-α	α-α
Decays	^{212}Bi $\rightarrow^{212}$ Po $\rightarrow^{208}$ Pb	^{222}Rn $\rightarrow^{218}$ Po $\rightarrow^{214}$ Pb
χ^2/n.d.f	4.7/16	9.0/17
Half-Life		
Nominal	299 ns	3.10 min
Measured	302$\pm$27 ns	3.14$\pm$0.39 min
Counts in 33.8 day	366.20$\pm$26.94	292.50$\pm$15.43
Radioactivity (mBq/kg)	0.140 $\pm$ 0.010	0.110 $\pm$ 0.006
Contaminations $\times 10^{-11}$(g/g)	2.21 $\pm$ 0.16	0.89 $\pm$ 0.048

inside the HND for taking into account of efficiency effects as illustrated in Figure 6.7. Thus, the measured event rates, half-lives and contamination levels etc. are summarized in Table 6.3.

The α energy spectrum from simulation prediction is obtained by Geant4 tool as illustrated in Figure 6.8. The quenching effect by Equation 5.9 with given parameters in Table 5.1 and detector resolution are applied in to simulated spectrum as described previous chapter. This spectrum was subtracted from $CR^- \otimes AC^-$ recoil spectrum by scaling with the measured table as demonstrated in Table 6.3 to obtain ambient neutron background. All the contamination was observed only in $CR^- \otimes AC^-$ channel.

6.4 Thermal Neutron Flux

Thermal neutrons energy distribution is described by the Maxwell-Boltzmann distribution which are those with kinetic energy below 1 eV and in thermal equilibrium. The most probable energy of the thermal neutron is ~0.02 eV, which correspond to velocity of v_{th} ~2200 ms^{-1}. The BC-702 scintillator is efficient for those neutrons as illustrated in Figure 5.3(c) in previous section. The scintillator does not provide the energy information, therefore, calculation of the thermal neutron flux was performed by assuming Maxwell-Boltzmann distributions.

The count rate in the detector, for a neutron flux $\phi_n(E)$ with interaction cross section $\sigma(E)$ is given by

$$R_{th} = N \int \sigma(E)\phi_n(E)dE \ , \tag{6.1}$$

where N is the total number of target nuclei in the detector. It is known that, the thermal neutron capture by ^{6}Li cross section is proportional to the inverse of the neutron velocity v_{th} (Hughes, 1957) and it can be written as

$$\sigma(E) = \sigma_{th}\frac{v_{th}}{v(E)} \ , \tag{6.2}$$

where v_{th} is a neutron velocity at which reaction cross-section σ_{th} is known as 940 barn. Moreover, for an isotropic and homogeneous distribution, flux can be describe as

$$\phi(E) = v(E)\rho_n(E) \tag{6.3}$$

where $\rho_n(E)$ is the density of neutrons in the detector volume and the count rate is written in terms of total number of the neutrons in the volume as

$$R_{th} = N\sigma_{th}v_{th}\langle\rho_n\rangle \ . \tag{6.4}$$

Considering the average neutron velocity ($\langle\rho_n\rangle$) and the total flux (Φ)

$$\langle v\rangle = \frac{\int v(E)\rho_n(E)dE}{\int \rho_n(E)dE} = \frac{\Phi}{\langle\rho_n\rangle} \ . \tag{6.5}$$

Accordingly, the rate becomes

$$R_{th} = N\sigma_{th}\frac{v_{th}}{\langle v\rangle}\Phi \ . \tag{6.6}$$

Maxwell-Boltzmann distribution for thermal neutrons provides the averaged velocity as

$$\langle v\rangle = \frac{2v_{th}}{\sqrt{\pi}} \ . \tag{6.7}$$

Accordingly the total thermal neutron flux for measured rate and lithium cross section is related with given equation,

$$\Phi_n = \frac{2R_{th}}{N\sigma_{th}\sqrt{\pi}} \ . \tag{6.8}$$

The measured total thermal neutron rate in the KSNL by BC-702 scintillator is

$$R_{th} = (4.15 \pm 0.12)\ \times\ 10^{-4}\ count\ s^{-1} \ . \tag{6.9}$$

The corresponding total thermal neutron flux with a total number of $N = 1.41\ \times\ 10^{22}$ ^{6}Li atoms in the BC-702 scintillator is,

$$\Phi_n = (3.54 \pm 0.10)\ \times\ 10^{-5}\ cm^{-2}\ s^{-1} \ . \tag{6.10}$$

The given rate in Equation 6.10 is corresponding to total thermal neutron count in the KSNL in 33.8 day. The summary of thermal neutron flux measurements are given in Table 6.4

Table 6.4 Summary of thermal neutron flux measurements among the channels

Thermal Neutrons 0.001 eV – 1.00 eV	Measured Fluxes Φ_n (cm^{-2}s^{-1})
$CR^+ \otimes AC^-$	$(2.68 \pm 0.28) \times 10^{-6}$
$CR^+ \otimes AC^+$	$(3.00 \pm 0.29) \times 10^{-6}$
$CR^- \otimes AC^+$	$(9.33 \pm 1.65) \times 10^{-7}$
$CR^- \otimes AC^-$	$(2.87 \pm 0.09) \times 10^{-5}$

6.5 Fast Neutron Flux and Projected HPGe Background

Once the folded spectra are measured, unfolded algorithm as discussed in Section 5.3, followed by a Friedman smoothing algorithm (Friedman, 1984), are applied to produce the corresponding fast neutron spectra.

The measured folded spectra with reconstruction of itself by corresponding fast neutron spectra, and the measured α–background contamination for $CR^- \otimes AC^-$ channel as discussed in Section 6.3 are illustrated in Figure 6.9. The unfolded neutron fluxes was converted into the expected nuclear recoil background in HPGe, which is measured with same place and shielding configuration. Both neutron fluxes and corresponding neutron background in HPGe are shown in Figures 6.10, 6.11, 6.12, 6.13. On the other hand the corresponding threshold of neutron flux for the best discrimination at 150 keV$_{ee}$ as discussed in Section 5.2.1, has measured as 700 keV. Therefore an extrapolation was used to make a bridge among the threshold with slow neutrons by wide range Gaussian function, which is cover the fast neutron spectrum shape and has a mean point at 1 MeV. Moreover, on the construction of neutron flux, 20 keV bin size response matrix was used thus the first point of neutron fluxes as illustrated in Figure 6.10 and 6.11 (b), are satisfy by total of the thermal neutron flux as given in Table 6.4 with the epithermal neutron flux as will be explained in Section 6.6.

Result of predicted nuclear recoil backgrounds for measured neutron flux with

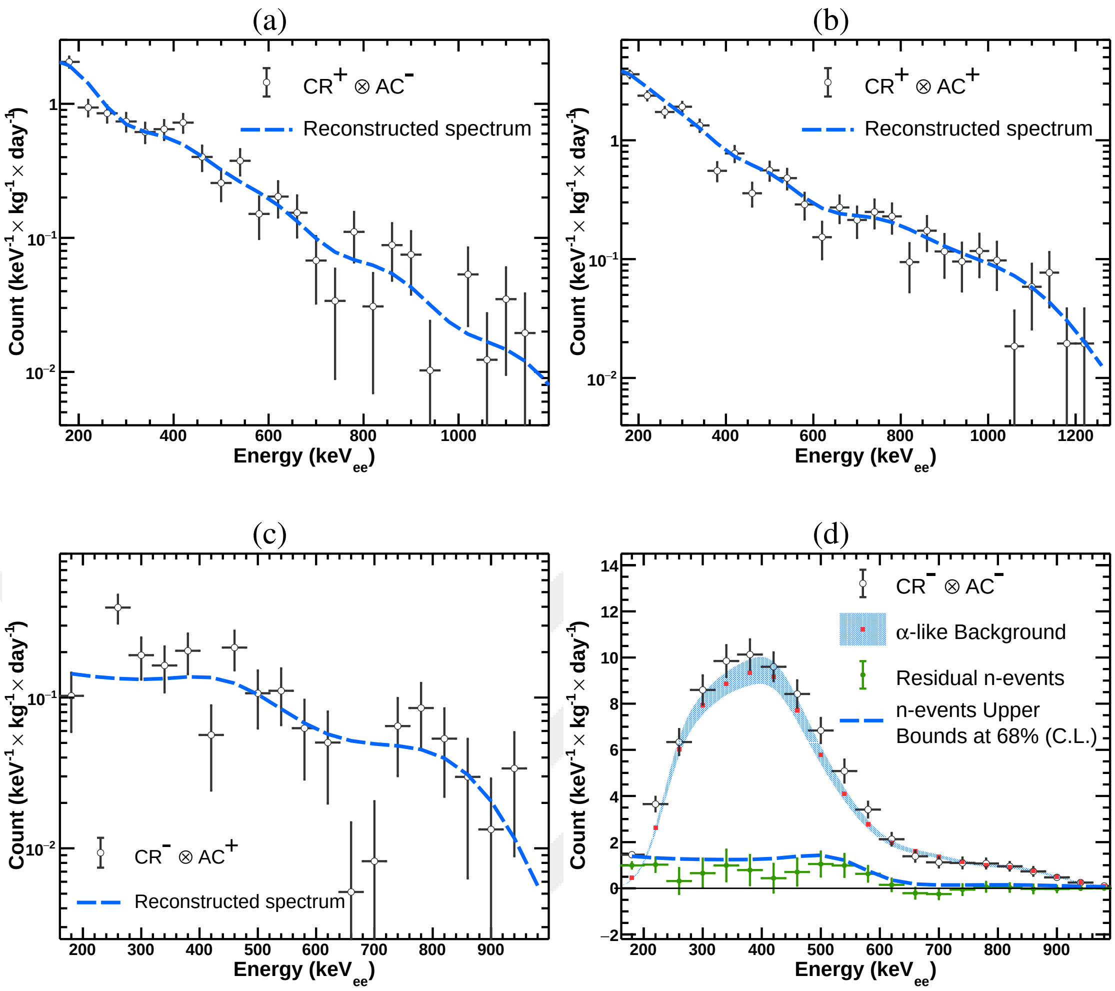

Figure 6.9 The samples of HND nuclear recoil energy spectrum for, (a) CR^{+} $\otimes$ AC^{-}, (b) CR^{+} $\otimes$ AC^{+}, (c) CR^{-} $\otimes$ AC^{+} and (d) CR^{-} $\otimes$ AC^{-} energy spectra for HND nuclear recoil-like events, together with the measured $\alpha-$ background from ^{232}Th and ^{238}U decay series as illustrated and scaled in Figure 6.8, and the 68% C.L. upper bound of neutron-induced nuclear recoils. The blue dashed lines represent reconstructed folded spectra from the unfolded neutron flux

HPGe samples are illustrated for relative channels in Figures 6.10, 6.11, 6.12, 6.13 (b). The extrapolation below the observed threshold at 700 keV is effected below 4 keV$_{ee}$ on CR^{+} $\otimes$ AC^{-} and CR^{+} $\otimes$ AC^{+} samples. The sample of CR^{+} $\otimes$ AC^{-} is expected cosmic induced neutron dominant channel and it is satisfied by 99% due to combination of projected Ge-recoil spectrum with extrapolation.

The CR^{+} $\otimes$ AC^{+} sample is the expected channel both neutron and Compton scattering of high energy γ-rays due to cosmic induced events. Those γ-rays events are

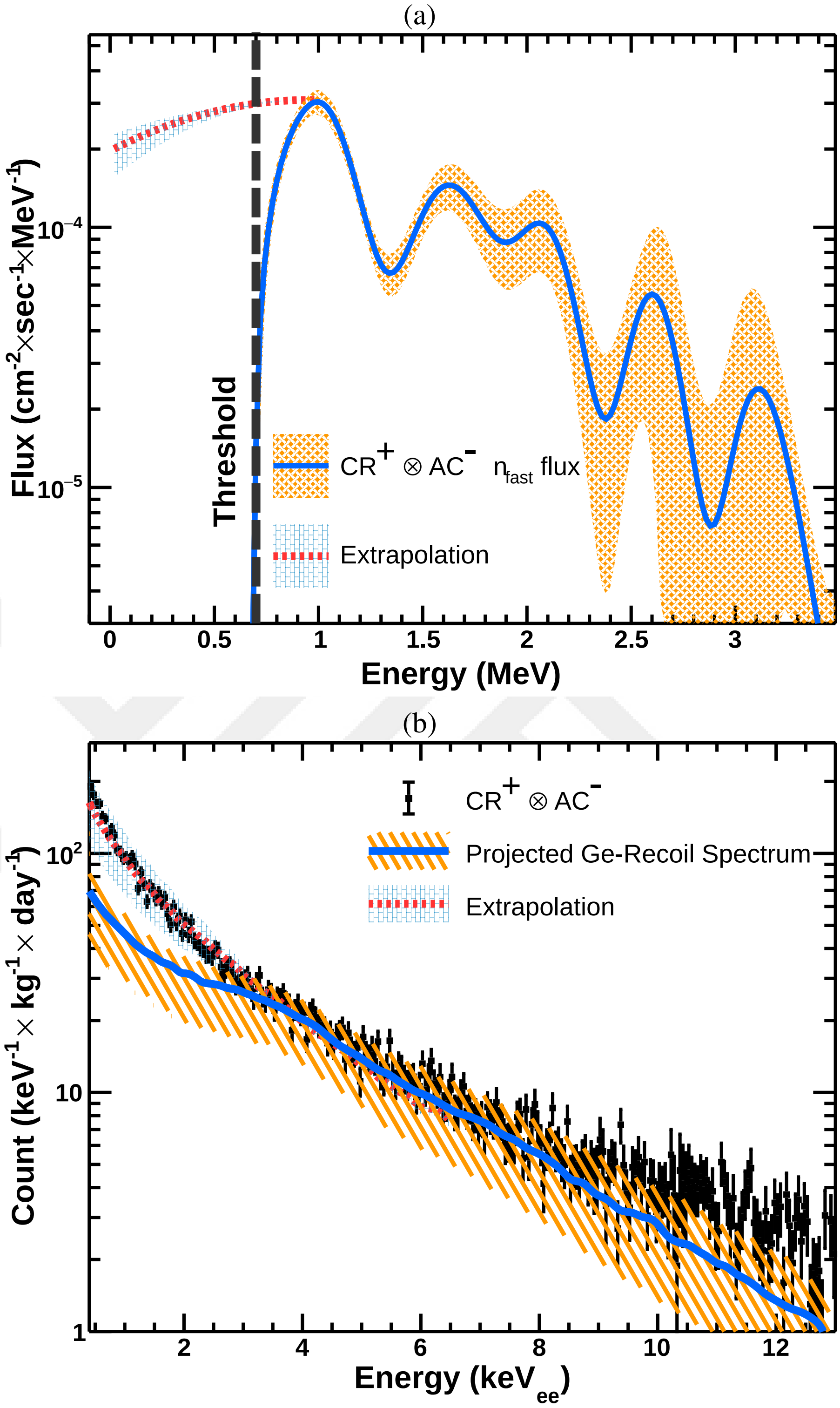

Figure 6.10 The sample of $CR^+ \otimes AC^-$ – (a) unfolded neutron flux with $\pm 1\sigma$ error as shadowed area, (b) the comparison of HPGe data and predicted Ge-recoil spectrum from simulations with the measured neutron fluxes. Extrapolated spectra of (a) and (b) at low energy, as fixed by neutron flux models of Figure 6.14 derived from equilibrium yield of $^{70}Ge(n,\gamma)^{71}Ge$, are corrections to the effects due to finite HND threshold of 150 keV_{ee}

(a)

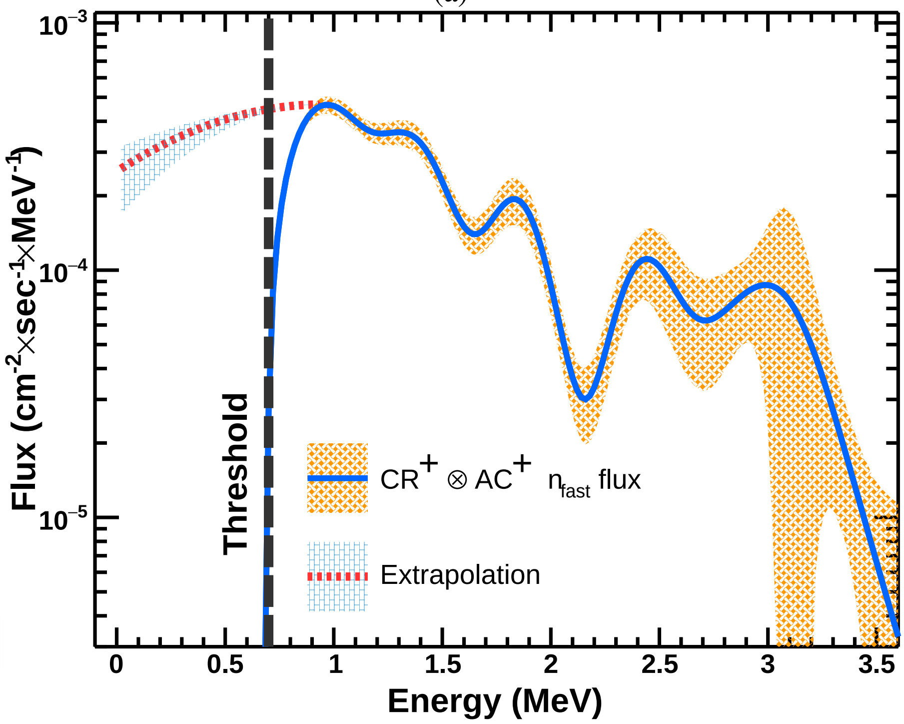

(b)

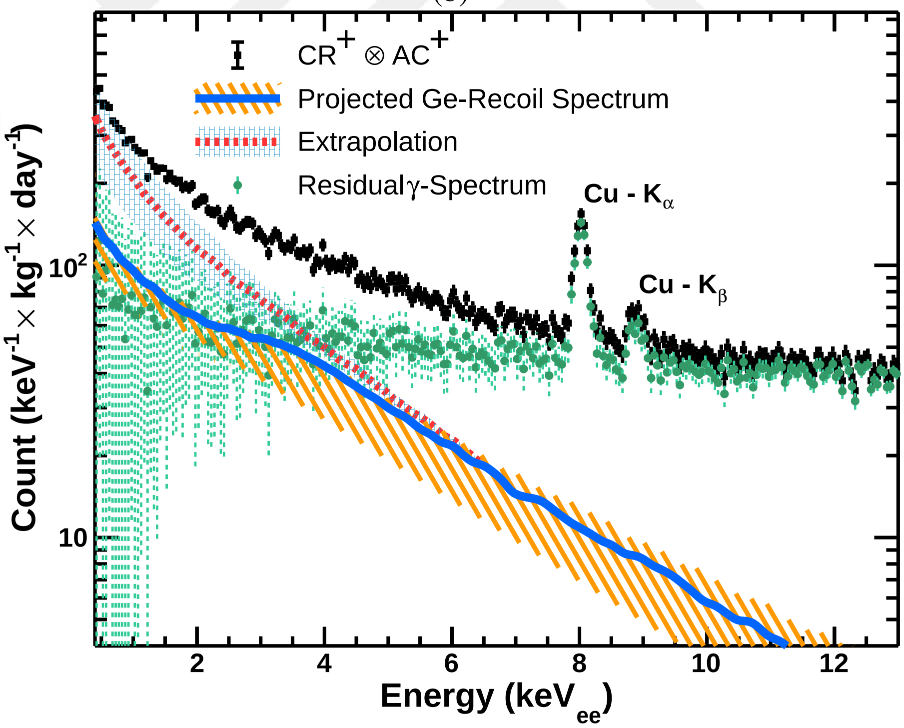

Figure 6.11 The sample of CR^{+} $\otimes$ AC^{+} – (a) unfolded neutron flux with $\pm 1\sigma$ error as shadowed area, (b) the comparison of HPGe data and predicted Ge-recoil spectrum from simulations with the measured neutron fluxes. Extrapolated spectra of (a) and (b) at low energy, as fixed by neutron flux models of Figure 6.14 derived from equilibrium yield of ^{70}Ge(n,γ)^{71}Ge, are corrections to the effects due to finite HND threshold of 150 keV$_{ee}$

(a)

(b)

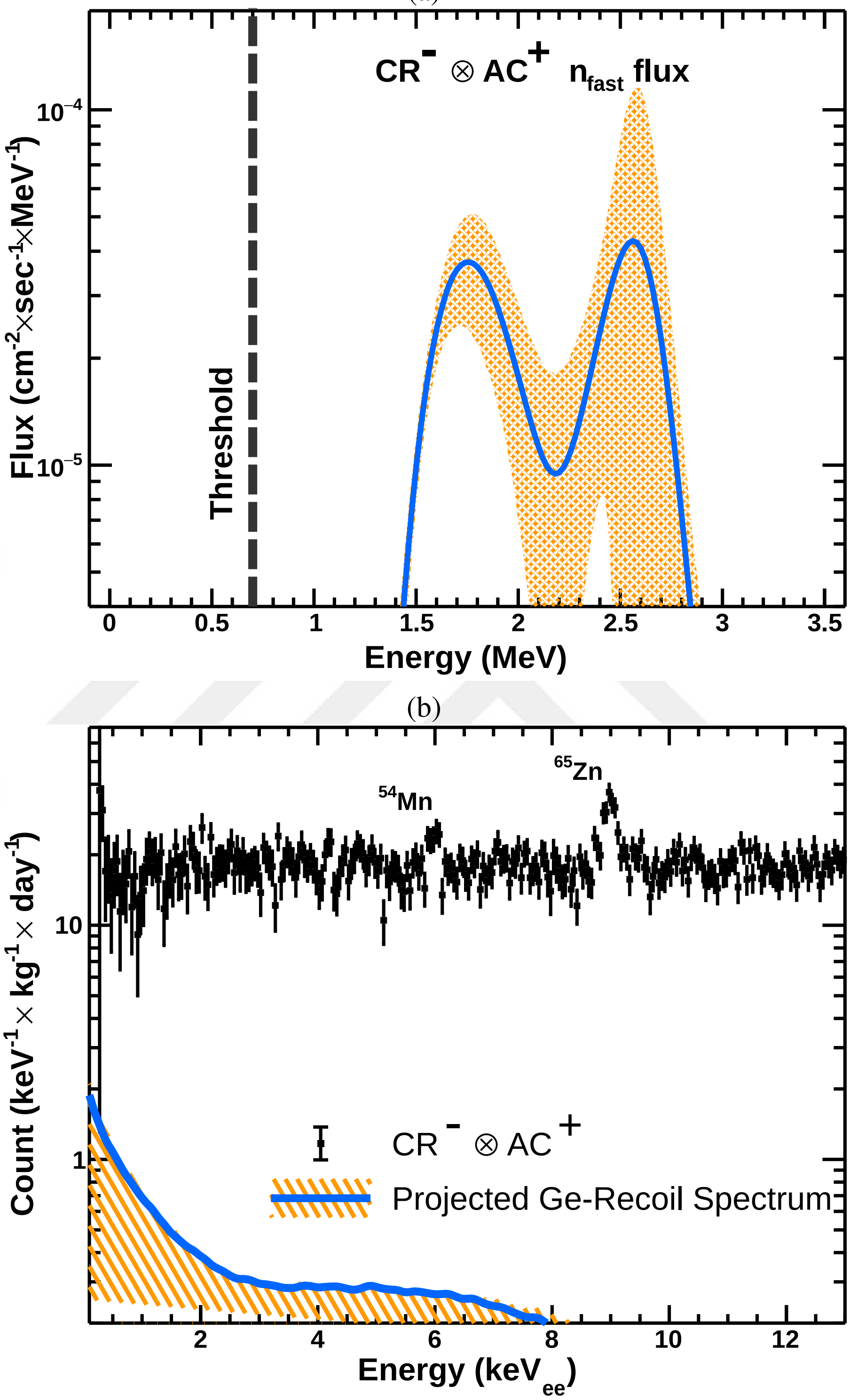

Figure 6.12 The sample of CR$^-$ $\otimes$ AC$^+$ – (a) unfolded neutron flux with $\pm1\sigma$ error as shadowed area, (b) the comparison of HPGe data and predicted Ge-recoil spectrum from simulations with the measured neutron fluxes

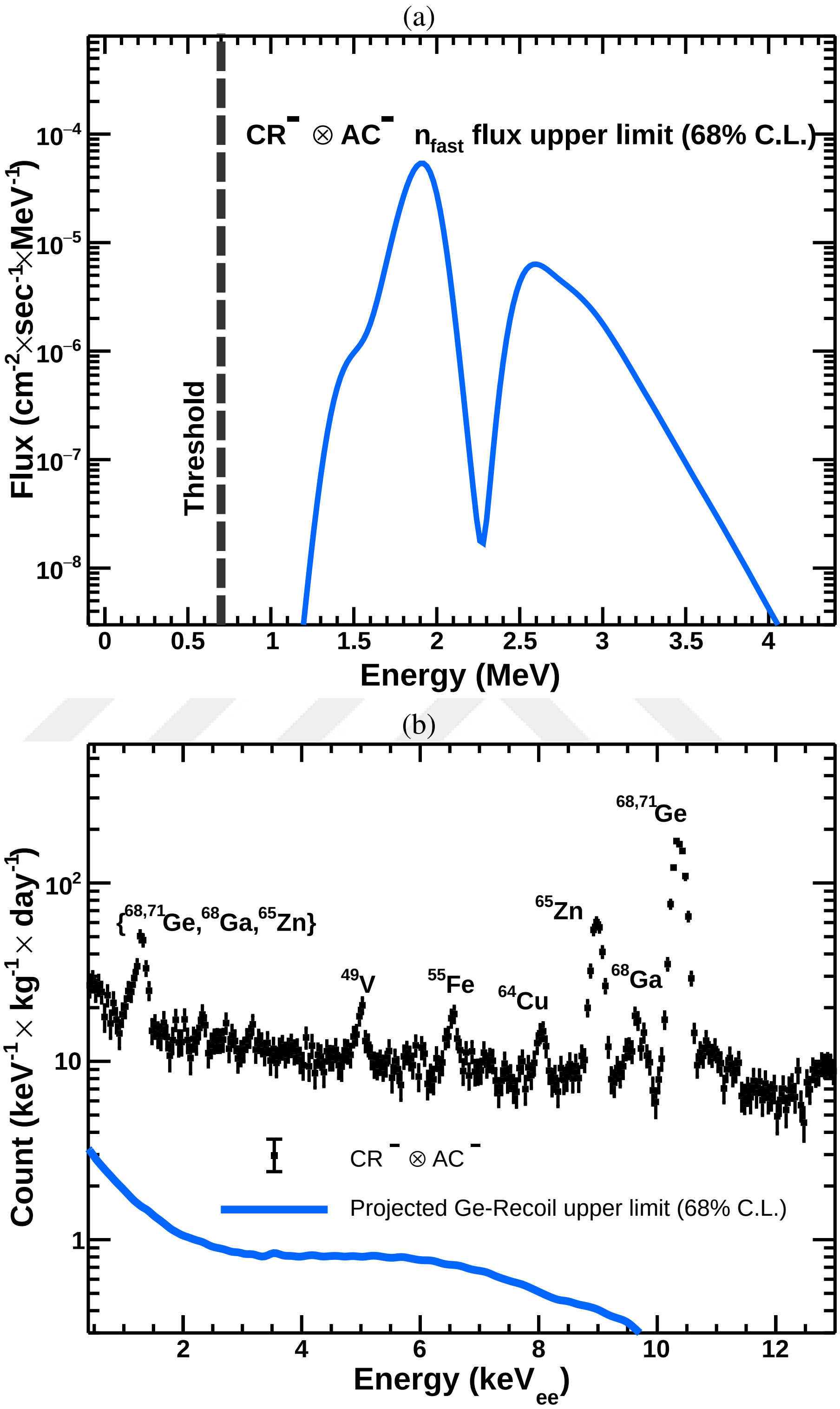

Figure 6.13 The sample of $CR^{-} \otimes AC^{-}$ – from which the upper bounds of (a) unfolded neutron spectrum and (b) predicted Ge-recoil background in HPGe can be derived and compared with measured data

characterized by flat spectrum. As being in the $CR^+ \otimes AC^-$ sample, combination of the extrapolation and projected Ge-recoil spectrum and the consistent residual events are satisfied with this flat spectrum behavior. The two peaks corresponds to copper K_α and K_β X-ray emission lines which are produced by the interactions of cosmic-ray muons with the supportive copper materials in the vicinity of the active Ge crystal.

The neutron background component on the cosmic-ray anti-coincidence samples with $CR^- \otimes AC^+$ and $CR^- \otimes AC^-$ tags have a minor contribution relative to that due to ambient γ-radioactivity. The measured "recoil-like" spectrum for $CR^- \otimes AC^-$ tag can completely be explained by internal α-contamination as discussed in Section 6.3. Therefore, upper limits of this spectra at 68% C.L. are displayed as being in Figure 6.13. The peaks are due to X-rays emissions following electron capture (EC) by the long-lived unstable isotopes in HPGe spectrum, which are produced by cosmogenic activation.

6.6 Complete Neutron Spectrum

As discussed in Section 6.1, the cosmic-ray shower is causes to produces the some long-lived cosmogenic activated isotopes internally in HPGe. Therefore this isotopes projects to internal background due to their long-lived case. Furthermore they are continuum to be produced dominantly by neutrons and causes an equilibrium yield continuously which is shown in Table 6.2. This equilibrium level have to be consistent with related ^{x}Ge production by measured total neutron fluxes in situ. It is observed that in Section 6.1, this long-lived isotope production occurs by only neutron capture of ^{70}Ge by following reaction, ^{70}Ge(n,γ)^{71}Ge, in situ. Therefore, with the combining of measured fast and thermal neutron fluxes and spectra, and adopting the neutron slowing-down theory (Lamarsh, 1966; Oka, 2010), which is described by a 1/E behavior of the epithermal region in between, the complete neutron spectrum at KSNL can be modeled using information in the Table 6.2. The different type of neutron rate for ^{70}Ge neutron capture in HPGe and the corresponding simulated efficiencies with the neutron capture rate are shown in Table 6.5.

Table 6.5 Summary of the total neutron rates for neutron capture interaction of ^{70}Ge in HPGe with the corresponding neutron capture rates

Channel	Measured Neutron Rate $(kg^{-1} \times day^{-1})$	Simulated Efficiency (%)	Neutron Capture Rate $(kg^{-1} \times day^{-1})$
$n_{thermal}$	$(1.42 \pm 0.04) \times 10^2$	5.67	8.05 ± 0.23
$n_{epithermal}$	$(2.53 \pm 0.77) \times 10^3$	0.86	2.18 ± 0.67
n_{fast}	$(2.76 \pm 1.12) \times 10^3$	0.13	3.67 ± 1.50
total	$(3.15 \pm 1.12) \times 10^3$	–	13.90 ± 1.65

As a consequence, complete neutron spectrum can be generated by considering total fluxes as is illustrated in Figure 6.14.

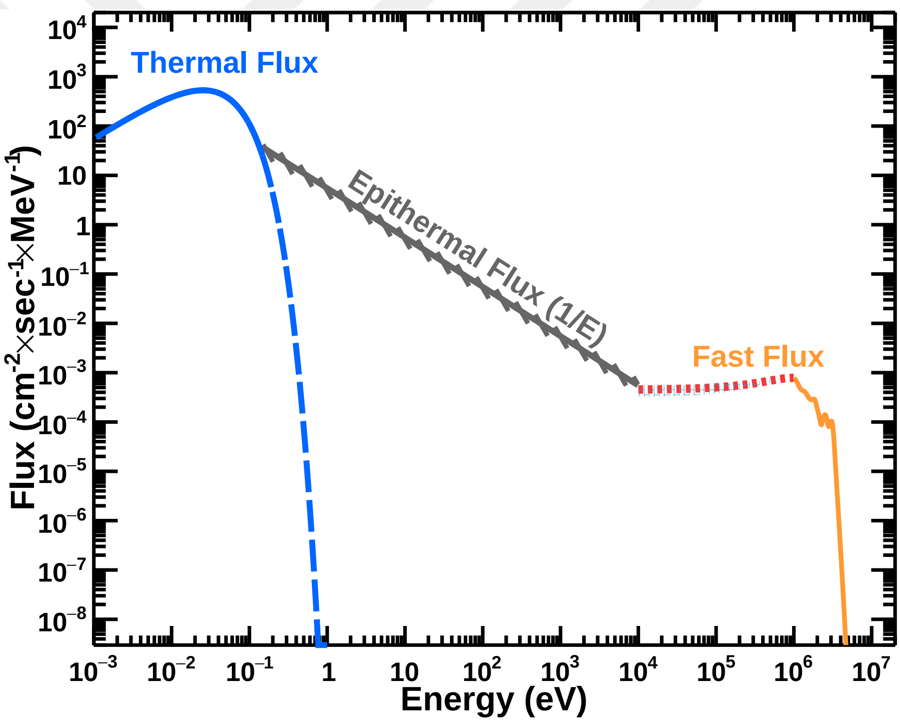

Figure 6.14 Neutron spectrum model at the target region of KSNL. The total thermal and fast neutron components are based on measurements and analysis reported in this study. The epithermal component is from interpolation

Complete neutron spectrum modeling by considering the measurement of cosmogenic activated isotopes in germanium, has taken into account for simulating Ge-recoil results, especially for cosmic channel.

For ambient neutron background in germanium results, fast neutrons do not affect to physics candidate signals. On the other hand, obtained limit in $CR^{-} \otimes AC^{-}$ Ge-recoil spectra can be used for different physics interaction which has event rate below one cpkd. Thus, this study provides a limit for neutron background contribution into Ge-recoil spectra in purpose of using in SM and BSM interactions of neutrinos and WIMP at lower energy, *in situ*.

CHAPTER SEVEN
CONCLUSIONS

In this study, a special designed detection system for background suppression has been introduced in the purpose of investigation of neutrino and WIMP interactions. The three important interactions of neutrino have been reviewed and demonstrated with their published out come for $\nu - e$ elastic scattering in the SM, electromagnetic properties of $\bar{\nu}_e$ and coherent elastic neutrino-nucleus scattering interactions. These three important processes were summarized by their differential event rate behavior in Figure 2.8 for known reactor $\bar{\nu}_e$ as was illustrated in Figure 2.2. For the investigation of the SM interaction of $\bar{\nu}_e - e$ elastic scattering, CsI(Tl) crystal array detector was used as was illustrated in Figure 2.9 and measurement showed consistency of SM by $R_{expt}(\nu)/R_{SM}(\nu) = 1.08 \pm 0.21(stat) \pm 0.16(sys)$. On the other hand, interference term was measured "-1" by using η parameter as is assumed by the SM. Another important measurable parameter, weak mixing angle for the SM, was measured as $sin^2\theta_W = 0.251 \pm 0.031(stat) \pm 0.024(sys)$. The PDG result demonstrates that constraining three experimental results in g_A vs. g_V space provides the best value for weak mixing angle as was illustrated in Figure 2.11. Another important issue in neutrino physics is the neutrino magnetic moment properties. In the SM, neutrinos are massless and their magnetic momenta are zero. However, the interaction of neutrino with a photon as a mediator particle can be investigated by unknown physics vertex for BSM interaction. This measurement for Ge target was illustrated in Figure 2.12 and neutrino magnetic moment limit was given as $\mu_{\bar{\nu}_e} < 7.4 \times 10^{-11}\ \mu_B$. The current experiment aim is to achieve low energy and low background for CENNS and WIMP candidate signal by using germanium target. This germanium target was used as a main detector for neutrino and WIMP candidate signal detection. At the low energy, neutron source becomes quite important due to low recoil energy of the large atomic number of the nuclei. Therefore, the contribution of neutrons on the germanium background must be understood. For this reason, the neutron contribution on Ge-recoil spectrum was measured by using a hybrid structure detector with a combination of organic liquid scintillator and ZnS(Ag) phosphor powder for fast and slow neutron detection *in situ*.

In chapter 3, experimental detail for the background suppression was presented and the detection system of typical germanium detectors was shown. Some notation have been also introduced for active shield labeling as coincidence(anticoincidence) cases of the cosmic ray (CR) and anti-Compton (AC) systems. In the chapter following 3, the characterization of different kinds of HPGes and their integration in the KSNL with full analyses details were reported. After performing all the required analysis steps, neutrino and WIMP candidate spectra were shown in Figure 4.9 as $CR^- \otimes AC^-$.

In chapter 5, full characterization of hybrid neutron detector and Monte Carlo simulation consistency was reported. In this small detector, neutrons deposit some of their energy into nuclei and leave the detector. This recoil energy is affected by quenching factor, with which the measured LO is associated. Due to all these reasons, a numerical method was developed in this study to find the initial energy of neutron, which is known as unfolding method. This method requires response matrix as a monochromatic neutron LO spectra which were created by Geant4 tool. The method was compared for known sources ^{22}Na, ^{137}Cs, ^{60}Co and ^{241}AmBe(α,n) and successful match was observed as was illustrated in Figures 5.14 and 5.16.

Subsequently, adaptation of HND into KSNL was reported in chapter 6. In that chapter some challenges were realized; namely, the introduced physics channel $CR^- \otimes AC^-$ considered as internal channel. Hence then, internal contamination appeared in this channel and α events looked literally similar to neutrons. Specific decay sequences were observed from uranium and thorium decay chain and α-like spectrum was created via Geant4 tool by measuring their decay rate. On the other hand, thermal neutron flux *in situ* was reported by the calculation from the count rate. For fast neutrons, the results for the cosmic-related events sign that the cosmic coincidence background events under the $CR^+ \otimes AC^-$ tag dominate in the range of 0-12 keV$_{ee}$ as was expected. The result of the other cosmic background channel with $CR^+ \otimes AC^+$ tag showed that the flat spectrum of γ-ray background and the cosmegenic neutron background are two components of this channel. On the other hand, for ambient events under the $CR^- \otimes AC^+$ and $CR^- \otimes AC^-$ tags with the Compton coincidence and anti-coincidence background there is a minor contribution of Ge-recoil background due to neutrons. As a result, the events on $CR^- \otimes AC^+$ are mostly dominated by Compton background of ambient photons as was expected. The Ge-recoil contribution due to neutron interaction on internal background for neutrino and WIMP candidate events on $CR^- \otimes AC^-$ is negligible. The neutron fluxes of each background channel from the different energy region of neutrons are summarized in Table 7.1.

Table 7.1 Summary of flux measurements of different categories of neutrons

Neutrons	Measured Fluxes Φ_n ($cm^{-2}s^{-1}$)
Thermal – 0.001 eV – 1.00 eV	
$CR^+ \otimes AC^-$	$(2.68 \pm 0.28) \times 10^{-6}$
$CR^+ \otimes AC^+$	$(3.00 \pm 0.29) \times 10^{-6}$
$CR^- \otimes AC^+$	$(9.33 \pm 1.65) \times 10^{-7}$
$CR^- \otimes AC^-$	$(2.87 \pm 0.09) \times 10^{-5}$
Epithermal	$\left\{ \begin{array}{l} > 4.39 \times 10^{-5} \\ < 8.25 \times 10^{-5} \end{array} \right.$
Fast – 0.70 MeV – 4.00 MeV	
$CR^+ \otimes AC^-$	$(2.35 \pm 1.60) \times 10^{-4}$
$CR^+ \otimes AC^+$	$(4.53 \pm 2.29) \times 10^{-4}$
$CR^- \otimes AC^+$	$(1.49 \pm 5.75) \times 10^{-6}$
$CR^- \otimes AC^-$	$< 3.22 \times 10^{-6}$

Another consequence of this study is to create a complete neutron spectrum by using the measured neutron capture rate of germanium isotopes. Some long-lived unstable isotopes as a product of neutron interaction have been achieved in an equilibrium yield. So, the complete neutron spectrum has to satisfy this equilibrium yield as is expected. Therefore, the consistence can be compared between these two independent measurements. Such a motivation helped to model a complete neutron spectrum as in this study, after which it was understood that the neutron capture rate can be studied by prediction of neutron contribution of rare event searches on low energy and low background studies.

REFERENCES

Aalseth, C. E. et al., (2011). Results from a Search for Light-Mass Dark Matter with a P-type Point Contact Germanium Detector, *Phys. Rev. Lett. 106*, 131301 110

Adams, J. M. et al, (1978). A versatile pulse shape discriminator for charged particle separation and its application to fast neutron time-of-flight spectroscopy, *Nucl. Instr. and Meth. A 156*, 459-476

Agnese, R. et al., (2016). New Results from the Search for Low-Mass Weakly Interacting Massive Particles with the CDMS Low Ionization Threshold Experiment, *Phys. Rev. Lett. 116*, 071301

Agostinelli, S., (2003). GEANT4: A Simulation toolkit, *Nucl.Instrum.Meth. A506* 250-303

Barbeau, P. S. et al., (2007). Large-mass ultra-low noise germanium detectors: performance and applications in neutrino and astroparticle physics, *J. Cosm. Astro. Phys. 0709*, 9.

Barranco, J. & Miranda, O. G., (2002) Sensitivity of low energy neutrino experiments to physics beyond the standard model. *Phys. Rev. D 76*, 073008

Barr, S. M. (1990). Mechanism for Large Neutrino Magnetic Moments. *Phys. Rev. Lett. 65*, 2626

Billard, J. et al, (2013). Implication of neutrino backgrounds on the reach of next generation dark matter direct detection experiments. *Phys. Rev. D 89*, 023524

Birks, J.B. (1951). Scintillations from Organic Crystals: Specific Fluorescence and Relative Response to Different Radiations., *Proc. Phys. Soc. A64.* 874.

Birks, J. B., (1964). *The theory and practice of scintillation counting*, Pergamon Press

Brun, R. and Rademakers, F., (1997). ROOT - An Object Oriented Data Analysis Framework, Proceedings AIHENP'96 Workshop, Lausanne, Sep. 1996, *Nucl. Inst. and Meth. in Phys. Res. A 389* 81-86.

Cecil, R. A. et al., (1979). Improved predections of neutron detection efficiency for hydrocarbon scintillators from 1 MeV to about 300 MeV, *Nucl. Inst. and Meth. A 161*, 439-447

Chou, C. N., (1952). The Nature of the Saturation Effect of Fluorescent Scintillators, *Phys. Rev. 87*, 904

Cooper, R. J. et al, (2011). A Pulse Shape Analysis technique for the MAJORANA experiment, *Nucl. Inst. Meth. A 629* 303-310.

Covington, L. et al, (2001). *SIMULATE-3 Ver 6.07.08, STUDSVIK/SOA-95/15 Rev. 2*, Studsvik Scandpower.

Czirr, J. B. et al., (1964). Calibration and performance of a neutron-time-of-flight detector, *Nucl. Inst. and Meth. A 31*, 226-232

Deniz, M., et al., (2010). Measurement of Nu(e)-bar -Electron Scattering Cross-Section with a CsI(Tl) Scintillating Crystal Array at the Kuo-Sheng Nuclear Power Reactor., *Phys.Rev. D81*, 072001.

Edenius, M. et al, (1994). *CASMO-3 Ver 4.84 STUDSVIK/ SOA-94/9*, Studsvik Scandpower.

Engel, J. (1991) Nuclear form factors for the scattering of weakly interacting massive particles. *Physics Letters B 264*, Issues 1–2, 114-119

Flaska, M. et al., (2007). Identification of shielded neutron sources with the liquid scintillator BC-501A using a digital pulse shape discrimination method, *Nucl. Instr. and Meth. A 577* 654-663

Freedman, D. Z. (1974) Coherent effects of a weak neutral current. *Phys. Rev. D 9*

Friedman, J. H., (1984). A Variable Span Smoother, Journal of American Statistical Association, *SLAC PUB-3477, STAN-LCS 005*

Fujikawa, K., Shrock, R. E., (1980). Magnetic Moment of a Massive Neutrino and Neutrino-Spin Rotation., *Phys. Rev. Lett. 45*, 963

Glimore, Gordon, (2008). *Practical Gamma-Ray Spectrometry: Second Edition*, Wiley, New York, U.S.A.,(ISBN: 9780470861967).

Griffiths, D. J., (2008). *Introduction to Elementary Particles. English. 2nd edition.*, Weinheim: Wiley-VCH.

Heusser, G., (1995). Low-Radioactivity Background Techniques, *Annu. Rev. Nucl. Part. Sci. 45*, 543.

Hughes, D.J., (1957). *International Series of Monographs on Nuclear Energy, Div. 2, 1: Neutron Cross Sections*, Pergamon Press.

Ivanovich, M. & Harmon, R. S., (1992). *Uranium Series Disequilibrium: Applications to Earth. Marine and Environmental Sciences.*, Oxford: Clarendon (1992).

Jones, K. W. & Kraner, H. W., (1971). Stopping of 1- to 1.8-keV ^{73}Ge Atoms in Germanium, *Phys. Rev. C 4*, 125

Jones, K. W. & Kraner, H. W., (1975). Energy lost to ionization by 254-eV ^{73}Ge atoms stopping in Ge, *Phys. Rev. A 11*, 1347

Kalyna, J. et al., (1970). Pulse shape discrimination: An investigation of n-γ discrimination with respect to size of liquid scintillator, *Nucl. Instr. and Meth. A 88-2* 277-287

Klein, H. and Neumann, S., (2002). Neutron and photon spectrometry with liquid scintillation detectors in mixed fields, *Nucl. Inst. and Meth. A 476*, 132-142.

Kluge, H. and Weise, K., (1982). The Neutron Energy Spectrum of a ^{241}Am-Be(Alpha,n) Source and Resulting Mean Fluence to Dose Equivalent Conversion

Factors, *Radiation Protection Dosimetry, 2*, 85-93.

Knoll, G. F., (1989). *Radiation Detection and Measurement*, Wiley, New York, U.S.A.,(ISBN: 9780471815044).

Knoll, G., *Radiation Detection and Measurements*, 3rd Edition, Wiley, New York, 2000.

Knox, H. H. & Miller, T. G., (1972). A technique for determining bias settings for organic scintillators, *Nucl. Inst. and Meth. A* 101 519-525

Kuo, W. S., (2001). *FISSRATE Ver 2.0, 08-4-MAN-036-002-1.0*, Institute of Nuclear Energy Research.

Lamarsh, J.R., (1966). *Introduction to Nuclear Reactor Theory*, Addison-Wesley

Li, H. B. et al., (2014). Differentiation of bulk and surface events in p-type point-contact germanium detectors for light WIMP searches, *Astroparticle Physics 56*, 1.

Lindhard, J. et al., (1963). Stopping power of electron gas and equipattion rule, *Mat. Fys. Medd. K. Dan. Vidensk. Selsk. 33*, 10

Luke, P. N. et al., (1989). Low capacitance large volume shaped-field germanium detector, *IEEE Trans. Nucl. Sci. 36, Issue 1*, 926.

Mei, D.-M. & Hime, A., (2006). Muon-induced background study for underground laboratories, *Physical Review D 73*, 053004.

Marrone, S., (2002). Pulse shape analysis of liquid scintillators for neutron studies, *Nucl. Inst. and Meth. A 490*, 299-307

M. Matzke, (1994). *Unfolding of Pulse Height Spectra: The HEPRO Program System*, Report PTB-N-19, Physikalisch-Technische Bundesanstalt, Braunschweig, ISBN 3-89429-543-0

Mertig, R. et al., (1991). Feyn Calc - Computer-algebraic calculation of Feynman amplitudes 9.0, Comput . *Phys. Commun ., 64*, 345-359

Messous, Y. et al., (1995). Calibration of a Ge crystal with nuclear recoils for the development of a dark matter detector, *Astropart. Phys. 3*, 361

Oka, Y., (2010). *Nuclear Reactor Design*, (1st ed.)(52) Tokyo: Springer

Papoulias, D. K., Kosmas, T. S. (2015) Standard and non-standard neutrino-nucleus reactions cross sections and event rates to neutrino detection experiments, *Adv.High Energy Phys.* 763648

Pell, E. M., (1960). Ion Drift in an np Junction, *Journal of Applied Physics 31, Issue: 2*, 291 72

Radford, J., (2014). *m3dcr and siggen software*, Retrieved April 20, 2018, from, https://radware.phy.ornl.gov/MJ/; http://radware.phy.ornl.gov/gretina/siggen

Sabbah, B. et al., (1968). An accurate pulse-shape discriminator for a wide range of energies, *Nucl. Instr. and Meth. A 58* 102-110

Sain Gobain ∼ Liquid Scintillators, Retrieved April 20, 2018, from https://www.crystals.saint-gobain.com/sites/imdf.crystals.com/files/documents/sgc-bc501-501a-519-data-sheet_69711.pdf.

Sain Gobain ∼ Thermal Neutron Detector, Retrieved April 20, 2018, from https://www.crystals.saint-gobain.com/sites/imdf.crystals.com/files/documents/sgc-bc702-data-sheet_70148.pdf;

Sakai, E., (1971). Slow Pulses from Germanium Detectors, *IEEE Trans. Nucl. Sci. 18, (1)*, 208 110

Shtabovenko, V. et al., (2016). New Developments in FeynCalc 9.0, *Phys. Commun ., 207C*, 432-444, arXiv:1601.01167

Shutt, T. et al., (1992). Measurement of ionization and phonon production by nuclear recoils in a 60 g crystal of germanium at 25 mK, *Phys. Rev. Lett. 69*, 3425

Soma, A. K. et al, (2016). Characterization and Performance of Germanium Detectors with sub-keV Sensitivities for Neutrino and Dark Matter Experiments, https://arxiv.org/abs/1411.4802

Sonay, A., (2017). *BC501a-unfolding-Source code of unfolding algorithms*, Retrieved April 20, 2018, from https://github.com/ASonay/BC501a-unfolding

Sonay, A., (2017). *G4HND-Source code of HND Geant4 simulation*, Retrieved April 20, 2018, from https://github.com/ASonay/G4HND

Sonay, A., (2017). *G4 Simple Ge Detector-Source code of HND Geant4 simulation*, Retrieved April 20, 2018, from https://github.com/ASonay/G4_Simple_Ge_Detector

Strauss, M. & Larsen, R., (1967). Pulse height defect due to electron interaction in the dead layers of Ge(li) γ-Ray detectors, *Nucl. Inst. and Meth. 56 (1)*, 80 110

Swiderski, L. et al., (2011). Suppression of gamma-ray sensitivity of liquid scintillators for neutron detection *Nucl. Instr. and Meth. A 652* 330-333

Tanabashi, M. et al. (Particle Data Group), (2018). The Review of Particle Physics (2018), *Phys. Rev. D 98*, 030001.

Tomasello, V. et al., (2008). Calculation of neutron background for underground experiments, *Nucl. Instrum. and Meth. A595* 431-438

Tong, W. S., (2001). *FISCOF Ver 1.0, 08-4-MAN-036-001-1.1*, Institute of Nuclear Energy Research.

Verbinski, V. V. et al., (1968). Calibration of an organic scintillator for neutron spectrometry, *Nucl. Inst. and Meth. A 68*, 8-25

Wei, W. Z., Mei, D. M., Zhang, C., (2017). Cosmogenic Activation of Germanium Used for Tonne-Scale Rare Event Search Experiments, *Astroparticle Physics, 96*, 24-31,

Wolski, D. et al., (1995). Comparison of n-γ discrimination by zero-crossing and digital charge comparison methods, *Nucl. Instrum. and Methods A 360*, 584.

Wong, H. T. et al, (2007) Search of neutrino magnetic moments with a high-purity germanium detector at the Kuo-Sheng nuclear power station, *Physical Review D 75.1*, 012001.

Wong, H. T. (2011) Low energy neutrino and dark matter physics with sub-keV germanium detectors, *International Journal of Modern Physics D 20.08*, 1463–1470.

Wong, H. T. (2015) Taiwan EXperiment On NeutrinO - History, Status and Prospects. *The Universe, 3*, (4), 22-37

Yoshida, S. et al., (2010). Light output response of KamLAND liquid scintillator for protons and 12C nuclei, *Nucl. Inst. and Meth. A 622*, 574-582

Ziegler, J. F., (1998). *Transport of Ions in Matter*, Retrieved April 20, 2018, from http://www.srim.org

Zhong, H., (2001). Review of the Shockley-Ramo theorem and its application in semiconductor gamma-ray detectors, *Nucl. Inst. and Meth. A 463*, 250.

APPENDICES

Appendix A: Two Body Scattering in the Rest Frame

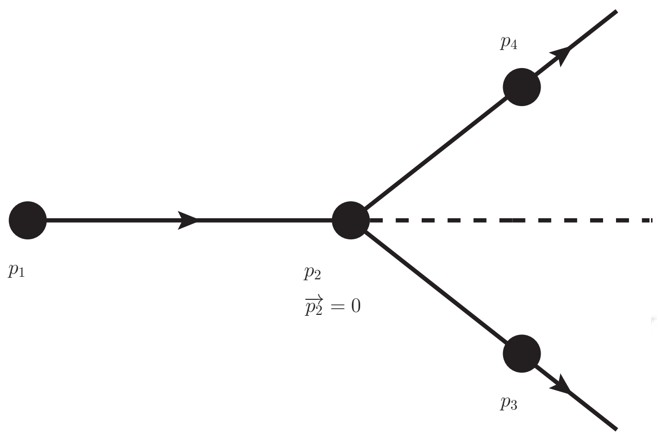

Figure A.1 The scattering in the rest frame is illustrated schematically.

It is well known that the differential cross section of the 1 + 2 $\rightarrow$ 3 + 4 process as demonstrated in Figure A.1 is determined in quantum field theory as,

$$d\sigma = |\mathscr{M}|^2 \frac{S}{4\sqrt{(p_1 \cdot p_2)^2 - (m_1 m_2)^2}} \left[\left(\frac{d^3\overrightarrow{p_3}}{(2\pi)^3 2E_3}\right)\left(\frac{d^3\overrightarrow{p_4}}{(2\pi)^3 2E_4}\right) \right] \times (2\pi)^4 \delta^4(p_1 + p_2 - p_3 - p_4) \,, \tag{A.1}$$

where p_i and $\overrightarrow{p_i}$ are denotes four momentum and 3-vectors for relative ith particle, respectively. Equation A.1 can be solved by integrating both side. There are good exercises on solving this equation in Reference Griffiths (2008). Thus the differential cross section can be given as,

$$\frac{d\sigma}{d|\overrightarrow{p_4}|} = \frac{|\mathscr{M}|^2}{32\pi} \frac{S}{m_2 |\overrightarrow{p_1}|^2} \frac{\overrightarrow{p_4}}{\sqrt{\overrightarrow{p_4}^2 + m_4^2}} \,. \tag{A.2}$$

If we consider the target material recoil which can be an electron in atomic shell or a nuclei, by T energy,

$$T = (E_4 - m_4) \,, \tag{A.3}$$

and using the relativistic energy-momentum relation we have;

$$\begin{aligned} E_4^2 - m_4^2 &= |\overrightarrow{p_4}|^2 \\ \Rightarrow (E_4 - m_4)(E_4 + m_4) &= |\overrightarrow{p_4}|^2 \\ \Rightarrow T(T + 2m_4) &= |\overrightarrow{p_4}|^2 \end{aligned} \tag{A.4}$$

By differentiate both side,

$$|\overrightarrow{p_4}|d|\overrightarrow{p_4}| = (T + m_4)dT \ . \tag{A.5}$$

The differential cross section by the recoil energy of rest particle can be obtain by putting Equation A.5 into Equation A.2,

$$\begin{aligned} \frac{d\sigma}{|\overrightarrow{p_4}|d|\overrightarrow{p_4}|} = \frac{|\mathscr{M}|^2}{32\pi}\frac{S}{m_2|\overrightarrow{p_1}|^2}\frac{1}{\sqrt{\overrightarrow{p_4}^2 + m_4^2}} &= \frac{|\mathscr{M}|^2}{32\pi}\frac{S}{m_2|\overrightarrow{p_1}|^2}\frac{1}{E_4} \\ \frac{d\sigma}{dT} = \underbrace{(T + m_4)}_{E_4} &\frac{|\mathscr{M}|^2}{32\pi}\frac{S}{m_2|\overrightarrow{p_1}|^2}\frac{1}{E_4} \\ &\boxed{\frac{d\sigma}{dT} = \frac{|\mathscr{M}|^2}{32\pi}\frac{S}{m_2|\overrightarrow{p_1}|^2}} \ . \end{aligned} \tag{A.6}$$

Thus, the Equation A.6 can be used as an observable energy of the recoil for both electron or nuclear target.

On the other hand, the maximum recoil energy of the illustrated interaction in Figure A.1 can be derived by using momentum conservation and squaring both side $(p_1 +$

$p_2)^2 = (p_3 + p_4)^2$,

$$
\begin{aligned}
p_1 \cdot p_2 &= p_3 \cdot p_4 \\
E_1E_2 - \overrightarrow{p_1} \cdot \cancelto{0}{\overrightarrow{p_2}} &= E_3E_4 - \overrightarrow{p_3} \cdot \overrightarrow{p_4} \\
E_1E_2 &= E_3E_4 - |\overrightarrow{p_3}||\overrightarrow{p_4}|cos(180) \\
\boxed{E_1m_2 = E_3E_4 + |\overrightarrow{p_3}||\overrightarrow{p_4}|}\ .
\end{aligned}
\tag{A.7}
$$

Putting Equation A.3 and A.4 into Equation A.7,

$$E_1m_x = (E_1 - T_{max})(T_{max} + m_x) + (E_1 - T_{max})\sqrt{T_{max}(T_{max} + 2m_x)} \tag{A.8}$$

where $|\overrightarrow{p_3}| = E_3 = E_1 - T$. By the solving this equation for T_{max},

$$\boxed{T_{max} = \frac{2E_1^2}{m_x + 2E_1}} \tag{A.9}$$

and the minimum energy of E_1,

$$\boxed{(E_1)_{min} = \frac{T + \sqrt{T^2 + 2Tm_x}}{2}} \tag{A.10}$$

With same motivation in Equation A.7 we can derived some kinematics in use of differential cross section calculations,

$$\boxed{p_1 \cdot p_2 = E_1E_2 - \overrightarrow{p_1} \cdot \cancelto{0}{\overrightarrow{p_2}} = E_1m_2}\ , \tag{A.11}$$

$$\boxed{p_2 \cdot p_4 = E_2 E_4 - \cancelto{0}{\overrightarrow{p_2}} \cdot \overrightarrow{p_4} = m_2 E_4}\,, \tag{A.12}$$

$$\begin{aligned}
(p_1 - p_3)^2 &= (p_4 - p_2)^2 \\
m_1^2 + m_3^2 - 2p_1 \cdot p_3 &= m_4^2 + m_2^2 - 2p_4 \cdot p_2 \\
2m_\nu^2 - 2p_1 \cdot p_3 &= 2m_2^2 - 2\underbrace{p_4 \cdot p_2}_{m_2 E_4} \\
p_1 \cdot p_3 &= m_\nu^2 - m_2^2 + m_2 E_4 \\
p_1 \cdot p_3 &= m_\nu^2 + m_2 \underbrace{(E_4 - m_2)}_{T} \\
&\boxed{p_1 \cdot p_3 = m_\nu^2 - m_2 T}\,.
\end{aligned} \tag{A.13}$$

Therefore, these Equations in A.11, A.12 and A.13 can be used for differential cross section calculation for different interactions in laboratory frame by considering momentum conservation relations.

Appendix B: Neutrino-Electron Elastic Scattering

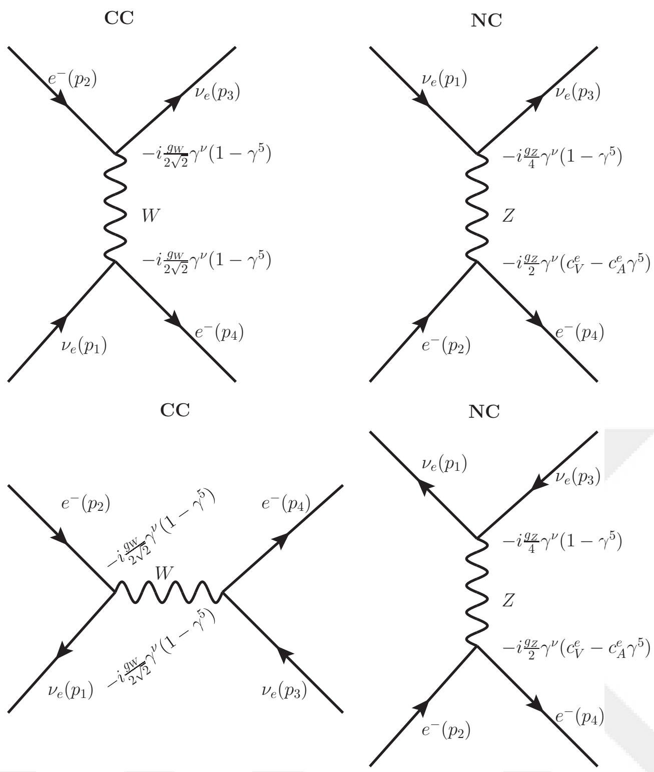

Figure B.1 Feynmann diagrams of $\nu_e - e(\bar{\nu}_e - e)$ scatterings with vertex factors.

Feynmann diagrams of $\nu_e - e(\bar{\nu}_e - e)$ scatterings are depicted in Figure B.1. The vertex factor for this interactions are well known in standard model. The total amplitude by the Feynmann rules can be written as,

$$\mathscr{M}_{\nu_e(\bar{\nu}_e)-e} = \mathscr{M}^{NC}_{\nu_e(\bar{\nu}_e)-e} - \mathscr{M}^{CC}_{\nu_e(\bar{\nu}_e)-e} \tag{B.1}$$

Considering the parameters g_W and g_Z are related with the Fermi coupling constant $G_F \equiv \sqrt{2}g_Z^2/8m_Z^2 \equiv \sqrt{2}g_W^2/8m_W^2$, amplitudes can be written as,

$$\mathscr{M}^{NC}_{\nu_e-e} = \frac{\sqrt{2}G_F}{2}[\bar{u}(p_3)\gamma^\mu(1-\gamma^5)u(p_1)][\bar{u}(p_4)\gamma_\mu(c^e_V - c^e_A\gamma^5)u(p_2)]$$
$$\mathscr{M}^{CC}_{\nu_e-e} = \frac{\sqrt{2}G_F}{2}[\bar{u}(p_4)\gamma^\mu(1-\gamma^5)u(p_1)][\bar{u}(p_3)\gamma_\mu(1-\gamma^5)u(p_2)] \tag{B.2}$$

$$\mathscr{M}^{NC}_{\bar{\nu}_e-e} = \frac{\sqrt{2}G_F}{2}[\bar{v}(p_1)\gamma^\mu(1-\gamma^5)v(p_3)][\bar{u}(p_4)\gamma_\mu(c^e_V - c^e_A\gamma^5)u(p_2)]$$
$$\mathscr{M}^{CC}_{\bar{\nu}_e-e} = \frac{\sqrt{2}G_F}{2}[\bar{u}(p_4)\gamma^\mu(1-\gamma^5)v(p_3)][\bar{v}(p_1)\gamma_\mu(1-\gamma^5)u(p_2)] \tag{B.3}$$

The square of amplitude can be written as,

$$\begin{aligned} |\mathscr{M}_{\nu_e(\bar{\nu}_e)-e}|^2 = &|\mathscr{M}^{NC}_{\nu_e(\bar{\nu}_e)-e}|^2 + |\mathscr{M}^{CC}_{\nu_e(\bar{\nu}_e)-e}|^2 \\ &-\mathscr{M}^{NC}_{\nu_e(\bar{\nu}_e)-e}\mathscr{M}^{CC}_{\nu_e(\bar{\nu}_e)-e} - \mathscr{M}^{CC}_{\nu_e(\bar{\nu}_e)-e}\mathscr{M}^{NC}_{\nu_e(\bar{\nu}_e)-e} \end{aligned} \tag{B.4}$$

By using Casimir trick Griffiths (2008), expected values of the amplitude can be written in following form,

$$\langle|\mathscr{M}_{\nu_e-e}|^2\rangle = \frac{G_F^2}{4}\{$$

$$Tr[\gamma^\mu(1-\gamma^5)\not{p}_1\gamma^\nu(1-\gamma^5)\not{p}_3]Tr[\gamma_\mu(c_V^e - c_A^e\gamma^5)(\not{p}_2+m_e)\gamma_\nu(c_V^e - c_A^e\gamma^5)(\not{p}_4+m_e)]$$
$$+Tr[\gamma^\mu(1-\gamma^5)\not{p}_1\gamma^\nu(1-\gamma^5)(\not{p}_4 m_e)]Tr[\gamma_\mu(1-\gamma^5)(\not{p}_2+m_e)\gamma_\nu(1-\gamma^5)\not{p}_3]$$
$$-Tr[\gamma^\mu(1-\gamma^5)\not{p}_1\gamma^\nu(1-\gamma^5)(\not{p}_4+m_e)\gamma_\mu(c_V^e - c_A^e\gamma^5)(\not{p}_2+m_e)\gamma_\nu(1-\gamma^5)\not{p}_3]$$
$$-Tr[\gamma^\mu(1-\gamma^5)\not{p}_1\gamma^\nu(1-\gamma^5)\not{p}_3\gamma_\mu(1-\gamma^5)(\not{p}_2+m_e)\gamma_\nu(c_V^e - c_A^e\gamma^5)(\not{p}_4+m_e)]$$
$$\}$$

(B.5)

$$\langle|\mathscr{M}_{\bar{\nu}_e-e}|^2\rangle = \frac{G_F^2}{4}\{$$

$$Tr[\gamma_\mu(c_V^e - c_A^e\gamma^5)(\not{p}_2+m_e)\gamma_\nu(c_V^e - c_A^e\gamma^5)(\not{p}_4+m_e)]Tr[\gamma^\mu(1-\gamma^5)\not{p}_3\gamma^\nu(1-\gamma^5)\not{p}_1]$$
$$+Tr[\gamma^\mu(1-\gamma^5)(\not{p}_2+m_e)\gamma^\nu(1-\gamma^5)\not{p}_1]Tr[\gamma_\mu(1-\gamma^5)\not{p}_3\gamma_\nu(1-\gamma^5)(\not{p}_4+m_e)]$$
$$-Tr[\gamma^\mu(c_V^e - c_A^e\gamma^5)(\not{p}_2+m_e)\gamma^\nu(1-\gamma^5)\not{p}_1\gamma_\mu(1-\gamma^5)\not{p}_3\gamma_\nu(1-\gamma^5)(\not{p}_4+m_e)]$$
$$-Tr[\gamma^\mu(1-\gamma^5)(\not{p}_2+m_e)\gamma^\nu(c_V^e - c_A^e\gamma^5)(\not{p}_4+m_e)\gamma_\mu(1-\gamma^5)\not{p}_3\gamma_\nu(1-\gamma^5)\not{p}_1]$$
$$\}$$

(B.6)

The traces in Equation B.5 and Equation B.6 can be calculate by computation via FeynCalc Mertig et al. (1991); Shtabovenko et al. (2016) and by using some kinematics in Appendices A. The FeynCalc codes with differential cross section of $\nu_e - e(\bar{\nu}_e - e)$ scatterings for electron recoil according to Equation A.6 are given follows, In[1]:=

```
<< FeynCalc`
Off[RuleDelayed::rhs, Rule::rhs];
"FeynCalc ""9.3.0 (development version). For help, use the "
 documentation center", check out the "wiki" or write to the "mailing list.
"See also the supplied "examples.
 " If you use FeynCalc in your research, please cite"
" • V. Shtabovenko, R. Mertig and F. Orellana, Comput.
  Phys. Commun., 207C, 432-444, 2016, arXiv:1601.01167"
" • R. Mertig, M. Böhm, and A. Denner, Comput. Phys. Commun., 64, 345-359, 1991."
```

In[7]:=

DIRAC FUNCTIONS

```
dm[mu_] := DiracMatrix[mu]
ds[p_] := DiracSlash[p]
sp[p_, q_] := ScalarProduct[p, q]
prop[p_, m_] := ds[p] + m c
fac1 = -dm[5] + 1;
fac2 = -dm[5] ca + cv;
```

In[14]:=

TRACE CALCULATION

```
LineA1 := dm[mu] . fac1 . ds[p1] . dm[nu] . fac1. ds[p3]
LineA2 := dm[mu] . fac2 . prop[p2, m] . dm[nu] . fac2 . prop[p4, m]

LineB1 := dm[mu] . fac1 . ds[p1] . dm[nu] . fac1. prop[p4, m]
LineB2 := dm[mu] . fac1 . prop[p2, m] . dm[nu] . fac1 . ds[p3]

LineAB :=
 dm[mu] . fac1 . ds[p1] . dm[nu] . fac1. prop[p4, m]. dm[mu] . fac2 . prop[p2, m] .dm[nu] . fac1 . ds[p3]
LineBA := dm[mu] . fac1 . ds[p1] . dm[nu] . fac1 . ds[p3] .
  dm[mu] . fac1 . prop[p2, m] .dm[nu] . fac2 . prop[p4, m]

A = Simplify[Contract[Tr[LineA1] . Tr[LineA2] ]] (G_F^2 / 4)
B = Simplify[Contract[Tr[LineB1] . Tr[LineB2] ]] (G_F^2 / 4)
AB = Simplify[Contract[Tr[LineAB] ]] (G_F^2 / 4)
BA = Simplify[Contract[Tr[LineBA] ]] (G_F^2 / 4)

M2 = FullSimplify[A + B - AB - BA /. cv → c_v - 1 /. ca → c_a - 1] /. c_v → c_v + 1 /. c_a → c_a + 1
```

$$16\,G_F^2\left(c^2\,m^2\left(\mathrm{ca}^2-\mathrm{cv}^2\right)\left(\overline{\mathrm{p1}}\cdot\overline{\mathrm{p3}}\right)+(\mathrm{ca}-\mathrm{cv})^2\left(\overline{\mathrm{p1}}\cdot\overline{\mathrm{p4}}\right)\left(\overline{\mathrm{p2}}\cdot\overline{\mathrm{p3}}\right)+(\mathrm{ca}+\mathrm{cv})^2\left(\overline{\mathrm{p1}}\cdot\overline{\mathrm{p2}}\right)\left(\overline{\mathrm{p3}}\cdot\overline{\mathrm{p4}}\right)\right)$$

$$64\,G_F^2\left(\overline{\mathrm{p1}}\cdot\overline{\mathrm{p2}}\right)\left(\overline{\mathrm{p3}}\cdot\overline{\mathrm{p4}}\right)$$

$$-16\,G_F^2\left(c^2\,m^2\,(\mathrm{ca}-\mathrm{cv})\left(\overline{\mathrm{p1}}\cdot\overline{\mathrm{p3}}\right)+2\,(\mathrm{ca}+\mathrm{cv})\left(\overline{\mathrm{p1}}\cdot\overline{\mathrm{p2}}\right)\left(\overline{\mathrm{p3}}\cdot\overline{\mathrm{p4}}\right)\right)$$

$$-16\,G_F^2\left(c^2\,m^2\,(\mathrm{ca}-\mathrm{cv})\left(\overline{\mathrm{p1}}\cdot\overline{\mathrm{p3}}\right)+2\,(\mathrm{ca}+\mathrm{cv})\left(\overline{\mathrm{p1}}\cdot\overline{\mathrm{p2}}\right)\left(\overline{\mathrm{p3}}\cdot\overline{\mathrm{p4}}\right)\right)$$

$$16\,G_F^2\left(c^2\,m^2\left((c_a+1)^2-(c_v+1)^2\right)\left(\overline{\mathrm{p1}}\cdot\overline{\mathrm{p3}}\right)+(c_a-c_v)^2\left(\overline{\mathrm{p1}}\cdot\overline{\mathrm{p4}}\right)\left(\overline{\mathrm{p2}}\cdot\overline{\mathrm{p3}}\right)+(c_a+c_v+2)^2\left(\overline{\mathrm{p1}}\cdot\overline{\mathrm{p2}}\right)\left(\overline{\mathrm{p3}}\cdot\overline{\mathrm{p4}}\right)\right)$$

In[26]:=

AMPLITUDE on LAB FRAME

```
labframeshell = {sp[p3, p4] → sp[p1, p2], sp[p1, p4] → sp[p2, p3]}
labframe = {sp[p1, p2] → Eν m, sp[p2, p3] → (Eν - T) m, sp[p1, p3] → m T}

M2shell = Simplify[M2 /. labframeshell];
M2lab = M2shell /. labframe
```

$$\left\{\overline{\mathrm{p3}}\cdot\overline{\mathrm{p4}}\to\overline{\mathrm{p1}}\cdot\overline{\mathrm{p2}},\ \overline{\mathrm{p1}}\cdot\overline{\mathrm{p4}}\to\overline{\mathrm{p2}}\cdot\overline{\mathrm{p3}}\right\}$$

$$\left\{\overline{\mathrm{p1}}\cdot\overline{\mathrm{p2}}\to \mathrm{E}\nu\, m,\ \overline{\mathrm{p2}}\cdot\overline{\mathrm{p3}}\to m\,(\mathrm{E}\nu-T),\ \overline{\mathrm{p1}}\cdot\overline{\mathrm{p3}}\to m\,T\right\}$$

$$16\,G_F^2\left(c^2\,m^3\,T\left((c_a+1)^2-(c_v+1)^2\right)+\mathrm{E}\nu^2\,m^2\,(c_a+c_v+2)^2+m^2\,(\mathrm{E}\nu-T)^2\,(c_a-c_v)^2\right)$$

In[31]:=

DIFFERENTIAL CROSS SECTION

```
DC = FullSimplify[(M2lab / (16 G_F^2 m^2))];

Print["\!\(\*FractionBox[\(dσ\), \(dT\)]\) = \!\(\*FractionBox[\(G_F^2m\), \(2πEν^2\)]\) [", DC, "]"]
```

Out[31]= CROSS DIFFERENTIAL SECTION

$$\frac{d\sigma}{dT}=\frac{G_F^2\,m}{2\,\pi \mathrm{E}\nu^2}\left[(\mathrm{E}\nu-T)^2\,(c_a-c_v)^2+\mathrm{E}\nu^2\,(2+c_a+c_v)^2+c^2\,m\,T\left((1+c_a)^2-(1+c_v)^2\right)\right]$$

In[34]:=

SIMPLIFIED DIFFERENTIAL CROSS SECTION

```
SDC = FullSimplify[FullSimplify[DC /. c_v → cv /. c_a → ca] /. cv + ca → a - 2 /. ca - cv → -b];
Print["\!\(\*FractionBox[\(dσ\), \(dT\)]\) = \!\(\*FractionBox[\(G_F^2m\), \(2πEν^2\)]\) [", SDC, "]"]
```

Out[34]= CROSS DIFFERENTIAL SECTION SIMPLIFIED

$$\frac{d\sigma}{d\mathrm{T}}=\frac{G_F^2\,m}{2\,\pi \mathrm{E}\nu^2}\left[-a\,b\,m\,T\,c^2+a^2\,\mathrm{E}\nu^2+b^2\,(\mathrm{E}\nu-T)^2\right]$$

In[1]:=

```
<< FeynCalc`
Off[RuleDelayed::rhs, Rule::rhs];
"FeynCalc ""9.3.0 (development version). For help, use the "
 documentation center", check out the "wiki" or write to the "mailing list.
"See also the supplied "examples.
 " If you use FeynCalc in your research, please cite"
" • V. Shtabovenko, R. Mertig and F. Orellana, Comput.
  Phys. Commun., 207C, 432-444, 2016, arXiv:1601.01167"
" • R. Mertig, M. Böhm, and A. Denner, Comput. Phys. Commun., 64, 345-359, 1991."
```

In[7]:=

DIRAC FUNCTIONS

```
dm[mu_] := DiracMatrix[mu]
ds[p_] := DiracSlash[p]
sp[p_, q_] := ScalarProduct[p, q]
prop[p_, m_] := ds[p] + m c
fac1 = -dm[5] + 1;
fac2 = -dm[5] ca + cv;
```

In[14]:=

TRACE CALCULATION

```
LineA1 := dm[mu].fac2.prop[p2, m].dm[nu].fac2.prop[p4, m]
LineA2 := dm[mu].fac1.ds[p3].dm[nu].fac1.ds[p1]

LineB1 := dm[mu].fac1.prop[p2, m].dm[nu].fac1.ds[p1]
LineB2 := dm[mu].fac1.ds[p3].dm[nu].fac1.prop[p4, m]

LineAB := dm[mu].fac2.prop[p2, m].dm[nu].fac1.ds[p1].dm[mu].fac1.ds[p3].dm[nu].fac1.prop[p4, m]
LineBA := dm[mu].fac1.prop[p2, m].dm[nu].fac2.prop[p4, m].dm[mu].fac1.ds[p3].dm[nu].fac1.ds[p1]

A = Simplify[Contract[Tr[LineA1] . Tr[LineA2]]] (GF^2/4)
B = Simplify[Contract[Tr[LineB1] . Tr[LineB2]]] (GF^2/4)
AB = Simplify[Contract[Tr[LineAB]]] (GF^2/4)
BA = Simplify[Contract[Tr[LineBA]]] (GF^2/4)

M2 = FullSimplify[A + B - AB - BA /. cv → cv - 1 /. ca → ca - 1] /. cv → cv + 1 /. ca → ca + 1
```

$$16\,G_F^2\left(c^2 m^2\left((c_a+1)^2-(c_v+1)^2\right)\left(\overline{\text{p1}}\cdot\overline{\text{p3}}\right)+(c_a-c_v)^2\left(\overline{\text{p1}}\cdot\overline{\text{p2}}\right)\left(\overline{\text{p3}}\cdot\overline{\text{p4}}\right)+(c_a+c_v+2)^2\left(\overline{\text{p1}}\cdot\overline{\text{p4}}\right)\left(\overline{\text{p2}}\cdot\overline{\text{p3}}\right)\right)$$

$$-16\,G_F^2\left(c^2 m^2(\text{ca}-\text{cv})\left(\overline{\text{p1}}\cdot\overline{\text{p3}}\right)+2(\text{ca}+\text{cv})\left(\overline{\text{p1}}\cdot\overline{\text{p4}}\right)\left(\overline{\text{p2}}\cdot\overline{\text{p3}}\right)\right)$$

$$-16\,G_F^2\left(c^2 m^2(\text{ca}-\text{cv})\left(\overline{\text{p1}}\cdot\overline{\text{p3}}\right)+2(\text{ca}+\text{cv})\left(\overline{\text{p1}}\cdot\overline{\text{p4}}\right)\left(\overline{\text{p2}}\cdot\overline{\text{p3}}\right)\right)$$

$$64\,G_F^2\left(\overline{\text{p1}}\cdot\overline{\text{p4}}\right)\left(\overline{\text{p2}}\cdot\overline{\text{p3}}\right)$$

$$16\,G_F^2\left(c^2 m^2\left(\text{ca}^2-\text{cv}^2\right)\left(\overline{\text{p1}}\cdot\overline{\text{p3}}\right)+(\text{ca}-\text{cv})^2\left(\overline{\text{p1}}\cdot\overline{\text{p2}}\right)\left(\overline{\text{p3}}\cdot\overline{\text{p4}}\right)+(\text{ca}+\text{cv})^2\left(\overline{\text{p1}}\cdot\overline{\text{p4}}\right)\left(\overline{\text{p2}}\cdot\overline{\text{p3}}\right)\right)$$

In[26]:=

AMPLITUDE on LAB FRAME

```
labframeshell = {sp[p3, p4] → sp[p1, p2], sp[p1, p4] → sp[p2, p3]}
labframe = {sp[p1, p2] → Eν m, sp[p2, p3] → (Eν - T) m, sp[p1, p3] → m T}

M2shell = Simplify[M2 /. labframeshell];
M2lab = M2shell /. labframe
```

$$16\,G_F^2\left(c^2 m^3 T\left((c_a+1)^2-(c_v+1)^2\right)+\text{E}\nu^2 m^2(c_a-c_v)^2+m^2(\text{E}\nu-T)^2(c_a+c_v+2)^2\right)$$

$$\left\{\overline{\text{p1}}\cdot\overline{\text{p2}}\to \text{E}\nu\, m,\ \overline{\text{p2}}\cdot\overline{\text{p3}}\to m\,(\text{E}\nu-T),\ \overline{\text{p1}}\cdot\overline{\text{p3}}\to m\,T\right\}$$

$$\left\{\overline{\text{p3}}\cdot\overline{\text{p4}}\to\overline{\text{p1}}\cdot\overline{\text{p2}},\ \overline{\text{p1}}\cdot\overline{\text{p4}}\to\overline{\text{p2}}\cdot\overline{\text{p3}}\right\}$$

In[31]:=

DIFFERENTIAL CROSS SECTION

```
DC = FullSimplify[(M2lab/(16 GF^2 m^2))];

Print["\!\(\*FractionBox[\(dσ\), \(dT\)]\) = \!\(\*FractionBox[\(GF^2m\), \(2πEν^2\)]\) [", DC, "]"]
```

$$\frac{\text{d}\sigma}{\text{dT}} = \frac{\text{G}_\text{F}^2\,\text{m}}{2\,\pi\text{E}\nu^2}\ \Big[\ \text{E}\nu^2\,(\text{c}_\text{a}-\text{c}_\text{v})^2+(\text{E}\nu-\text{T})^2\,(2+\text{c}_\text{a}+\text{c}_\text{v})^2+\text{c}^2\,\text{m}\,\text{T}\left((1+\text{c}_\text{a})^2-(1+\text{c}_\text{v})^2\right)\Big]$$

In[34]:=

SIMPLIFIED DIFFERENTIAL CROSS SECTION

```
SDC = FullSimplify[FullSimplify[DC /. cv → cv /. ca → ca] /. cv + ca → a - 2 /. ca - cv → -b];
Print["\!\(\*FractionBox[\(dσ\), \(dT\)]\) = \!\(\*FractionBox[\(GF^2m\), \(2πEν^2\)]\) [", SDC, "]"]
```

$$\frac{\text{d}\sigma}{\text{dT}} = \frac{G_F^2\,m}{2\,\pi\text{E}\nu^2}\left[-a\,b\,m\,T\,c^2+b^2\,\text{E}\nu^2+a^2\,(\text{E}\nu-T)^2\right]$$

Appendix C: Cohherent Elastic Neutrino Nucleus Scattering

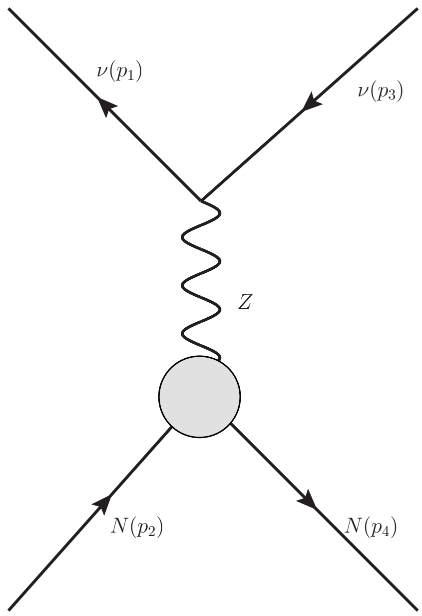

Figure C.1 Feynmann diagram of CENNS for anti-neutrino.

The CENNS has only neutral current component as illustrated in Figure C.1. Therefore, the neutral current (NC) can be written similarly as Equation B.3 as,

$$\mathscr{M}^{NC}_{N-\bar{\nu}} = \sqrt{2}G_F[\bar{\nu}(p_1)\gamma^{\mu}(1-\gamma^5)\nu(p_3)][\bar{N}(p_4)(J_{\mu})_{NC}N(p_2)] \ . \tag{C.1}$$

In the SM, the neutral current J^{μ}_{NC} can be written as

$$J^{\mu}_{NC} = \sum_f \bar{f}\gamma^{\mu}(g^f_V - g^f_A\gamma^5)f \ , \tag{C.2}$$

where f stands for all elementary fermions in the SM. Therefore we have

$$\begin{aligned}\bar{N}J^{\mu}_{NC}N = g^u_L\bar{N}(\bar{u}_L\gamma^{\mu}u_L)N + g^u_R\bar{N}(\bar{u}_R\gamma^{\mu}u_R)N \\ +g^d_L\bar{N}(\bar{d}_L\gamma^{\mu}d_L)N + g^d_R\bar{N}(\bar{d}_R\gamma^{\mu}d_R)N \ .\end{aligned} \tag{C.3}$$

For a nucleus with a large mass number A, one can expect parity is not violate due to it is contains many u and d quarks so that approximately respects parity. So we have

$$g_L^u \bar{N}(\bar{u}_L \gamma^\mu u_L)N = g_R^u \bar{N}(\bar{u}_R \gamma^\mu u_R)N,$$
$$g_L^d \bar{N}(\bar{d}_L \gamma^\mu d_L)N = g_R^d \bar{N}(\bar{d}_R \gamma^\mu d_R)N \ . \tag{C.4}$$

On the other hand, in the nucleus numbers of u and d quarks are $2Z+N$ and $2N+Z$, respectively. Thus,

$$\frac{\bar{N}(\bar{u}\gamma^\mu u)N}{\bar{N}(\bar{d}\gamma^\mu d)N} = \frac{2Z+N}{2N+Z} \ . \tag{C.5}$$

From the Equation C.5 following relation can be written,

$$\bar{N}(\bar{u}\gamma^\mu u)N = (2Z+N)f^\mu,$$
$$\bar{N}(\bar{d}\gamma^\mu d)N = (2N+Z)f^\mu \ . \tag{C.6}$$

The electromagnetic current can be written as,

$$J^\mu_{EM} = \frac{2}{3}\bar{u}\gamma^\mu u + \frac{-1}{3}\bar{d}\gamma^\mu d \ . \tag{C.7}$$

Moreover, from the Feynman rules of a complex scalar field with a gauged U(1) symmetry, it is known that the interaction vertex of the gauge boson with the scalar field should be proportional with $(p_2+p_4)^\mu$. Thus,

$$\bar{N}(p_4)J^\mu_{EM}N(p_2) = (p_2+p_4)^\mu Q_Z F(Q^2) \ , \tag{C.8}$$

where Q_Z is the charge of nucleus which is related with Z. By using Equation C.6 and

C.7 f^μ can be obtain,

$$\frac{2}{3}(2Z+N)f^\mu + \frac{-1}{3}(2N+Z)f^\mu = (p_2+p_4)^\mu ZF(Q^2)$$
$$\boxed{f^\mu = (p_2+p_4)^\mu F(Q^2)}\ . \tag{C.9}$$

By using Equations C.4, C.6, C.9 into Equation C.3,

$$\begin{aligned}\bar{N}(p_4)J^\mu_{NC}N(p_2) &= F(Q^2)(p_2+p_4)^\mu[(2Z+N)g^u_V+(2N+Z)g^d_V] \\ &= F(Q^2)(p_2+p_4)^\mu[Zg^p_V+Ng^n_V]\ ,\end{aligned} \tag{C.10}$$

where,

$$g^p_V = \frac{1}{2} - 2s^2_W,\ g^n_V = -\frac{1}{2}\ . \tag{C.11}$$

Thus Equation C.1 can be written as,

$$\begin{aligned}\mathscr{M}^{NC}_{N-\bar{\nu}} &= \frac{\sqrt{2}G_F}{2}[(1-4s^2_W)Z-N]F(Q^2) \\ &\times(p_2+p_4)^\mu[\bar{\nu}(p_1)\gamma^\mu(1-\gamma^5)\nu(p_3)]\ ,\end{aligned} \tag{C.12}$$

and square of amplitude can be derived as,

$$\begin{aligned}|\mathscr{M}^{NC}_{N-\bar{\nu}}|^2 &= \frac{G^2_F}{2}[(1-4s^2_W)Z-N]^2F^2(Q^2)(p_2+p_4)^\mu(p_2+p_4)^\nu \\ &\times Tr[\not{p}_1\gamma^\mu(1-\gamma^5)\not{p}_3\gamma^\nu(1-\gamma^5)]\ ,\end{aligned} \tag{C.13}$$

after solving the trace,

$$\begin{aligned}|\mathscr{M}^{NC}_{N-\bar{\nu}}|^2 &= \frac{G^2_F}{2}[(1-4s^2_W)Z-N]^2F^2(Q^2)(p_2+p_4)^\mu(p_2+p_4)^\nu \\ &\times 8(p^\mu_1\cdot p^\nu_3+p^\nu_1\cdot p^\mu_3-g^{\mu\nu}p_1\cdot p_3-i\varepsilon^{\rho\mu\sigma\nu}p_{1\rho}p_{3\sigma})\ ,\end{aligned} \tag{C.14}$$

and with organizing the equation,

$$|\mathscr{M}^{NC}_{N-\bar{\nu}}|^2 = 4G_F^2[(1-4s_W^2)Z-N]^2F^2(Q^2)[p_1\cdot p_2p_3\cdot p_2 + p_1\cdot p_2p_3\cdot p_4 \\ \times + p_1\cdot p_4p_3\cdot p_2 + p_1\cdot p_4p_3\cdot p_4 + (M^2+p_2\cdot p_4)p_1\cdot p_3]\ . \quad \text{(C.15)}$$

by considering the kinematic in Appendices A,

$$|\mathscr{M}^{NC}_{N-\bar{\nu}}|^2 = 32G_F^2[(1-4s_W^2)Z-N]^2F^2(Q^2)M^2E_\nu^2 \\ \times(1-\frac{T}{E_\nu}-\frac{MT}{2E_\nu^2})\ . \quad \text{(C.16)}$$

As a consequence, by using Equation A.6 differential cross section of CENNS interaction can be written,

$$\frac{d\sigma}{dT} = \frac{1}{4\pi}G_F^2[(1-4s_W^2)Z-N]^2F^2(Q^2)M(1-\frac{T}{E_\nu}-\frac{MT}{2E_\nu^2})\ . \quad \text{(C.17)}$$